UNIVERSITÉ DE SHERBROOKE
Faculté de génie
Département de génie mécanique

Un modèle numérique de l'excitation couche limite turbulente pour prédire le bruit à l'intérieur d'une automobile

A Numerical Model for Turbulent Boundary Layer Excitation to Predict Interior Noise in Automobile

Thèse de doctorat
Specialité: génie mécanique

Venkata Phani Kiran VADAVALLI

Sherbrooke (Québec) Canada

Automne 2018

JURY MEMBERS

Noureddine ATALLA
Supervisor

Stéphane MOREAU
Co-supervisor

Raymond PANNETON
Examiner

Franck NICOUD
Examiner

Sébastien PONCET (Rapporteur)
Examiner

RÉSUMÉ

L'objectif principal de la thèse est de développer une approche numérique basée sur la dynamique computationnelle des fluides (CFD) pour modéliser une excitation produite par une couche limite turbulente (TBL) et, par la suite, prédire le bruit à l'intérieur de l'automobile. A cet égard, deux corps non profilés (bluff) ont été considérés : a) Un obstacle représentatif du pilier A et b) un rétroviseur générique. Ces deux corps non profilès sont placés sur un système plaque-cavité qui représente la cabine intérieure et la vitre latérale d'une automobile. Les fluctuations de la pression pariétale (WPF) sont finement résolues en utilisant une analyse CFD. Par la suite, elles sont quantifiées en termes de spectre de puissance, de spectre croisé, de cohérence et de spectre de fréquence d'onde en utilisant le code k-ω développé dans cette thèse. Grâce à la longue durée calculée par CFD, et de la finesse du maillage, les zones acoustiques et aérodynamiques sont correctement capturées pour une analyse vibro-acoustique poussée. Trois stratégies numériques sont proposées pour calculer la puissance injectée à la plaque : 1) Identification des paramètres empiriques du modèle Corcos à partir de la WPF, 2) Calcul de la puissance injectée dans le domaine du nombre d'ondes, et 3) Échantillonnage aléatoire de l'excitation TBL. Ces différentes approches ont été comparées et discutées pour proposer une approche optimale du point de vue computationnel. En d'autres termes, la véritable réalisation a consisté à trouver une méthode efficace en terme du temps de calcul pour coupler le modèle CFD de la WPF aux modes propres de la plaque afin d'obtenir la puissance injectée. Le couplage entre la structure spatiale de l'excitation et les modes propres de la structure est donnée par la "joint-acceptance". Les indicateurs vibro-acoustiques du système plaque-cavité, comme la puissance injectée, la vitesse quadratique et la pression quadratique, sont calculés à l'aide de l'approche d'analyse énergétique modale et statistique (SEA). La procédure numérique CFD/SEA appliquée à un système plaque-cavité est validée par des expériences menées dans la soufflerie de Purdue University. Parmi les trois approches numériques, le modèle Corcos dérivé de CFD semble très prometteur en termes d'efficacité en temp de calcul, car il est basé sur une méthode analytique. La meilleure approche en termes de calcul et précision est la seconde, qui résout complètement le WPF de la TBL en utilisant une CFD transitoire et calcule la puissance injectée dans le domaine de nombre d'ondes. L'originalité de cette thèse est l'estimation des paramètres du modèle de Corcos à partir d'un calcul CFD statistiquement convergé de la pression pariétale. Une autre contribution originale est de réduire le temps de calcul au niveau de l'intégration dans l'espace du nombre d'onde de la joint acceptance en proposant un nouveau critère pour les limites supérieure d'intégration.

Mots-clés : bruit du vent automobile, aérodynamique, aéro-acoustique, couche limite turbulente, dynamique computationnelle des fluides, vibro-acoustique,

ABSTRACT

The main objective is to develop a Computational Fluid Dynamics(CFD) based numerical approach to model the turbulent boundary layer (TBL) excitation and later predict the interior noise. In this regard, two automobile bluff bodies were considered a) flat fence representative of A-pillar and b) generic side mirror. These two bluff bodies are placed over a plate-cavity system as a representation of side window-interior cabin of an automobile. Turbulent Wall-Pressure Fluctuations (WPF) are finely resolved using unsteady CFD analysis and later quantified in terms of power spectrum, cross-spectrum, coherence and wavenumber-frequency spectrum using the k-ω code developed as a part of this work. Due to a lengthy CFD run and finely resolved CFD mesh, both acoustic and aerodynamic zones were properly captured for further vibro-acoustic analysis. Three numerical strategies are proposed to calculate the TBL power input to the plate. 1) Identification of empirical Corcos model parameters from unsteady CFD WPF through curve fitting; 2) TBL power input calculation in wavenumber domain; 3) Random sampling of TBL excitation. Different approaches have been compared and discussed to propose a computationally optimal approach. In simple words, the real task at hand is to find a computationally efficient approach to couple the CFD WPF with plate modeshapes to obtain the TBL power input. The coupling strength between excitation and structural modeshapes is given by "joint-acceptance". The vibro-acoustics indicators of plate-cavity system like input power, quadratic velocity, quadratic pressure are calculated using Modal and Statistical Energy Analysis (SEA) approach. The numerical CFD/SEA procedure applied for a plate-cavity system is validated with experiments conducted at Purdue University wind tunnel. Among the three numerical approaches, CFD derived Corcos model looks very promising in terms of computational efficiency as its based on analytical method. The best approach in terms of accuracy and computation is the second one, which fully resolves the TBL WPF using unsteady CFD and calculate the TBL power input to plate in wavenumber domain. The originality of thesis is due to the estimation of Corcos parameters from a statistically converged CFD wall-pressure. Another original contribution is to minimize the computational effort in the wavenumber integration of joint acceptance by proposing a new criterion for upper limits.

Keywords: Automobile wind noise, Aerodynamics, Aero-acoustics, Computational Fluid Dynamics, Turbulent Boundary Layer, Vibro-acoustics

To
God Ganesha and God Surya,
my Dear loving wife Sravanti
and
Dear children Krishna, Sadasiva.
JAISRIMATA.

ACKNOWLEDGEMENTS

I have no “words” to express my gratitude to everyone who have touched my life in this enduring course both past and present, as mere words will fall short of my true feelings. It has been a roller coaster ride of emotions within myself and towards everyone who have been with me all through this tiring and fun journey. The present thesis does not exist without the able guidance of my supervisors Prof. Noureddine Atalla and Prof. Stéphane Moreau. A million thanks to both of you for all. Many thanks to all my jury members and reviewers who have provided valuable feedback and constructive comments.

Also I wish to thank the kind staff at Faculté de génie, many of my good friends at Groupe d’Acoustique de l’Université de Sherbrooke (GAUS) Lab and in Université de Sherbrooke. I have to thank my family and friends in Sherbrooke who have always been my strength in all times. I have to sincerely apologize to everyone for not able to mention all names as its exhaustive. I am greatly indebted to the my first supervisor Prof. Noureddine Atalla for giving me an opportunity to work in the well renowned GAUS lab and appreciate the kind support and guidance provided by second supervisor Prof. Stéphane Moreau and Madam Marlene.

I would like to thank EXA corporation and its CFD aeroacoustics team, D. Freed, S. Siva, F. Pérot and B. Powell for providing the license to PowerFLOW software and their assistance with the set-up of the simulations. Also I would also like to acknowledge J. Park and L. Mongeau at Purdue University for sharing experimental data on both cases.

Many thanks to Dr. Huizhong Lu at Centre de calcul scientifique (CCS) Sherbrooke for his prompt assistance in running the CFD simulations on Mammouth supercomputer. Computations were made on the supercomputer Mammouth parallèle 2(Interactive nodes: mp09, mp26 and mp28) from Université de Sherbrooke, managed by Calcul Québec and Compute Canada. The operation of this supercomputer is funded by the Canada Foundation for Innovation (CFI), NanoQuébec, RMGA and the Fonds de recherche du Québec - Nature et technologies (FRQNT).

I wish to express my gratitude to the kindest and friendly people in Québec and Canada who made my journey a memorable one. Last but not least I would like say “Thanks to Almighty God”.

TABLE OF CONTENTS

1 INTRODUCTION **1**
- 1.1 Automotive interior noise: Technological problem . . . 1
- 1.2 Aerodynamic noise: Scientific problem . . . 2
- 1.3 Motivation and challenges . . . 3
  - 1.3.1 Estimation of low wavenumber TBL WPF . . . 3
  - 1.3.2 Deficiency of empirical TBL models . . . 4
- 1.4 Research problem . . . 5
  - 1.4.1 Computational aerodynamics and aero-vibro-acoustics . . . 5
  - 1.4.2 Test cases considered . . . 5
  - 1.4.3 Assumptions . . . 7
- 1.5 Objectives of research . . . 7
- 1.6 Outline of thesis . . . 7

2 LITERATURE REVIEW **9**
- 2.1 Overview . . . 9
- 2.2 Mechanism of aerodynamic/TBL excitation . . . 10
- 2.3 Features of separated and reattached flows . . . 11
  - 2.3.1 Backward facing step . . . 12
  - 2.3.2 Boundary layer with pressure gradients . . . 14
  - 2.3.3 Boundary layer wall scaling parameters . . . 16
  - 2.3.4 Flat plate boundary layer parameters: Exact and approximate methods 19
  - 2.3.5 Aerodynamic dimensionless numbers . . . 22
  - 2.3.6 Summary of boundary layer separation control techniques . . . 23
- 2.4 Modelling turbulent boundary layer excitation . . . 23
- 2.5 Empirical/Semi-empirical models for TBL wall-pressure fluctuations . . . 25
  - 2.5.1 One-point wall-pressure spectrum models . . . 26
  - 2.5.2 Two-point wall-pressure spectrum models . . . 29
- 2.6 Numerical models for TBL wall-pressure fluctuations . . . 33
  - 2.6.1 Unsteady CFD Tools . . . 34
  - 2.6.2 Statistical and Stochastic models based on steady RANS . . . 36
- 2.7 Measurement of TBL wall pressure fluctuations . . . 41
- 2.8 Vibroacoustic analysis due to TBL Excitation . . . 43
  - 2.8.1 Approximate analytical methods . . . 43
  - 2.8.2 Modal based element methods: FEM and BEM . . . 45
  - 2.8.3 Band averaged energy based methods: SEA . . . 47
  - 2.8.4 Random sampling methods . . . 48
- 2.9 Conclusions . . . 48

3 IDENTIFICATION OF EMPIRICAL TBL MODEL PARAMETERS FROM CFD WALL PRESSURE **50**
3.1 Introduction . . . 50
3.2 Aerodynamic simulations . . . 51
3.2.1 Test cases and experimental data . . . 51
3.2.2 Monitoring the CFD simulation run . . . 54
3.3 Mean flow analysis . . . 56
3.4 Unsteady flow analysis . . . 66
3.4.1 PSD: simulations vs experiments for side mirror . . . 66
3.4.2 Fence side mirror PSD roll off . . . 72
3.4.3 Effect of side mirror yaw angle on PSD . . . 74
3.4.4 Spatio-temporal analysis of turbulent flow . . . 74
3.4.5 Spatial variation of wavenumber-frequency spectrum for side mirror 83
3.5 TBL model parameter identification from CFD WPF . . . 84
3.5.1 Identification of convection ratio and coherence decay . . . 84
3.5.2 Identification of homogeneous zone based on flow reattachent and dB map . . . 87
3.5.3 Empirical TBL parameter identification for the flat fence . . . 90
3.5.4 Empirical TBL parameter identification for side mirror . . . 90
3.6 Expressions for vibroacoustics indicators for plate excited by TBL . . . 93
3.7 Vibroacoustics of plate using CFD derived Corcos model . . . 98
3.8 Conclusions . . . 101

4 POWER INPUT DUE TO CFD DERIVED TBL EXCITATION IN WAVENUMBER DOMAIN **103**
4.1 Introduction . . . 103
4.2 Wavenumber domain concept . . . 104
4.3 Identification of the plate boundary conditions based on point mobility test 104
4.4 Numerical evaluation of joint acceptance in spatial domain with cross spectral density known at discrete points . . . 106
4.5 Numerical evaluation of joint acceptance in wavenumber domain with wavenumber-frequency spectrum known at discrete points . . . 110
4.6 Wavenumber interaction between TBL and structural modes . . . 114
4.7 Upper limits of joint acceptance integration at low speed flow . . . 118
4.8 Validation of joint acceptance integration using Corcos model . . . 120
4.9 Validation of joint acceptance integration using CFD wavenumber WPF . . 121
4.10 Conclusions . . . 124

5 RANDOM SAMPLING OF CFD DERIVED TBL WPF **125**
5.1 Introduction 125
5.2 Numerical algorithm for Random sampling 125
5.3 Vibroacoustics of plate-cavity system using Random sampling 126
5.4 Conclusions 129

6 CONCLUSION **130**
6.1 Summary of work 130
6.2 Future work and Perspectives 132

7 Résumé du travail **133**
7.1 Résumé du travail 133
7.2 Travaux futurs et Perspectives 135

LIST OF REFERENCES **137**

LIST OF FIGURES

1.1 Automotive noise sources for typical passenger car [Crocker, 2007, Chapter 83] 1
1.2 Wind noise sources for typical passenger car 2
1.3 Wavenumber-frequency Spectrum of TBL WPF at constant frequency[Bull, 1996] 3
1.4 Schematic of Flat fence on plate-cavity system in wind tunnel 6
1.5 Side mirror(left) and cavity microphone (right) in wind tunnel 6

2.1 Schematic of plate-cavity system excited by TBL 10
2.2 Flow topology for backward facing step [Driver *et al.*, 1987] 13
2.3 Structure of boundary layer separation and reattachment showing separation bubble, [Horton, 1968] 13
2.4 Favorable and adverse pressure gradients in boundary layer separation [Leishman, 2006] 16
2.5 Inner outer and overlap layer laws relating velocity profiles in turbulent wall flow. [White, 1999] 17
2.6 Schematic representation of wavenumber-frequency specrum at constant frequency depicting the variation regions [Howe, 1998] 25
2.7 Generalised schematic of roll-off of one-point frequency spectrum in different scales by [Hwang *et al.*, 2003] 27
2.8 Comparison of one-point frequency spectrum predicted by empirical models with measured by [Farabee, 1986] as presented by [Hwang *et al.*, 2003] . . . 28
2.9 Comparison of WPF with empirical models at fixed frequency [Hwang *et al.*, 2003] 33
2.10 Signal processing chart for wavevector filtering [Keith and Abraham, 1994] 44
2.11 Various domains in response calculation [Maury *et al.*, 2002] 45

3.1 Test cases considered 52
3.2 Probe locations in Experimental set-up 52
3.3 CFD simulation setup for Flat Fence 53
3.4 CFD simulation setup for side mirror 53
3.5 Fine grid on the plate for fence and mirror cases 54
3.6 Cp and lift time history for the whole plate-side mirror system 55
3.7 Lift and Drag for fence and side mirror 57
3.8 Instantaneous C_p for fence and side mirror 57
3.9 Instantaneous iso-surface at lambda2 $= -0.1$ for fence and mirror 58
3.10 Flow field around the simulated bluff bodies fence and side mirror with reattachment distances 59
3.11 Mean flow results 60
3.12 Mean TKE flow results for fence and mirror 61
3.13 Mean Cp: Experiments and PowerFLOW 62
3.14 Mean C_p from CFD (PowerFLOW) over entire plate 62

3.15 Mean streamwise C_p and u_x at the centreline of the plate for fence 64
3.16 Mean streamwise C_p and u_x in the z-direction for fence 64
3.17 Mean streamwise C_p and u_x at the centreline of the plate for mirror 64
3.18 Mean streamwise C_p and u_x in the z-direction for mirror 65
3.19 Mean streamwise X-velocity at mid-streamwise contour for mirror 65
3.20 Mean velocity profile development across the plate 67
3.21 Mean streamwise center-line velocity profiles normalised wrt inner variables 68
3.22 Comparison of mean streamwise center-line velocity profiles with Blasius Profile 69
3.23 PSD for fence and mirror 70
3.24 Spatially averaged PSD simulation and experiments 71
3.25 PSD roll-off from CFD and comparison with empirical spectral models for fence and mirror 73
3.26 Spatially averaged PSD for mirror in $-30°$ vs $30°$ to flow direction 74
3.27 Validation of k-ω code with Corcos analytical model 77
3.28 dB maps at constant frequency using k-ω code 78
3.29 Size of coherence influence zone with respect to plate center 79
3.30 Validation of the wall-pressure streamwise coherence with experiments for the side mirror 80
3.31 Two dimensional wavenumber-frequency spectrum plots at fixed frequency 81
3.32 Validation of streamwise wavenumber frequency PSD of probes 17-29 for mirror case 82
3.33 Streamwise k-ω spectrum for fence and mirror cases 82
3.34 Spanwise k-ω spectrum for fence and mirror cases 83
3.35 Location of probe array for non-homogeneous k-ω spectrum 83
3.36 Spatial variation of streamwise and spanwise k-ω spectrum for mirror case 85
3.37 Convection ratio for flat fence and side mirror 87
3.38 Reattachment iso-surface at lamda2 = -0.01 for fence and side mirror . . . 88
3.39 Homogeneous zones based on autospectrum and mean skin friction 89
3.40 CFD WPF coherence curve fitting in streawise and spanwise for fence: Ref probe 7 and probe 6d 91
3.41 CFD WPF coherence curve fitting in streamwise and spanwise for region 3 of side mirror 94
3.42 Spatial averaged quadratic velocity from CFD derived Corcos model and experiments for fence case 99
3.43 FEM mesh convergence study using CFD CPSD data and experiments for side mirror case 99
3.44 Spatial averaged quadratic velocity from FEM, CFD derived Corcos model and experiments for mirror case 100
3.45 Quadratic pressure from CFD derived Corcos model, Rayleigh integral and experiments for side mirror case 100
3.46 Quadratic pressure from CFD derived Corcos model, SEA and experiments for side mirror case 101

4.1 Driving point mobility test on side glass of passenger car 105

4.2 Comparison of experimental point mobility with FEM . . . 105
4.3 Plate mesh(left) with measurement and reference locations and Gauss bi-linear element (right) for interpolation . . . 108
4.4 Convergence of joint acceptance function for mode m=1 and n=1 in spatial domain . . . 109
4.5 Joint acceptance for mode m=7 and n=7 obtained in spatial domain . . . 109
4.6 Wavenumber mesh (left) and Gauss bi-linear element (right) for interpolation 111
4.7 Modeshape of simply supported plate for mode $m = 3$ and $n = 1$ in wavenumber domain . . . 111
4.8 Corcos model at 5 Hz frequency in wavenumber domain . . . 112
4.9 Corcos model at 1000 Hz frequency in wavenumber domain . . . 113
4.10 Wavenumber-frequency diagrams: dispersion curves . . . 114
4.11 Wavenumber interaction between low speed flow and slow mode . . . 116
4.12 Wavenumber interaction between low speed flow and fast mode under clamped and SSP BC . . . 116
4.13 Wavenumber interaction between high speed flow and slow mode . . . 117
4.14 Wavenumber interaction high speed flow and fast mode . . . 117
4.15 Joint acceptance calculated in wave number domain for m=7 and n=8 based on convective wavenumber and modal wavenumber . . . 119
4.16 High speed flow: Joint acceptance in wavenumber domain for $m = 3$ and $n = 1$ and analytical value . . . 119
4.17 High speed flow: Joint acceptance in wavenumber domain for $m = 7$ and $n = 8$ and analytical value . . . 120
4.18 Quadratic velocity using Corcos in spatial vs wavenumber domain for fence case at low speed . . . 120
4.19 Power input using Corcos in spatial vs wavenumber domain for fence case at low speed . . . 121
4.20 Fence case: Joint acceptance in wavenumber using CFD wavenumber WPF vs Corcos model . . . 121
4.21 Fence case:Quadratic velocity using CFD wavenumber WPF and CFD derived Corcos model . . . 122
4.22 Side mirror case: Joint acceptance in wavenumber using CFD wavenumber WPF and Corcos model . . . 123
4.23 Side mirror case: Quadratic velocity using CFD wavenumber WPF and CFD derived Corcos model . . . 123

5.1 Spatial averaged quadratic velocity from Random sampling, analytical Corcos model and experiment for fence case . . . 127
5.2 Power input from Random sampling, Analytical Corcos model and FEM for side mirror case . . . 128
5.3 Spatial averaged quadratic velocity from Random sampling, analytical Corcos model, FEM, experiment for side mirror case . . . 128

LIST OF TABLES

3.1 Inner variables and outer variables used in normalised PSD at Location 1 m away from fence and mirror 63
3.2 Flat fence: Corcos parameters obtained from nonlinear curve fitting 92
3.3 Validation of coherence decay and convection ratio with experimental data for side mirror for Probe 27 wrt 28 93
3.4 Side-mirror: Corcos parameters obtained from nonlinear curve fitting . . . 93

4.1 Plate and TBL details for Joint acceptance calculation 115
4.2 Computation time for the joint acceptance integration for higher structural modes 118

LIST OF SYMBOLS

Symbol	Definition
S_{pp}	PSD, Pa^2/Hz
x, y	location of measurement probe, m
x', y'	location of reference probe, m
$r_x = (x - x')$	Probe spacing in streamwise direction, m
$r_y = (y - y')$	Probe spacing in spanwise direction, m
ω	Circular frequency, rad/sec
$\psi\left(r_x, 0, \omega\right)$	Streamwise coherence
$G_p\left(r_x, r_y, \omega\right)$	Cross spectrum, Pa^2
k_x	Streamwise Wavenumber , 1/m
k_y	Spanwise Wavenumber, 1/m
$\psi\left(k_x, k_y, \omega\right)$	Wavenumber frequency spectrum, Pa^2
A	Plate surface area, m^2
γ	Phase, radians
ϕ_{mn}	Modeshapes
U_c	Convection velocity, m/s
ω_{mn}	Natural frequency, rad/sec
η_{mn}	Structural loss factor, dimensionless
η_{12}	Coupling loss factor between plate and cavity, dimensionless
$\sigma(\omega)$	radiation efficiency of plate, dimensionless
$n_1(\omega)$	modal density of plate
$n_2(\omega)$	modal density of cavity
$\langle \eta_{mn} \rangle_{\triangle\omega}$	Band averaged structural loss factor, dimensionless
M	Mass of the plate, Kg
M_{mn}	modal mass of the plate, Kg
Y_{mn}	impedance of the plate, N.s/m
$Z_{rad,mn}$	radiation resistance of the plate, N.s/m
f_{cut}	Cutoff frequency, Hz
m, n	Mode order, dimensionless
S_{vv}	Power spectrum of plate velocity, m/s^2
$\langle V^2 \rangle$	Quadratic velocity, m/s^2
P_{in}	Power input, Watt
$\langle P_{in} \rangle_{\omega}$	Band averaged power input, Watt/Hz
P_{rad}	Power radiated, Watt
$j^2(\omega)$	Joint acceptance, dimensionless
$\langle j^2_{mn} \rangle_{\triangle\omega}$	Band averaged joint acceptance, dimensionless
$\triangle\ \omega$	Frequency band width, Hz
j_{mn}	Joint acceptance, dimensionless
α_x and α_y	Corcos decay parameters, dimensionless
h	Plate thickness, m
ρ_s	Plate density, Kg/m^3

LIST OF ACRONYMS

Acronym	Definition
TBL	Turbulent Boundary Layer
WPF	Wall Pressure Fluctuations
CFD	Computational Fluid Dynamics
LES	Large Eddy Simulation
RANS	Reynolds Averaged Navier Stokes
DNS	Direct Numerical Simulation
SEA	Statistical Energy Analysis
TKE	Turbulent Kinetic Energy
PSD	Power Spectral Density
CPSD	Cross-Power Spectral Density
LBM	Lattice Boltzmann Method
FEM	Finite Element Method
BEM	Boundary Element Method

CHAPTER 1

INTRODUCTION

1.1 Automotive interior noise: Technological problem

Now-a-days the noise legislations are becoming stringent for all industrial sectors. Automobile sector is also gearing up to develop quieter, lightweight and fuel efficient vehicles to meet the noise regulations and customer requirements. Customer demands and awareness about noise has also increased due to number of car models in market. Noise reduction has become the key strategy for the success of any automobile company. There is a huge competition between the major automobile players to launch quieter and cost effective vehicles in the market. In an effort to develop quieter cars, automobile manufacturers are investing heavily in noise and vibration development. Interior noise has become a comfort metric for choosing different models of vehicles by customer. In larger size vehicles, interior noise levels can be high enough to be unacceptable, resulting in passenger discomfort and noise fatigue. In this regard, interior noise reduction has become an important consideration in the design of automotive cabin. In a typical passenger car shown in Figure 1.1, the major noise sources contributing to the interior noise are given by powertrain noise, intake noise, exhaust noise, road-tyre noise and wind noise or aerodynamic noise.

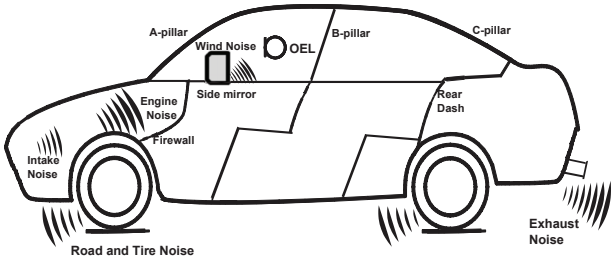

Figure 1.1 Automotive noise sources for typical passenger car [Crocker, 2007, Chapter 83]

It has been observed that aerodynamic noise increases with the sixth power of vehicle speed [Hucho, 1998]. Hence wind noise becomes dominant contributer to the interior noise at high speeds compared to other noise sources. With the development of current generation hybrid and electrical cars, wind noise becomes much more dominant over other noise sources due to light weight and quieter powertrain.The current study is focused on prediction of interior noise due to wind noise excitation without the need of expensive wind tunnel testing.

1.2 Aerodynamic noise: Scientific problem

When an automobile cruises at low mach speeds typically above 80 km/h, flow separation and vortex shedding occurs over the protusions (A-pillars, side mirrors, windshield wipers, aerials, roof bars, hood and front bumper) which act as bluff bodies. In addition to aerodynamic drag generated by the bluff bodies, these separations also generate aerodynamic noise and excitation to vehicle panels and structures. The threshold speed 80 km/h can change based on the road surface, tyre quality, engine and wind conditions etc. At these higher speeds, large amount of flow separation occurs due to the pressure drop across the bluff body and flow settles down back on the surface of vehicle hatchback. These types of flow regimes are more evident across A-pillar and side mirror and generally categorised as separated and reattaching flows. The flow separation and vortices are the source of Turbulent Boundary Layer (TBL) Wall Pressure Fluctuations (WPF) on the vehicle hatchback which excite the panels and interior car cabin. In order to predict the interior noise accurately, knowledge of the turbulent wall pressure fluctuations are very crucial in understanding the flow excitation mechanisms. For a typical passenger car, the major wind noise sources according to their ranking are A-pillar, side mirror, wheel housings and ventilation channels as shown in Figure 1.2.

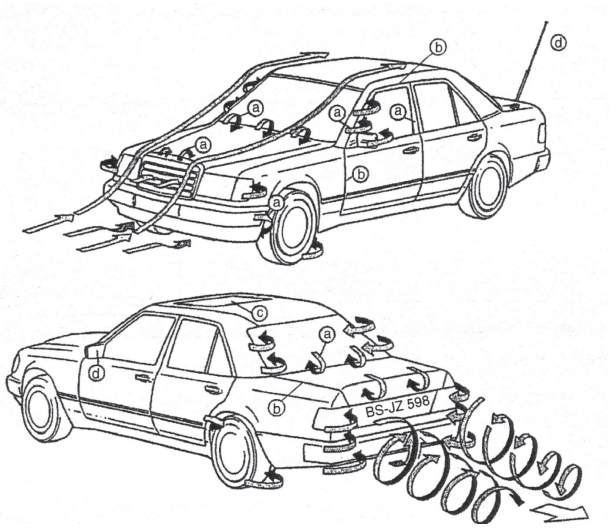

Figure 1.2 Wind noise sources for typical passenger car
Schematic given by Syed Ahmed in [Crocker, 2007, Chapter 87]

Among the bluff bodies mentioned above, A-pillar and side mirror contribute to the majority of the interior noise. Hence this study is on two bluff bodies. Accurate prediction of turbulent WPF is necessary to determine the interior noise of car cabin. This is a big challenge to acoustic engineers due to the complexity in turbulent flow topology and the coupled interaction between turbulent WPF and acoustics. This project focuses on

estimating the turbulent wall pressure fluctuations on the vehicle using Computational Fluid Dynamics (CFD) simulations and coupling the CFD wall-pressure excitation to structural modeshapes to predict the interior noise of car cabin.

1.3 Motivation and challenges

1.3.1 Estimation of low wavenumber TBL WPF

There are lot of challenges and uncertainity in modeling the turbulent boundary layer wall pressure fluctuations in terms of flow and noise sources. In order to predict the turbulent wall pressure, it is important to understand the characteristics and physical phenomenon behind the TBL WPF. A detailed historical review on the characterization of wall pressure fluctuations was presented by [Bull, 1996]. A schematic representation of wall-pressure spectrum in terms of wavenumber-frequency spectrum is shown in Figure 1.3. It depicts the presence of four regions 1) convective region 2) sub-convective region 3) acoustic region and 4) viscous region .

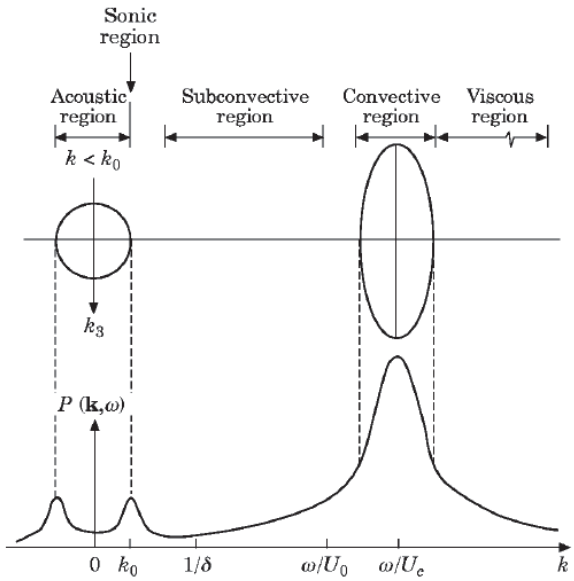

Figure 1.3 Wavenumber-frequency Spectrum of TBL WPF at constant frequency[Bull, 1996]

Out of four regions, convective region is the dominant in amplitude. But it has been observed by [Hwang *et al.*, 2003] that in case of a low mach number TBL flow, the region between acoustic zone and sub-convective zone called as low wavenumber region creates strong structural excitation of panel. This happens because of TBL convective phase velocities match with structural wavespeeds and structural resonances present in the low wavenumber region cause a higher amount of response. This coupling between TBL wall pressure flucuation and structural modeshapes is measured by a parameter called

Joint-acceptance. Joint acceptance basically gives a measure of efficiency with which TBL wall pressure can excite the panel. Structural resonances become a strong spatial filter to the excitation. So that only very small amplitude, low wavenumber components are crucial for structural response. Hence estimation of low wavenumber frequency spectrum of TBL WPF is important in the prediction of wind noise power input [Bremner and Wilby, 2002].

Measurement of the low wave number region of the TBL wall pressure spectrum is essentially the measurement of a relatively low amplitude signal in the presence of much higher amplitude signals. Because of this reason, its not easy to capture these low wavenumbers in experiments. The accurate measurement of wall pressure fluctuations is not easy because of the probe sensitivity and the size of the transducers, noise contamination in low wave numbers as well as the existence of a wide range of scales in the pressure fluctuations with dynamic range. CFD numerical simulations provide an alternative and cost effective approach to capture them.

1.3.2 Deficiency of empirical TBL models

The existing empirical models for wall pressure fluctuations are based on flat plate boundary layer results with linearized source models. These models are deficient when applied to actual systems where there is pressure gradients over the cabin and the production roughness of the skin surface and presence of bluff bodies like side mirror in case of automobiles. CFD numerical simulations are only the cost effective way to serve as a remedy for obtaining the WPF's. There is an urgent need for the development of tractable numerical models for accurate prediction of wall pressure fluctuations which can accommodate the realistic configurations of vehicles and reduce the costs of wind tunnel testing.

In this project, funded by EXA corporation, a CFD software named PowerFLOW that is based on Lattice Boltzmann method (LBM) was used. It uses VLES turbulence model. The PowerFLOW solver has been developed by EXA corp and extensively used for aerodynamic simulations of automotive bluff bodies at low Mach flow [Crouse *et al.*, 2006b; Powell *et al.*, 2010; Senthooran *et al.*, 2005]. The unsteady wall pressure obtained from the CFD solver has been used to calculate the wind noise power input to the structure. The PowerFLOW generated WPF data is used to estimate the forcing function for the flow induced structural noise predictions in both spatial-frequency domain and wavenumber-frequency domain. Vibroacoustics response is predicted using Statistical Energy Analysis(SEA) tools. The tests were conducted at Purdue University wind tunnel as a joint colloboration between EXA corporation, Purdue University and Université de Sherbrooke.

1.4 Research problem

1.4.1 Computational aerodynamics and aero-vibro-acoustics

The main objective is to develop a Computational Fluid Dynamics (CFD) numerical model for turbulent boundary layer (TBL) excitation to predict the interior noise of automobile. Turbulent WPFs are characterised by mean square pressure, cross spectrum, correlation functions and wave number frequency spectrum. The modal response of a structure is given by the product of the WPF forcing function and structural acceptances. The aero-vibro-acoustics, the sound transmission and vibration response due to turbulent excitation will be calculated using modal and Statistical Energy Analysis (SEA) approach. The numerical procedure is applied for a plate-cavity system and validated with experiments in wind tunnel. Also correlation between exterior WPF and interior noise will be investigated once the model is validated. This methodology will be generalized for the prediction of the interior noise inside a passenger car using SEA tools. In this project, the interior noise generated by turbulent wall pressure fluctuatios are predicted using a combination of CFD and SEA tools without the requirement of expensive testing of full model cars in wind tunnel.

1.4.2 Test cases considered

The main aerodynamic noise sources in a car are A-pillar and side mirror, which are the focus of the current study. A custom made wind-tunnel plate-cavity system has been designed to represent plate as the side window and cavity as car cabin so as to capture the physical phenomenon of aerodynamic source excitation. The wind tunnel with the plate-cavity system has been designed and built by Purdue University in collaboration with EXA corporation. The bluff bodies A-pillar and side mirror have been represented by a flat fence inclined at 55° to the wind tunnel floor and a generic side mirror oriented at −30° to the flow path as shown in Figure 1.4 and Figure 1.5 respectively. The schematic of the plate-cavity excited by TBL is shown in Figure 1.4. A flat plate corresponding to a typical car side window size is flush mounted on the wind tunnel floor using foam pads. The cavity is made anechoic as shown in Figure 1.5 using foam wedges with microphone placed at center of the cavity for measurement. The walls of the cavity are filled with sand to avoid coupling. More details of the wind tunnel experimental setup can be found in [Park *et al.*, 2004]. The flat plate excited by TBL flow radiates the sound into the cavity. CFD simulations were also carried out to mimic the experimental wind tunnel tests with same specifications. The assumptions in determination of WPF are described in 1.4.3.

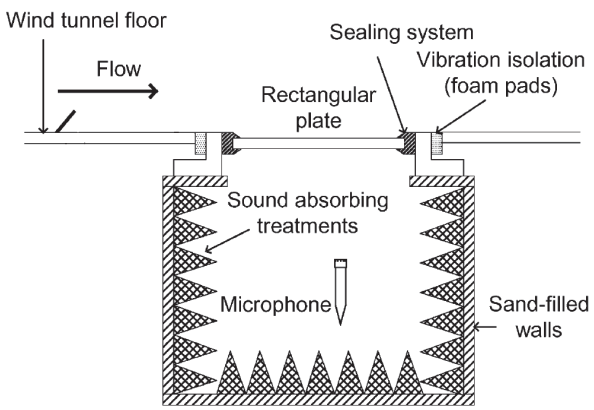

Figure 1.4 Schematic of Flat fence on plate-cavity system in wind tunnel [Park *et al.*, 2004]

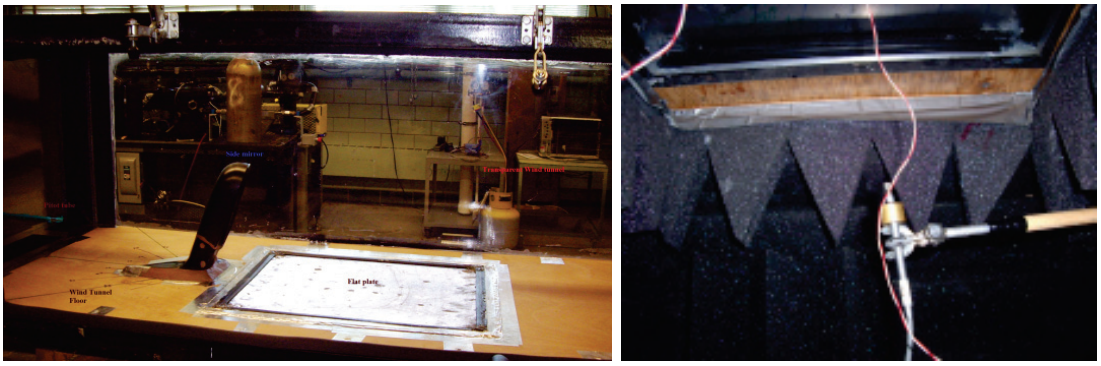

Figure 1.5 Side mirror(left) and cavity microphone (right) in wind tunnel [Caillet, 2008]

1.4.3 Assumptions in plate-cavity excited by TBL

1. Panel vibration does not influence the TBL (no fluid loading)
2. TBL flow is fully developed and three dimensional in nature
3. Turbulent wall pressure excitation and vibro-acoustics are decoupled
4. Flow over flat rigid smooth surface without any surface irregularities on the plate
5. TBL WPF are weakly time stationary and space homogeneous random processs functions defined by second order statistics

1.5 Objectives of research

The main objective is to develop an efficient approach to compute TBL power input using CFD (PowerFLOW) predicted WPF and estimate vibro-acoustics for two test cases namely fence and side mirror. In simple words this project address the question "How to use PowerFLOW WPF data to calculate wind noise input power to a vehicle structure ?"

Specific objectives

1. Conduct an unsteady CFD simulation to finely resolve wall-pressure for two test cases (flat fence and side mirror)
2. Present three methods to calculate TBL power input using CFD WPF
3. First method: Derive an empirical model from CFD predicted wall-pressure coherence and evaluate TBL noise input power and validate on two test cases
4. Second method: Estimate TBL power input in wavenumber-frequency domain using the CFD WPF and validate
5. Third method: Random sampling of CFD derived TBL WPF excitation to evaluate TBL power input and validation
6. Compare and discuss the pros and cons of the various methods

1.6 Outline of thesis

The present thesis is organized into five chapters.

Chapter 1 gives a brief introduction of the automobile interior noise sources and importance of aerodynamic WPF to the interior noise at high speeds. The challenges in the estimation of low wavenumber WPF are discussed. The main objective of this thesis is to propose three methods to convert the CFD WPF to TBL power input to the structure. 1) Identification of empirical TBL model parameters from unsteady CFD WPF 2) TBL power

input in wavenumber-frequency domain using CFD WPF 3) Random sampling of TBL excitation.

Chapter 2 presents the literature review on various methods to estimate unsteady WPF. These methods are empirical models, CFD tools and wind tunnel experiments. Different methods to predict the interior noise due to TBL excitation are reviewed with a focus on energy based methods (SEA).

Chapter 3 deals with the determination of empirical TBL model parameters using unsteady CFD WPF obtained from PowerFLOW. These empirical models for WPFs are described in terms of space-frequency domain or wave number-frequency domain. Mean flow and unsteady CFD analysis on the flat fence and side mirror are discussed along with experimental validation. A wavenumber-frequency analysis is done for these two bluff body cases to assess the spatial temporal characteristics. TBL model parameters are estimated in small patches of quasi-homogeneous zones on the plate that are classified based on autospectra in terms of decibels (dB) and mean skin friction maps. Finally vibroacoustics of plate-cavity system are determined using the empirically identified TBL parameters and validated with experiments.

In Chapter 4, The wavenumber description of CFD predicted WPF is used to compute the TBL power input and calculate the vibro-acoustics based on Rayleigh-Ritz approach. The efficiency of coupling between TBL WPF and structural modes is characterised by a non-dimensional parameter "joint acceptance". Joint acceptance was calculated in wavenumber domain and spatial domain to compare the computational time. Experiments were conducted at Purdue University wind tunnel for the two cases(supplied by Exa Corp). The validations are performed using the shared experimental data.

Chapter 5 focuses on a deterministic approximation of CFD-derived TBL WPF using random sampling technique. This method involves treating the excitation as stationary and homogeneous spatial random process. Cholesky decomposition was used to reduce the space correlated excitation components to multi load excitation with random phases. Finally structural response computed with random sampling was compared with that of FEM based deterministic approach.

Chapter 6 gives the conclusions and perspectives for future research with necessary recommendations.

CHAPTER 2

LITERATURE REVIEW

2.1 Overview

Prediction of interior noise due to turbulent excitation can be divided into a two-step problem assuming that turbulent flow excitation and vibro-acoustic response of the structure are decoupled. The decoupling assumption means that turbulent source generation and its propagation are separately calculated which makes the computation more tractable. The first step is to accurately estimate the turbulent wall pressure on the panel and the second step would be to convert the wall pressure into the power input to the panel. The focus of this chapter is to review different modeling methods to estimate turbulent wall pressure fluctuations (WPF). These modeling methods can be categorized into experiments in wind tunnel, empirical models and computational fluid dynamics (CFD). A detailed comparison of TBL WPF estimation methods with application to automobile turbulent flows were discussed. Most widely used empirical models for modelling the turbulent wall pressure are presented according to their chronology of publication. With the recent development of supercomputers CFD tools have become a popular choice for modelling turbulence for real and complex flows. Numerical simulation approaches used in industry to model and analyze turbulent flow across side mirror and A-pillar flow are discussed. These turbulent flows across side mirror and A-pillar are categorized as separated/reattached flows, which have adverse pressure gradients and recirculations at the separation points. The measurement challenges in conducting experiments in wind tunnels to measure the wall pressure are also discussed. Finally an overview of vibro-acoustic numerical tools like element based methods (FEM and BEM)and energy based methods (SEA) to predic the sound radiated from the panel excited by TBL are discussed. A summary of conclusions drawn from the literature review presents the objectives of the thesis and appropriate methodologies to meet the objectives. The objective of this review is to determine a tractable numerical approach for predicting the wall pressure and power injected to the panel due to TBL excitation. In otherwords, how we can convert the unsteady wall-pressure data to power injected and thereby estimating the sound radiated into cavity ?.

2.2 Mechanism of aerodynamic/TBL excitation

Many of the engineering applications involve complex fluid flows over structures like the road vehicles, aerospace vehicles and submarines. Understanding the turbulence and conceptualizing the physical phenomenon behind the fluid motions has been a great challenge for fluid dynamicists and engineers. The complexity and obscure nature of turbulence arises due to the reason that every flow regime is distinct in its own topology and hence canonical models are the best way to study the flow physics in depth. In a classical text book by [Hinze, 1975] on turbulence, turbulent flows have been categorized as i) free turbulent flows and ii) wall turbulent shear flows. Jet flows and wake flows fall into the first category of free turbulent flows as flows are unbounded without any wall (rigid surface). Flow around rigid bodies (boundary layer flows) and channel/pipe flows falls into the secondary category of wall bounded flows. The study of the fluid flow around rigid bodies is termed as external aerodynamics. The rigid bodies may be a streamlined body like aerofoil or bluff bodies like A-pillar and side mirror in car. The physical mechanism of flow induced noise can be explained with a simple flat plate turbulent flow coupled with cavity as shown in Figure 2.1.

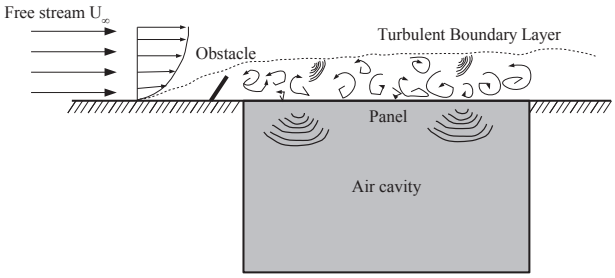

Figure 2.1 Schematic of plate-cavity system excited by TBL

When a fluid flows over a surface, at a certain vicinity of the surface the flow velocity reaches close to free stream velocity. In this region significant viscous stresses are present with fluctuating pressures and velocities. Due to the viscous drag in this layer shear stress is developed near to surface. This imaginary layer close to the surface is termed boundary layer. The boundary layer thickness develops over the laminar, transition and turbulent regions. In the turbulent region, flow is random and chaotic in nature with strong pressure fluctuations. The intense turbulent wall-pressure fluctuations on the surface can be classified as "pseudo-sound" and "sound" based on their characteristics. The pressure fluctuations that do not follow acoustic wave equation are convected with flow and hence named as "pseudo-sound" or sound-like pressure. Since sound is a small amplitude pressure fluctuation with irrotational compressible motions satisfying the wave equation [Dowling, 1984]. In simple terms "pseudo-sound" is non-propagating or convective component and

"sound" is propagating component. Both the turbulent sources "pseudo-sound" and "sound" excite the panel surface to radiate sound into the cavity. It is impossible to separately measure "pseudo-sound" and "sound" from the wall pressure fluctuations because the microphone picks both the pressure signals. The turbulent "sound" sources excite the panel surface similar to an acoustic excitation of a structural panel. Although the turbulent "sound" is a small fraction of the total pressure fluctuations, in case of a low Mach number flow, the low wavenumber pressure components and "sound" pressure components are the strong sources for the panel excitation. The turbulent "sound" source can be modelled as monopoles, dipoles and quadrupoles based on unsteady flow generation mechanism. In a turbulent boundary layer flow at low Mach number, the turbulent "sound" is dominated by dipole sources and hence the power radiated is sixth power of flow velocity [Crocker, 2007].

2.3 Features of separated and reattached flows

Turbulent shear flows may be divided into wall turbulent shear flows (wall bounded flows, boundary layer flows) and free turbulent flows (jet flows, wake flows) [Hinze, 1975]. Another classification of turbulence is based on the number of turbulence quantities required to describe flow characteristics in each direction. Isotropic turbulence is the simplest type of turbulence since it requires minimum number of quantities and relations to describe the flow structure as it is independent of direction. In this study we are concerned about boundary layer flows i.e flow around rigid bodies where the wall turbulence remains confined to a relatively thin layer along the surface of the body and the boundary layer develops in the downstream to a undisturbed free stream. Boundary layer flows over streamlined and bluff bodies with adverse pressure gradients are major source of flow noise due to the strong flow separations. Understanding the physical behaviour of separated and reattached flows are of major importance for reducing the aerodynamic noise in automobiles and trailing-edge noise in airfoils. The mechanism of flow separation and reattachment for a typical bluff bodies is best studied with a canonical case of backward facing step as shown in Figure 2.2. When a high velocity fluid flows past a body, flow separation happens at the sharpest section of the body or at any point on the surface depending on the pressure gradient, flow velocity and surface roughness. Flow separation occurs mostly in adverse pressure gradient situations with positive pressure rise in the direction of flow. In the immediate vicinity of separation, there is a low pressure region that is created behind the body where recirculation and flow reversals happen due to the encapsulated fluid or so-called dead air as shown in Figure 2.3. In addition to the separation, a wake is generated downstream of the body that consists of interacting shear layers. Depending on the body shape, the separated flow reattaches the

surface and follows the wake. At certain Reynolds number of the flow, periodic oscillations of small fluid zones called as *vortices* are noticed in the wake region due to the interaction between two separated flow streams around the body. This phenomenon is often referred to as vortex shedding and quantified by vortex-shedding frequency or Strouhal number. The flow-separation mechanism is also noticed in streamlined bodies like airfoil near the leading edge or trailing edge depending on the angle of attack and flow velocity. The aftermath of flow separation in airfoils leads to *stalling* effect, drastically reducing the lift force and increasing the drag.

According to [Simpson, 1996] the term 'separation' must mean the entire process of 'departure' or 'breakaway' or the breakdown of boundary-layer flow. Any sudden thickening of the rotational flow region next to a wall and significant values of the normal-to-wall velocity component must accompany breakaway, or else this region will not have any significant interaction with the free-stream flow [Castro and Haque, 1987; Driver and Johnston, 1990]. This unwanted interaction causes a reduction in the performance of the flow device and source of flow noise, for example, aerodynamics of bluff bodies, loss of lift on an airfoil and loss of pressure rise in a diffuser. In a steady time-averaged two-dimensional flow one can assume that zero wall shear stress would be the point of separation, but in an unsteady ensemble-averaged two-dimensional flow the wall shear stress can change sign with flow reversal, but without 'breakaway'. Conversely the breakdown of the boundary-layer concept can occur before any flow reversal is encountered. In three-dimensional flow the rotational layer can depart without the wall shear stress necessarily falling to zero; the wall shear is zero only at the singular points.

2.3.1 Backward facing step

To understand the fluid physics behind the turbulent separated and reattached flows, we consider the widely used two dimensional example of backward facing step. Figure 2.2 consists of upstream boundary layer detaches, recirculation zone, forming a free shear layer, dividing streamline in reattachment zone which are typical characteristics of a separated/reattached flows commonly noticed in automotive pillars and mirrors. [Simpson, 1996] has reviewed turbulent behavior of separated and reattached flows due to strong adverse pressure gradients for backward facing-step test case. Dettachement is the location where the boundary layer flow leaves the wall, the locus of points where the limiting streamline of the flow leaves the surface. Reattachment is the locus of points where the limiting streamline of time-averaged flow rejoins the surface. Separation is the total process of detachment, recirculation, flow free-shear layer and recirculating zone. The recirculation zone consists of fluid created by pressure forces with flow reversals or low velocity fluid

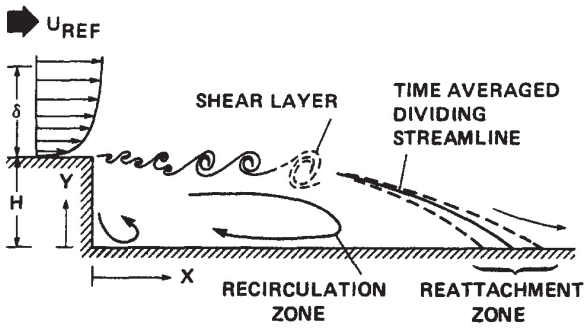

Figure 2.2 Flow topology for backward facing step [Driver *et al.*, 1987]

movements. The simplest test case for reattaching flow is backward facing step widely used to validate the numerical codes. When the external flow strikes the backward facing step, the upstream boundary layer detaches at the sharp corner forming a free shear layer. The separated shear layer curves sharply downwards in the reattachment zone and impinges on the wall. Part of shear-layer fluid is deflected upstream into the recirculating flow by strong adverse pressure gradient. The shear layer is subjected to the effects of adverse pressure gradient and strong interaction with the wall in the reattachment zone. A rapid decay of shear stress occur within reattachment zone. The recirculation zone may have some little back flow velocity. A detailed blow up schematic of separation zone with dead air and dividing streamlines are shown in Figure 2.3.

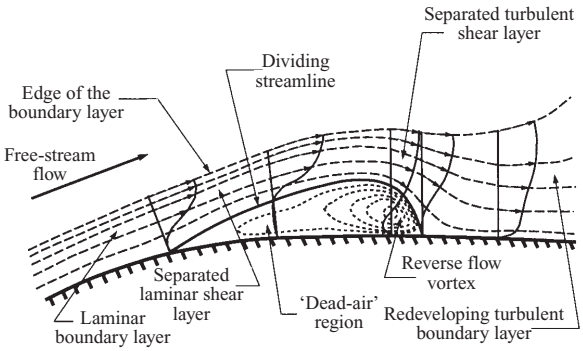

Figure 2.3 Structure of boundary layer separation and reattachment showing separation bubble, [Horton, 1968]

2.3.2 Boundary layer with pressure gradients

In this section, a brief description of the boundary layer equations with pressure gradients have been discussed as per [White, 2006]. In this direction, let's consider the boundary layer equations for simple steady two dimensional flow in the xy-plane, neglecting the gravity effects. The boundary layer coordinate system is defined by the x-axis parallel to the direction of flow (streamwise) and y-axis perpendicular to the streamwise direction. The boundary layer equations governing the two dimensional steady incompressible flow are given in [Çengel and Cimbala, 2006]

$$\frac{\partial u}{\partial x} + \frac{\partial u}{\partial y} = 0 \tag{2.1}$$

$$u\frac{\partial u}{\partial x} + v\frac{\partial u}{\partial y} = -\frac{1}{\rho}\frac{\mathrm{d}P}{\mathrm{d}x} + v\frac{\partial^2 u}{\partial y^2} \tag{2.2}$$

At $y = 0$, $u = 0$ and $v = 0$ the velocity is zero near the wall (with no slip condition i.e there is no relative velocity between fluid close to wall and wall surface). Plugging these boundary conditions in above equations reduces the left side of boundary-layer equations to zero and shear term is balanced by second derivative of u at the wall. Since the pressure gradient does not change from inside the boundary layer and in outer flow region, one can use the same Bernoulli's equation for both regions. Bernoulli's Equation at $y = \delta$ outside the viscosity influence zone close to the top of boundary layer where $u = U(x)$ is $\frac{P}{\rho} + \frac{1}{2}U^2 = constant$. thereby differentiating the Bernoulli's equation with respect to x leads to the relation between the pressure gradient term and intertial term as follows

$$\frac{1}{\rho}\frac{\mathrm{d}p}{\mathrm{d}x} = -U\frac{\mathrm{d}U}{\mathrm{d}x} \tag{2.3}$$

Finally the boundary layer equations for two dimensional flows with pressure gradients are given

$$u\frac{\partial u}{\partial x} + v\frac{\partial u}{\partial y} = U\frac{\mathrm{d}U}{\mathrm{d}x} + v\frac{\partial^2 u}{\partial y^2} \tag{2.4}$$

Figure 2.4 shows the schematic of the boundary layer velocity profile development over a curved surface with favorable pressure gradients at the leading edge and adverse pressure gradients at the trailing edge. A favorable pressure gradient is also termed a negative pressure gradient, where as a adverse pressure gradient in the flow is termed a positive pressure gradient which is the cause of boundary layer separation. The separation point is located on the surface at which the slope of the velocity profile is zero. Flow reversals and break down of boundary layer is noticed with negative shear forces at the trailing edge of the curved surface. After the separation point, the classical boundary layer approximation

theory of dividing the flow into viscous and inviscid flows is not applicable. The point of inflection is a important criterion for study of boundary-layer stability and transition [Liepmann, 1943]. The height of the point of inflection from the wall indicates the strength of the pressure gradient of the flow. Another noteworthy feature of pressure gradient flows is the presence of *point of inflection* that is defined as the point where the slope of $\frac{\partial u}{\partial y}$ changes sign and thereby $\frac{\partial^2 u}{\partial y^2} = 0$. In *favorable (negative)* pressure gradients , the pressure gradient $(\frac{\mathrm{d}p}{\mathrm{d}x})$ is negative creating a suction zone that favours accelerating flow to be attached to the surface which avoids separation. With $\frac{\mathrm{d}p}{\mathrm{d}x} < 0$, the other gradient terms in Equation 2.3 $\frac{\mathrm{d}U}{\mathrm{d}x}$ becomes positive and second partial derivative of u at the wall $\frac{\partial^2 u}{\partial y^2}_{y=0}$ share the similar sign with pressure gradient term. For favorable pressure gradient flow, the pressure gradient basically favours the flow to be attached to the surface without separation and there is no point of inflection. In zero pressure gradient flow, there is no pressure gradient $\frac{\mathrm{d}p}{\mathrm{d}x} = 0$ which implies linear growth of u with respect to y and Blasius boundary layer velocity profile is applicable in zero pressure gradient flows in case of laminar flows (low velocity). For zero pressure gradient flows the point of inflection is approximately at the wall. In case of *adverse (positive)* pressure gradients , the pressure gradient $\frac{\mathrm{d}p}{\mathrm{d}x}$ is positive with decelerating flow, creating a pressure zone that facilitates flow separation. With adverse pressure gradient$(\frac{\mathrm{d}p}{\mathrm{d}x} > 0)$, the other terms in the two dimensional boundary layer Equation 2.3 becomes $\frac{\mathrm{d}U}{\mathrm{d}x}$ as negative and second partial derivative of u at the wall $\frac{\partial^2 u}{\partial y^2}_{y=0}$ as positive. Flow once separated from surface of the body, breaks down creating flow reversals and separation bubble depending on the strength of positive pressure gradient. For adverse pressure gradients, the point of inflection (change of slope) occurs above the wall in the boundary layer flow and its height from the wall surface increases with increase in the strength of positive pressure gradients. The boundary layer thickness increases for a decelerating flow with adverse pressure gradients. In a separated and reattached flows, there exists a point where the reversed flow that meets the main flow stream known as reattachment point or reattachment zone. The wall shear stress is proportional to velocity gradient $\frac{\partial u}{\partial y}$ given by $\tau_w = \mu(\frac{\partial u}{\partial y})_{y=0}$, i.e at the wall. When the streamwise velocity profile is having a zero slope at the wall $(\frac{\partial u}{\partial y} = 0)$, the wall shear stress approaches zero. This location defines the separation point. Depending on the flow velocities and surface geometries (2D or 3D) the separation point can vary from a small point to a larger zone.

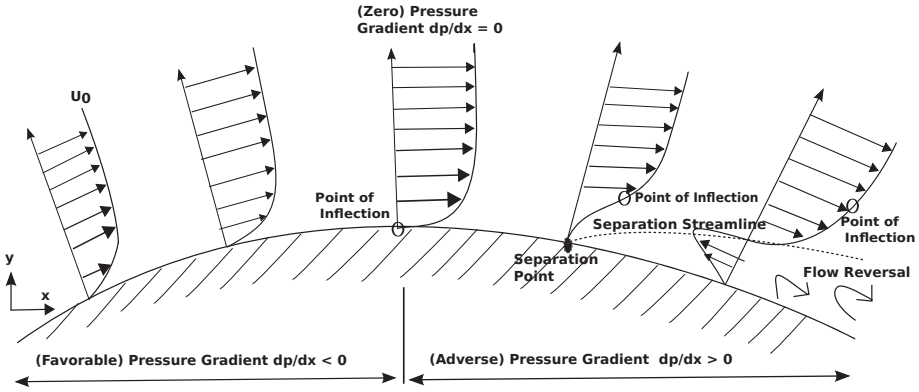

Figure 2.4 Favorable and adverse pressure gradients in boundary layer separation [Leishman, 2006]

2.3.3 Boundary layer wall scaling parameters

In this section we are focusing on the wall variables that characterize the statistical properties of wall pressure also called boundary layer parameters. These boundary layer parameters vary from the near vicinity of the wall to the free stream and can be classified as inner and outer variables. Inner variables are parameters that are describing the inner wall layer in dimensionless velocity profiles, and outer variables are corresponding to the outer layer beyond the boundary layer effects. Boundary-layer parameters used frequently in scaling the wall pressure spectrum and in deducing other physically significant dimensionless parameters are presented with equations. For a detailed review on boundary layer theory refer to the well known book by [Schlichting and Gersten, 2000]. In a ideal inviscid flow the fluid close to the wall has a finite relative speed, even with a small amount of viscous friction the local speed near the wall becomes zero that creates a small region termed as "boundary layer". Wall shear effects extends from surface to the free stream where viscosity has no effects and measured in terms of free stream velocity U_∞ and boundary layer thickness, δ.

Based on the dimensional analysis of normalised mean velocity profiles in terms of y^+, turbulent wall flow can be divided into three regions a) Inner wall layer(linear) b) Outer Layer(velocity-defect zone) c) Overlap Layer (logarithmic zone) as shown in Figure 2.5. Viscous shear dominates in *Inner wall layer* region where the velocity gradient is independent of the distance from the wall and dependent on wall shear. Hence also termed linear region with governing equation.

$$u = \frac{\tau_w y}{\mu} \tag{2.5}$$

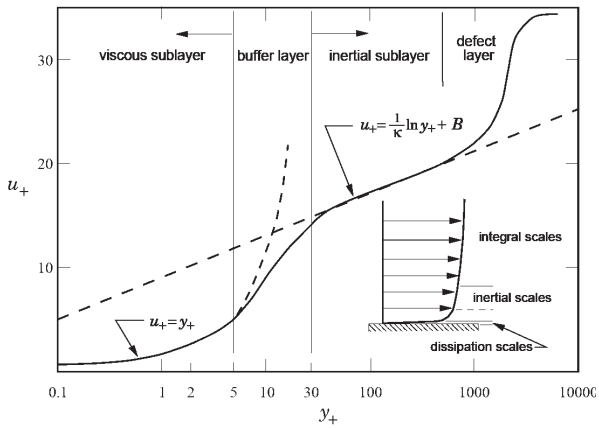

Figure 2.5 Inner outer and overlap layer laws relating velocity profiles in turbulent wall flow. [White, 1999]

where u denotes the streamwise velocity, y is the distance from wall, τ_w is wall shear stress and μ is the dynamic viscosity of fluid. Using dimensionless parameters $u^+ = \frac{u}{u_\tau}$, $y^+ = \frac{yu_\tau}{\nu}$ and friction or shear velocity $u_\tau = \sqrt{\frac{\tau_w}{\rho}}$. ν is the kinematic viscosity of the fluid. The above equation can be written in a dimensionless format

$$u^+ = y^+ \tag{2.6}$$

where u^+ denote the dimensionless velocity component on the streamwise direction and y^+ is dimensionless wall distance. The inner wall region is sub-divided into viscous sublayer and buffer layer that is an overlap of linear region and logarithmic region. In the logarithmic region the turbulence activity is the greatest and the velocity gradients are proportional to the distance from the wall expressed in an dimensionless equation form also known as *Law of the wall* .

$$u_+ = \frac{1}{k} \ln y_+ + B \tag{2.7}$$

where k is the von Kármán constant empirically determined and its value is ≈ 0.4 for all types walls and B is the intercept of the logarithmic law that depends on degree of surface roughness of the wall. For smooth walls its a constant value of 5.

The outer layer is characterized by having constant eddy mixing length with velocity distributions expressed by velocity defect law. In a ideal flow situation, logarithmic law of wall would be sufficient to characterize the velocity profiles for two regions except the outer

layer. With turbulent flow that have favorable and adverse pressure gradients, there always exist an outer layer that represents the wake like behaviour of the boundary layer. In order to represent the outer layer phenomenon correctly, [Coles, 1956] proposed to extend the logarithmic law of wall with an added wake function to velocity defect law and termed it as *Law of wake* . Together with law of wall, logarithmic law and defect law, its possible to approximately predict the velocity profile for any turbulent shear flows to major extent. The law of wake is given by

$$\frac{u_\infty - u}{u_\tau} = \frac{1}{k}\ln y + 1.38[2 - W(\frac{y}{\delta})] \tag{2.8}$$

where $W(\frac{y}{\delta}) = 1 + sin[\frac{(\frac{2y_2}{\delta} - 1)\pi}{2}]$

As $y \to \delta$, $U \to U_\infty$ in the wake region, the notion of boundary layer thickness δ parameter does not make sense. so an outer boundary layer scale called *displacement thickness* δ^* based on mass balance is often used that is given by.

$$\delta^* = \int_0^\infty [\frac{u_\infty - u(y)}{u_\infty}]dy \tag{2.9}$$

Typically δ^* varies from 1/8 to 1/5 δ based on the surface roughness and pressure gradients. Another length scale called *momentum thickness*, θ based on momentum balance given by the following equation

$$\theta = \int_0^\infty \frac{u(y)}{u_\infty}[1 - \frac{u(y)}{u_\infty}]dy \tag{2.10}$$

Displacement thickness, δ^* and momentum thickness θ are related by the shape factor, H given by

$$H = \frac{\delta^*}{\theta} \tag{2.11}$$

Strouhal number

In case of a flow over cylinder, at a certain range of Reynolds number, there exists a periodic vortex shedding phenomenon behind the cylinder known as the von Kármán vortex street. Vortex street are due to the fluctuating interaction between two separated vortices on both sides of the cylinder past the separation. The frequency of vortex shedding is given by the so called dimensionless number *Strouhal number* defined by

$$St = \frac{\omega L}{U_\infty} \tag{2.12}$$

where ω is vortex shedding circular frequency, L is the characteristic length of bluff body and U_∞ is free stream velocity. In external flow simulations, the Strouhal number helps as a quick and simple validation check for CFD analysis of bluff bodies and also used in dimensional analysis of pressure spectra to correlate different flow configurations.

2.3.4 Flat plate boundary layer parameters: Exact and approximate methods

The basic concept of boundary layer analysis is to separately calculate the viscous effects in the proximity of surface and patch the remaining inviscid flow above boundary layer. This concept is valid for thin boundary layers at high Reynolds numbers.

The interrelationships between the boundary layer parameters described above can be determined in closed form using exact and approximate methods like Blasius and von Kármán momentum integral methods respectively for simple flat-plate fluid flows with zero pressure gradient. Blasius method is used for solving laminar boundary layer flows and von Kármán momentum integral equations for both laminar and turbulent boundary layers. In 1908, Blasius, a student of Prandtl, studied an example of flow over a thin flat plate with zero pressure gradient to be able to solve for boundary layer equations in closed form. The steady flow is assumed over the semi-infinite flat plate. The velocity profiles at any point in time and space are assumed to be self-similar or also termed as equilibrium boundary layers, which implies they are characterised by mean velocity profile and the velocity profile at any position can be determined as a scaled values of boundary layer thickness, $\delta(x)$ function and free stream velocity, U_∞. Assuming the constant free stream velocity, the similarity velocity profile can be written as

$$\frac{u}{U_\infty} = f'(\eta) \quad \text{and} \quad \eta \ = y\left(\frac{U_\infty}{\nu x}\right)^{0.5} \tag{2.13}$$

where the η is the similarity variable, ν is the kinematic viscosity, x is the streamwise distance, y is the vertical distance in boundary layer thickness direction, $'$ denotes the differentiation operator with respect to η. $f(\eta)$ is the dimensionless streamwise function. Prandtl's boundary-layer equations in the form of partial differential equations simplifies into third order non-linear ordinary differential equation(ODE) using the Blasius similarity relations. This equation famously known as Blasius equation.

$$f''' + \frac{1}{2} f f'' = 0 \tag{2.14}$$

The corresponding boundary conditions for "no-slip" and "patching" becomes

At $y = 0$, $f(0) = f'(0) = 0$,

As $y \to \infty$, there by $f(\infty) \to 1$

The above three boundary conditions are enough to determine the solution of ODE. Blasius equation can be solved using numerical integration approaches like Runge-Kutta method also known as shooting method. The Blasius velocity profile $\frac{u}{U_\infty}$ is usually given in a tabular form with respect to $y(\frac{U_\infty}{\nu x})^{1/2}$. From the Blasius profile, at $\frac{u}{U_\infty} = 0.99$, which is the boundary layer thickness δ that occurs at $\eta \approx 5$. Hence boundary layer thickness can be given by $\frac{\delta}{x} \approx \frac{5}{(Re_x)^{0.5}}$.

The remaining laminar boundary-layer parameters like wall-shear stress, skin-friction coefficient, displacement thickness and momentum thickness can be determined in closed form as described in detail in [Schlichting and Gersten, 2000]. Another widely used approximate method to estimate these parameters is von Kármán momentum integral approach. Unlike Blasius method this integral approach is applicable to both laminar and turbulent boundary layers. The basic assumption in integral approach is steady incompressible flow with a guess estimate for its velocity profile. Von Kármán momentum integral equations are derived when Navier-Stokes equations are applied to selective region of boundary layer treating it as control volume and integration inside the control volume using guess estimate of velocity profile. The accuracy depends on the intuition in having a good guess estimate for velocity profile. In turbulent boundary-layer flows, momentum integral approach gives only time averaged quantities of boundary layer parameters instead of usual instantaneous values. Integrating the momentum balance equation along the vertical y direction till the boundary-layer thickness leads to von Kármán integral equation as shown below

$$\frac{d}{dx}(U^2\theta) + U\frac{dU}{dx}\delta^* = \frac{\tau_w}{p} \tag{2.15}$$

von Kármán integral equation is valid for incompressible boundary layer irrespective of flow is laminar or turbulent. Alternative simplified form of above equation in terms of shape factor and skin-friction coefficient

$$\frac{C_f(x)}{2} = \frac{\theta}{dx} + (2+H)\frac{\theta}{U(x)}\frac{dU}{dx} \tag{2.16}$$

where shape factor is $H = \frac{\delta^*}{\theta}$ and skin-friction coefficient as a function of streamwise direction x is given by

$$C_f(x) = \frac{\tau_w}{\frac{1}{2}\rho U(x)}$$

Both H and C_f are function of x of a turbulent flow with non-zero pressure gradient.

For flat plate turbulent flow with constant free stream velocity, once we know the assumed velocity profile and skin-friction coefficient as function of streamwise distance x, approximate time averaged quantities of boundary-layer parameters can be determined using momentum integral equation. Two kinds of empirical relations are available for guessing the velocity profile to derive boundary layer parameters for flat plate turbulent flow with zero pressure gradients. The first one would be the law of wall also known as log law that is given in section 2.3.3 and expressed as equation (2.7). The alternative option for simplifying the analytical calculation is *one seventh power law* that is expressed as

$$\frac{u}{U} \cong (\frac{y}{\delta})^{1/n} \text{ for } y \leq \delta \text{ and } \frac{u}{U} \cong 1 \text{ for } y > \delta$$

where the denominator n varies depending on the flow characteristics for example typical values are $n = 7$ for smooth flat plate , $n = 4$ for rough walls , $n = 2$ for laminar flows and $n = 5$ for smooth pipe flow. For the case of a turbulent flow over flat plate, the local skin-friction coefficient to follow this expression $C_f(x) = \frac{0.027}{(Re_x)^{1/7}}$ and the corresponding boundary-layer characteristics are derived.Substituting the $\frac{u}{U}$ and $C_f(x)$ in the definition of momentum-thickness provides expressions for momentum thickness in Equation 2.17, displacement thickness in Equation 2.18 and boundary layer thickness in Equation 2.19.

$$\frac{\theta}{x} \approx \frac{0.016}{(Re_x)^{1/7}} \tag{2.17}$$

$$\frac{\delta^*}{x} \approx \frac{0.02}{(Re_x)^{1/7}} \tag{2.18}$$

$$\frac{\delta}{x} \approx \frac{0.38}{(Re_x)^{1/7}} \tag{2.19}$$

The generalized interrelationships between boundary layer parameters for power law are given by Equations 2.20 and 2.21

$$\frac{\delta^*}{\delta} \approx \frac{1}{n+1} \tag{2.20}$$

$$\frac{\delta^*}{\theta} \approx \frac{n+2}{n} \tag{2.21}$$

For one seventh power law $n = 7$, $\frac{\delta^*}{\delta} \approx \frac{1}{8}$ and $\frac{\delta^*}{\theta} \approx \frac{9}{7}$. These expressions deduced from momentum-integral equation are widely used to have first approximate estimate of the boundary layer parameters and give a good start for CFD wall-function analysis.

2.3.5 Aerodynamic dimensionless numbers

Drag force is the net resultant of pressure and shear forces acting on the body in the direction of flow and lift force is the component of force acting in the direction normal to the flow.

$$\text{Lift coefficient} = C_L = \frac{L}{\frac{1}{2}\rho U^2 A}$$

$$\text{Drag coefficient} = C_D = \frac{D}{\frac{1}{2}\rho U^2 A}$$

where L is the lift force, D the drag force, $\frac{1}{2}\rho U^2 A$ is the dynamic pressure term and A the frontal area or planform area. Frontal area is used for calculation of drag for blunt or bluff bodies and planform area of streamlined airfoils bodies. Frontal area is calculated by projecting the body surface on to a normal plane in the flow direction. Planform area is the area as seen from top of the body.

$$\text{Pressure coefficient} = C_p = \frac{p - p_\infty}{\frac{1}{2}\rho U^2}$$

where $p - p_\infty$ is the static pressure difference

The skin-friction drag is due to the wall shear stress acting on the surface and varies with the viscosity of the fluid. On the other hand the pressure drag or form drag is due to the pressure forces varies mainly with pressure difference generated on the front and back of the body due to the shape of the body. Both drag and lift are dependent on angle of attack or flow direction. In case of a blunt flat plate whose plate area is perpendicular to flow direction, total drag is dominated by pressure drag since skin drag is zero due to the lack

of forces parallel to the surface. Similarly for a flat plate whose area is parallel to the flow direction, total drag is dominated by skin drag and pressure drag vanishes since there is only shear forces acting on the plate.

The lift and drag coefficients on the surface vary depending on the pressure distribution and flow profiles, so an average values of these coefficients for the entire body are determined by the integration of the lift and drag forces with respect to the length of the body. At $Re \geq 10^4$ typical values of C_D for bluff bodies such as half-cylinder, representative of a car side mirror is 0.7 and for streamlined bodies such as airfoils is 0.01. The ratio of lift to drag ratio for bluff bodies is typically around 0.1- 0.05 and for streamlined bodies like airfoil it is around 10 - 15 [White, 1999]. Laminar flows are very vulnerable to adverse pressure gradients compared to turbulent flows which resist the flow separation and hence separation is delayed.

2.3.6 Summary of boundary layer separation control techniques

Prevention of turbulent separation is done by many active and passive techniques [Gad-el Hak, 2001; Joslin *et al.*, 2005]. Some of the control methods are changing shape to streamlined body, blowing and suction, adding flaps to trailing edge, slats to leading edge of high-lift devices and adding surface corrugations to delay flow separation. In streamlining technique, drag coefficient is reduced by minimizing both pressure and friction drag with optimal length to diameter/width ratio. In suction technique, low pressure is created inside the body with narrow slits on the wall to have an attached flow. The other approach is by blowing tangentially into the boundary layer by using a wall jet to impart enough kinetic energy to avoid separation. Certain compliant coatings or corrugations/dimples are also used to reduced skin drag inspired from humpback whale fin "tubercles" skin texture. Recently, there has been talk on biomimicking the humpback whale fin for the leading edge of the wind turbine blades to reduce tip noise, but further studies are warranted.

2.4 Modelling turbulent boundary layer excitation

The first step in the estimation of response to turbulent excitation is to capture the turbulent wall-pressure fluctuations beneath the panel using experimental, simulation or empirical methods. Figure 2.1 represents such kind of turbulent excitation of the panel backed by cavity. The second step deals with the conversion of the wall-pressure fluctuations on the panel to input power. The coupling efficiency between the wall-pressure fluctuations and the panel mode shapes is expressed in terms of a non-dimensional parameter known as "Joint acceptance". This parameter describes the amount of wall pressure that is able

to excite the panel in its mode shapes. It requires a numerical algorithm to couple wall pressure and panel mode shapes. Any random excitation that is time and space stationary such as TBL excitation or diffuse field can be written as a product of auto and cross pressure spectra or wavenumber frequency spectrum. Wavenumber frequency spectrum is the spatial Fourier transform of wall-pressure spectra across the panel. The wall-pressure fluctuations were caused by the inherent random nature in the excitation. Statistical parameters are used to characterize turbulent wall-pressure fluctuations:

(i) Mean square pressure (second-order statistical parameters)

(ii) Frequency spectrum

(iii) Auto and cross-correlation functions (space-time)

(iv) Wavenumber-frequency spectrum (space-frequency)

Auto and cross-correlation functions in time domain are difficult to measure and estimate compared to wavenumber frequency spectrum due to the cumbersome nature of correlation calculation.Hence these time domain correlation functions are not widely used to express the TBL input excitation for the prediction of vibro-acoustics. With the availability of Fast Fourier Transform (FFT) algorithms, the computation of wavenumber frequency spectrum is more tractable and provides a direct physical appreciation of the turbulent excitation. Also most of the vibro-acoustic response calculations that are coupled with flow excitation are done in frequency domain due to presence of many industrial frequency domain solvers to determine structural mode shapes that interact with the turbulent wall-pressure excitation.

Usually the empirical models for WPF are expressed as a product of auto power spectrum of the pressure signal (point frequency spectrum)and cross-spectrum(two-point frequency spectrum). The auto power spectrum gives an idea of the spectral content in the signal whereas the cross spectrum gives the signal variation from point to point on the surface of the plate in frequency domain. The cross spectrum is obtained from the time Fourier transform of the correlation function of the pressure signal. Similarly the wave-frequency spectrum is obtained from the spatial Fourier transform of the cross spectrum. The excitation force on the plate is high usually when large wavelengths (low wave number) and phase velocities which match with structural wave speeds (normally much higher than the convection velocity of low Mach number flows) and acoustic radiation is associated with components with phase velocities which are equal to or greater than the components of the pressure field. Highest spectral levels of pressure fluctuations are those with convective ridge where Corcos model is applicable.

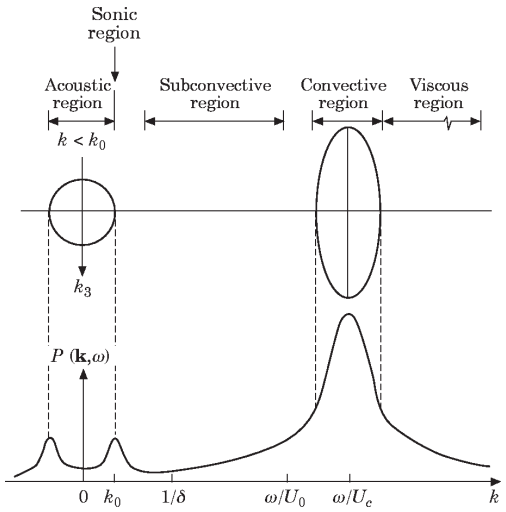

Figure 2.6 Schematic representation of wavenumber-frequency specrum at constant frequency depicting the variation regions [Howe, 1998]

The characteristic shape of the wavenumber-frequency spectrum at low Mach numbers is illustrated in Figure 2.6 for a fixed frequency and also for a fixed wavenumber. This spectrum can be characterized into five ranges i) the supersonic region ii) the sonic or acoustic region iii) the sub-convective region iv) the convective region centered at $k_c = \frac{\omega}{U_c}$ v) the viscous region. The strongest pressure fluctuations occur within the convective ridge centred on where is the convection velocity. [Bull, 1996] gives extensive review on estimation of turbulent wall pressure fluctuations from measurements and empirical models. He reviews the importance of estimation of low wave number components for marine applications and the estimation of convective ridge for the aerospace applications.

2.5 Empirical/Semi-empirical models for TBL wall-pressure fluctuations

Empirical models for TBL wall pressure fluctuations can be divided into one-point frequency spectrum models and two-point cross spectrum or wavenumber-frequency spectrum models. The one-point empirical models are derived from curve fitting for the roll-off (change in slope) of normalised frequency spectrum obtained from measurements in various frequency ranges. The two-point empirical models available in literature are also derived from curve fitting the multiple data set of measurements with varying spacing of probes and flow speeds. In contrast to the empirical models, the semi-empirical models include certain theoretical relationships involving wall pressure and turbulent velocity fluctuations along with inputs

from experimental data. Recently new semi-empirical models are being developed using cost effective numerical simulation based on RANS in combination with experimental data. These kind of semi-empirical models also known as "statistical models" in literature. They make use of the cost efficient time averaged RANS solutions as inputs instead of the conducting an expensive wind tunnel tests. Statistical models are presented in details in the Section 2.6.2. In the following sections, a brief review of the empirical and semi-empirical models that exist in literature are presented along with their limitations and suitability for various applications.

2.5.1 One-point wall-pressure spectrum models

One-point wall-pressure spectrum is also known by autospectrum or power spectral density. In addition to the two-point spectrum, the one-point spectrum is an important characteristic of WPF that needs to be measured or computed, for an accurate prediction of radiated sound. In an effort to find a one-point frequency spectrum with single scaling for the entire frequency range, a comparison of various one-point models have to be performed using three scaling laws based on inner, outer and mixed variables. These scaling laws are used to calculate the dimensionless wall pressure spectrum and dimensionless frequency. The inner, outer and mixed variables are discussed in boundary layer parameters Section 2.3.3. [Keith *et al.*, 1992] presented a comparison of dimensionless one-point frequency spectrum based on scaling laws obtained from various test data available in literature. The effect of scaling in each frequency region of spectrum were studied but they were unable to find a particular scaling that collapses entire data set to a single curve due to transducer size attenuations resulting from sensor spatial resolution. More recently [Hwang *et al.*, 2009] also compared the one-point frequency spectrum from notable semi-empirical models with published experimental data for various Reynolds numbers and flow parameters. In their work, the transducer size attenuations in measured data were corrected with sensor size correction factors to represent the actual data. According to [Hwang *et al.*, 2009] study, [Goody, 2004] model was recommended as the best overall prediction for one-point wall-pressure spectrum in the entire frequency range incase of zero pressure gradient flows. A schematic of one-point spectrum roll-off inside each region of the boundary layer is given in Figure 2.7. Unfortunately there seems to be no single scaling that suits well for the entire frequency range due to the observed data scatter as noticed in Figure 2.8.

Among the existing one-point spectral models , [Mastrello, 1969], [Cockburn and Robertson, 1974], [Efimtsov, 1982, 1984], [Smol'yakov and Tkachenko, 1991] are developed based on experimental datasets obtained from aerospace applications with high Mach numbers. The basic idea is to generate a curve fit for the normalised wall-pressure spectrum in

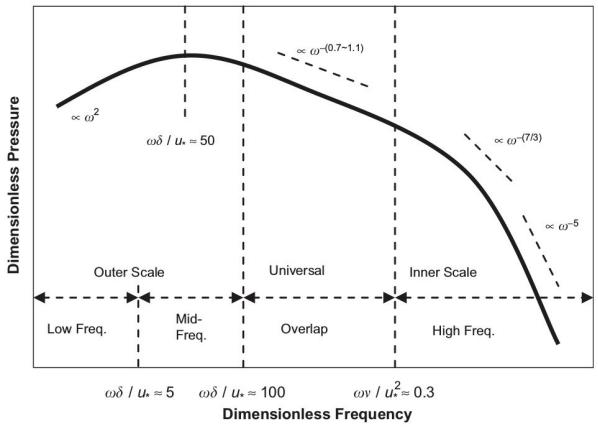

Figure 2.7 Generalised schematic of roll-off of one-point frequency spectrum in different scales by [Hwang *et al.*, 2003]

each frequency range from the earlier published data with different flow conditions. The normalised wall-pressure spectrum can be obtained from boundary layer parameters namely inner, outer or an mixed variables as discussed in Section 2.3.3. The other set of semi-empirical models such as [Chase, 1980], [Witting, 1986], [Chase, 1987] and [Smol'yakov, 2000] are based more on the physical phenomena of turbulent mean shear interactions and turbulent velocities fluctuations rather than curve fits of experimental dataset. [Chase, 1980] model forms the basis for the development of recent semi-empirical model by [Goody, 2004] which includes Reynolds number effect on pressure spectrum. [Chase, 1980] model is also known as "Chase-Howe" model due to the fact that [Howe, 1998] presented a simplified form. Until recently [Goody, 2004] one-point spectral model was used in combination with Corcos two-point spectrum to predict the turbulent boundary layer noise in a fully analytical approach. It has been observed by [Caro *et al.*, 2006] that Goody model under predicts when compared to the the one-point spectrum calculated from incompressible unsteady LES simulation using FLUENT for half-cylinder case. [Goody, 2004] model is not suitable for predicting the wall-pressure spectrum for turbulent boundary layers with pressure gradients.

The empirical/semi-empirical models discussed earlier are strictly limited to zero pressure gradients flows. To overcome this problem researchers like [Rozenberg *et al.*, 2012], [Catlett *et al.*, 2015], [Kamruzzaman *et al.*, 2015] and [Hu and Herr, 2016] extended [Goody, 2004] model to accommodate the effects of pressure gradient in wall-pressure spectrum model. These semi-empirical models need boundary layer parameters as inputs that can obtained from experiments or steady CFD simulations. [Rozenberg *et al.*, 2012] model extended the Goody model to incorporate the effects of adverse pressure gradient effects with help of Clauser's parameters and wake strength. [Hu and Herr, 2016] developed a new empirical

spectral model for adverse pressure gradient with different set of boundary layer scaling parameters compared to that of earlier researchers. These parameters are obtained from curvefitting the experimental spectral data. Experiments were conducted on rotatable NACA 0012 airfoil with various flow conditions to obtain the flow statistics needed for the empirical model and its validations. They have compared one-point spectra generated using empirical model with boundary layer parameters from [Catlett *et al.*, 2015] and [Schloemer, 1967].

It can be concluded that no single empirical model was able to predict one-point spectrum over the entire frequency range while using boundary layer parameters obtained from a third party experiments. In otherwords, each empirical model developed predicts well with its own measured set of parameters and becomes case dependent. In recent times, cost effective and time efficient steady RANS solvers have been used to develop statistical and stochastic models for wall pressure fluctuations under complex flow configurations where zero pressure gradient empirical models are not applicable. Although there exist a degree of empiricism in the statistical models but still majority of the information like mean and fluctuating quantities are derived from RANS simulations and validated with experimental spectra. More details will be discussed in Section 2.6.2. For a comprehensive review on spectral properties of wall-pressure fluctuations and their estimation, the reader is advised to refer a monograph by [Juvé *et al.*, 2015].

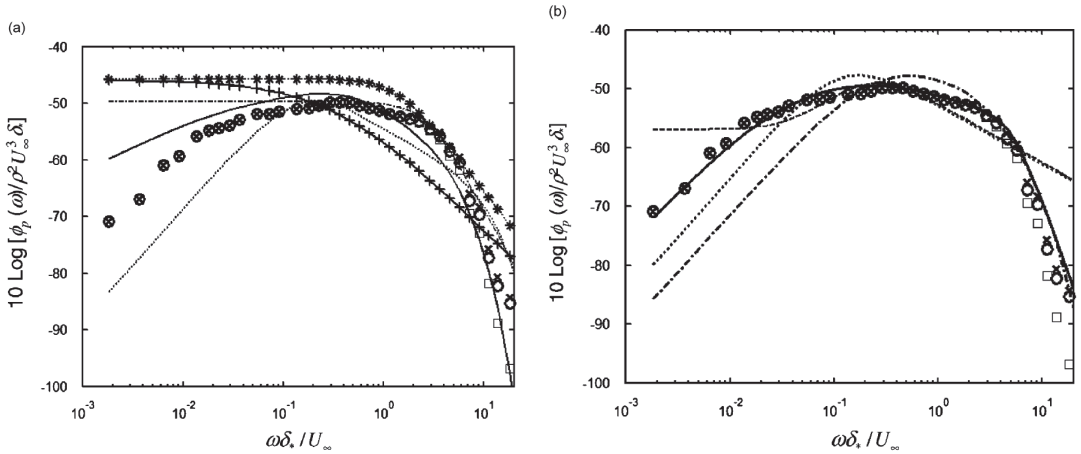

(a) Predicted spectra using model by (——) Maestrello, (—|—) Cockburn–Robertson, (—·—·—) Efimtsov, (·····) Witting, (···◆···) Smol'yakov–Tkachenko. (b) Predicted spectra using model by (– – – –) Chase, (▪▪▪▪▪▪▪) Chase–Howe, (— ▪ — ▪) Smol'yakov, (——) Goody. (○) the measured data corrected with Chase, (✖) measured data corrected with Corcos and (□) uncorrected measured data.

Figure 2.8 Comparison of one-point frequency spectrum predicted by empirical models with measured by [Farabee, 1986] as presented by [Hwang *et al.*, 2003]

2.5.2 Two-point wall-pressure spectrum models

Two-point wall-pressure spectrum models represent the spatial convective energy correlation, whereas the one-point wall-pressure spectrum represents the temporal energy distribution of the TBL WPF. In the comparison of various two-point models, normalised two-point coherence spectrum(spatial domain) or normalised wavenumber-frequency spectrum(wavenumber domain) are used. These spectra can be obtained by normalising the cross spectrum or wavenumber-frequency using one-point frequency spectrum. But incase of a prediction and validation of sound radiated due to TBL wall-presure excitation using empirical models, a full-pledged model would include the product of one-point spectrum and two-point spectrum. The basic idea in two-point wall-pressure model is to deduce an expression for wall-pressure function using curve fitting procedure based on the measurement of coherence with multiple probe spacings. Notable two-point spectrum models from an exhaustive literature review can be categorised into separable(eg:Corcos) and non-separable models (eg: Chase). Separable models like [Corcos, 1963] express the two-point wall-pressure in terms of separate streamwise and spanwise functions that makes it mathematically simple. Some of the examples of separable models are [Cockburn and Robertson, 1974], [Smol'yakov and Tkachenko, 1991] and [Efimtsov, 1982], Modified Corcos by [Hambric *et al.*, 2004] and a recent Generalized Corcos model by [Caiazzo *et al.*, 2016]. The non-separable two-point models are [Williams, 1982], [Witting, 1986], [Chase, 1987], [Mellen, 1990], combined Chase by [Hwang *et al.*, 2003] and modified Chase by [Finnveden *et al.*, 2005]. Both separable and non-separable two-point models also have their one-point spectral model counterparts except Corcos model that has to use any one-point model discussed earlier. In the following section a short description about each model and its limitations are discussed.

Corcos model

One of the first empirical models for WPFs was introduced by [Corcos, 1963]. This model was developed based on the experimental curve fitting for the measured coherence spectrum of WPF's in terms of spanwise and streamwise exponential decaying functions separately. It is based on the hypothesis of one-parameter similarity. The cross spectral density of the pressure is the product of three functions: the autospectrum of the point pressure fluctuations and two exponential functions, to account for the pressure correlation in the stream wise and spanwise directions. The general form of Corcos model for wall-pressure fluctuations is given by

$$G_p\left(r_x, r_y, \omega\right) = S_{pp}\left(\omega\right)\psi\left(r_x, r_y, \omega\right) \tag{2.22}$$

where cross spectral density $G_p\left(r_x, r_y, \omega\right)$ consists of a power spectrum $S_{pp}\left(\omega\right)$ and a

coherence $\psi\left(r_x, r_y, \omega\right)$ and Corcos model for cross spectral density is given by

$$G_p(x, y, x', y', \omega) = S_{pp}(\omega) e^{-\left|\frac{\omega r_x}{\alpha_x U_c}\right|} e^{-\left|\frac{\omega r_y}{\alpha_y U_c}\right|} e^{\frac{i\omega r_x}{\alpha_x U_c}} \tag{2.23}$$

Where (x, y) are coordinates of measurment point on the plate and (x', y') are the reference point on the plate, probe separations $r_x = x - x'$ and $r_y = y - y'$, U_c is the convection velocity, $1/\alpha_x$ and $1/\alpha_y$ are the decay constants given by the empirical model.

The Corcos model gives good estimate of the cross spectrum of the pressures near the convective region and it has questionable validity in the sub-convective region. The Corcos model overestimates dramatically the low wave number levels for the spectrum which exhibits a white wave number spectrum 20 to 40 dB above the measured spectrum in the sub-convective region down to the acoustic domain.The advantage of Corcos model is that it is simple enough to provide closed form analytical expressions for the modal excitation term either in space-frequency domain or in wavenumber domain. Due to the convertibility nature from spatial domain to wavenumber domain, the Corcos model can easily be handled for parametric studies over the entire frequency range and reduces the computational effort.

Cockburn and Roberston model

In an investigation of the vibration response of the spacecraft shrouds to in-flight fluctuating pressures,[Cockburn and Robertson, 1974] utilised a semi-empirical equation for the wall-pressure frequency spectrum beneath a homogenous and attached boundary layer at transonic and supersonic speeds. This model represents the frequency distribution of the mean square pressure as a function of the characteristic frequency, which is function of outer variables like Corcos. Cockburn and Robertson model was intended for vehicles at transonic and supersonic speeds and it may not be applicable for the low speed ground or marine vehicles.

Chase model

This is the first model after Corcos which describes the wall pressure in terms of wavenumber-frequency spectrum for incompressible inviscid flow that follows the Kraichnan-Phillips low wave number constraints. Modelling of sub-convective region was included by [Chase, 1980] and it was the first model to include the spatial characteristics of boundary-layer structure while including details of the turbulence structure. This model includes both mean shear and turbulence-turbulence pressure spectra that is dependent upon eight empirical coefficients that control the shape and level of the pressure spectra. In this model, the low

wavenumber spectrum is proportional to the square of the wavenumber and vanishes at zero wavenumber. In the following paper [Chase, 1987], Chase re-examined the character of the wavenumber-frequency spectrum and modified the spectrum to be wavenumber independent (or white) and consistent with the experimental data in sub-convective domain. [Chase, 1987] model was extended to acoustic domain with the inclusion of fluid compressibility such that acoustic components are generated by the incompressible source terms, Reynolds stress field. This model was widely used and summarised in [Howe, 1987] with slight modifications.

In a modelling perspective, the [Chase, 1987] model is a hydroacoustically sensible model based on the real world experience in hydroacoustics and is consistent with the Kraichnan-Philips theorem. The Corcos model on the other hand was not focussed on the secondary hydrodynamic effect and may be considered as hydroacoustically blind model. In summary, the Chase and Corcos models are complimentary. On one hand the Corcos spectrum provides good estimates of wall pressures near the convective region which is of fundamental importance for aircraft boundary layers. On other hand the Chase spectrum is more suitable for low speed flow applications where the strong flow-structure interaction occurs in the low wave number region (sub-convective region).

Efimtsov model

[Efimtsov, 1982] follows Corcos philosophy, but takes into account the dependence of the spatial correlation on the boundary layer thickness, as well as spatial separation. Although this model represents an improvement on that of Corcos, it suffers from the same tendency to overpredict the spectrum at low wave numbers.

Ffowcs Williams model

[Williams, 1982] derived an expression for wavenumber-frequency from Lighthill's analogy and assuming the velocity source terms were of the general Corcos form containing several unknown constants and functions to be determined experimentally.

Witting model

The postulated sources of pressure fluctuations in [Witting, 1986] model were hydrodynamic dipoles distributed in the wall boundary layer region, along with their mirror images about the plane of the wall, which establish impenetrable conditions. This model is given in wavenumber-white spectrum which is a function of the mean-square wall pressure and three parameters: C, free empirical constant which is the measure of the life-time of the sweep/ejections, limits of integration above and below which it is assumed that the contributions of the sweeps and ejections are negligible. Since the model depends on the

mean-square pressure, the overall level of the model spectra is Reynolds number dependent. Witting's formulation was criticized as artificially introducing a volume dipole which is incompatible with the incompressible Lighthill's equations.

Smolyakov and Tkachenko & Smolyakov model

[Smol'yakov and Tkachenko, 1991] have proposed a generalized model of Corcos keeping in view of its inadequacy in low wave numbers. The model includes frequency dependent generalized decay rates in conjunction with a non-rectangular product of the coherence functions. The coherence functions is an exponential function of the square root of the geometric sum of streamwise and spanwise directions. It also includes a correction factor to bring the low wavenumber spectra to the measured data. It is expressed in terms of both inner and outer variables.[Smol'yakov, 2000] developed a simple model for wall pressure based on the source mechanisms that generate wavenumber spectrum caused by the interactions between turbulence and the mean shear. This model is also convertible from wavenumber-frequency to spatial domain. From the generalised wavenumber-frequency source function and the mean shear terms, the point frequency spectrum is evaluated. He argued for the requirement of different scaling for different frequencies and Reynolds numbers.

Combined Chase model

Combined chase model is developed by combining the [Chase, 1987] inviscid flow model with semi-empirical shear stress model of [Chase, 1993], it attempts to overcome the over prediction of low-wavenumbers noticed in Corcos model by including the merits of Chase models. A comprehensive review on the comparison of empirical models for predicting the noise generated due to TBL was given by [Graham, 1997], [Borisyuk and Grinchenko, 1997], [Hwang *et al.*, 2003] and [Miller *et al.*, 2012]. The comparison of empirical models is given in Figure 2.9. But none of the empirical models could predict accurately the low-wavenumber and acoustic components of TBL wall-pressure excitation which is very crucial to have an accurate vibro-acoustics response. Hence a CFD simulation might be a possible way to estimate both acoustic and convective zones of TBL WPF which would be discussed in 2.6.

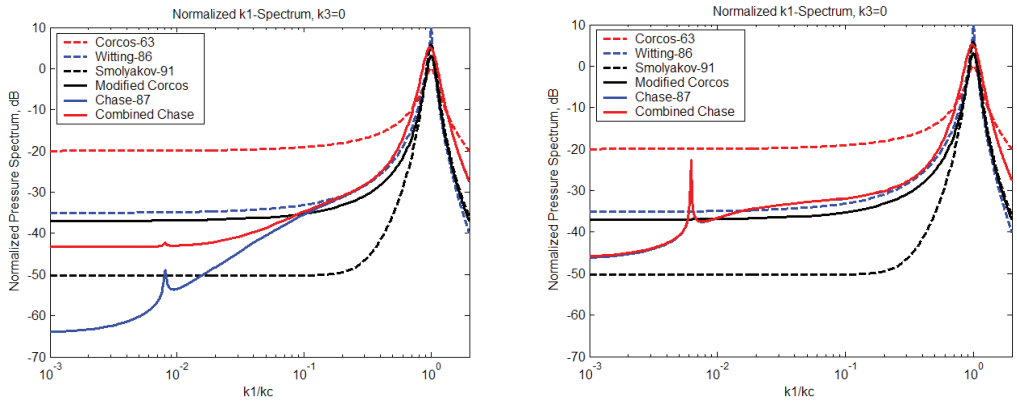

Figure 2.9 Comparison of WPF with empirical models at fixed frequency [Hwang *et al.*, 2003]

2.6 Numerical models for TBL wall-pressure fluctuations

The empirical models in Section 2.5 have a limited applicability for solving the real world flow induced noise problems as these models are based on assumption that WPF are homogenous and stationary over a smooth flat plate with zero pressure gradient, except models like [Rozenberg *et al.*, 2012] that extends the [Goody, 2004] model to accommodate the effects of adverse pressure gradients. It is well known that to accurately resolve the small scale structures of a TBL, the size of the transducer must be as small as smallest turbulent structure [Abraham and Keith, 1998]. The cost of wind tunnel tests for determining the WPF for each application and geometry makes the experiments prohibitive. With the development of super computers, the numerical simulation of turbulent flows can be possible which are complimentary to both the experiments and theories in the study of WPF's. The CFD numerical simulations of turbulent flows are an appealing cost effective way to serve as a remedy.

Most practical flows, such as flow over airplanes and ships, have a large Reynolds number (Re=$10^5 - 10^6$). Most wind tunnel and water tunnel flows have smaller Reynolds number (Re = $10^3 - 10^4$). Therefore, understanding the effects of Reynolds number is crucial when applying wind tunnel results to the analysis of practical flows [Goody, 2004]. Hence the optimal way is to develop a numerical model for WPF using computational fluid dynamics (CFD) tools. The CFD numerical simulations attempts to resolve the turbulent scales in the flow over the complicated geometries like side mirrors in automobile with little assumptions compared to empirical models. The computational fluid dynamics tools widely used for modelling the turbulent flow over a flat plate are LES, RANS and DNS.

2.6.1 Unsteady CFD Tools

Direct numerical simulation

Direct Numerical Simulation (DNS) is restricted to simple geometrical problems and low Reynolds number flows, i.e (Re = 10^2 - 10^3). Many investigators have made measurements at Reynolds numbers high enough such that the turbulent energy content is large with respect to the energy of the acoustic noise. As a result, there are very few measurements with low-Reynolds number for which DNS results can be compared. Specifically DNS studies provide information for validating models of quantities that are not easily measured experimentally, such as pressure-strain correlation. In addition the range of scales increases with increasing Reynolds number and in most instances the size of the small-structures decreases. High Reynolds number measurement of turbulent wall pressure fluctuations suffer from poor resolution [Gravante *et al.*, 1998] .

Direct numerical simulations and large eddy simulation were first used to obtain WPF's for low Reynolds number channel flows by [Choi and Moin, 1990] and [Chang III *et al.*, 1999]. The DNS database developed by Choi and Moin (1990) for low Reynolds number channel flow has been used by many other researchers for further studies and validation. They have predicted the wall pressure fluctuations using direct numerical simulations (DNS). They have computed the wavenumber-frequency spectra for a very moderate Reynolds number Re = 3200. However, at such Reynolds number, the low wavenumber zone and the convective zone are not separated enough to allow the determination of the different scaling behaviours reported by experiments and theoretical models. Their spectra agreed with other numerical results in the convective ridge region, but have higher levels at lower wavenumbers. As a result, extrapolation of such low Reynolds number simulation to much higher Reynolds number flows typical of hydrodynamic or aerospace is not possible.

Large eddy simulation

In contrast to DNS, Large Eddy Simulation (LES) computes the large scales directly and models the small scales or the subgrid scales, thereby yielding a cheaper alternative to DNS. The LES is not limited to low Reynolds numbers, since large energetic scales are computed while the universal fine scales are modelled without the necessity for fine grid like in DNS. Although the Reynolds number restriction and computational cost of LES is favourable compared to DNS, it is still not used for engineering design problems of interest due to its rather long turnaround time. Hence Very Large Eddy Simulation (VLES) is used instead of LES. The fundamental basis of VLES is almost the same as in LES, except a typical LES resolves 80 of the turbulent length scales and the other 20 is modelled. In VLES however, roughly half of the turbulent length scales are modelled and other half are

resolved. Thus the VLES methodology relaxes the computational cost to an even greater fraction when compared to LES and DNS due to its far lower grid resolution requirement. The numerical method based on Lattice Boltzmann method (LBM) combined with VLES turbulence model provides an accurate and efficient approach to high Reynolds number flow simulation [Crouse *et al.*, 2006a].

An unsteady incompressible Large Eddy Simulation (LES) based method has been successfully implemented by [Wang *et al.*, 2009] to predict the statistical properties of wall pressure on low speed airfoil with RANS computed boundary conditions to account for the effect of airfoil aerodynamic loading. The wall pressure spectra obtained from LES was in good agreement with the measured values from wind tunnel tests. The second order statistics like spanwise coherence of the wall pressure has reasonable match with experiments except at low frequency. Trailing edge broadband noise was calculated from the LES extracted acoustic source data using Ffowcs Williams and Hall solution based on half-plane Green's function. Similar incompressible LES approaches have been adopted by [Winkler *et al.*, 2009] to predict the broadband noise of airfoil with and without trailing edge blowing. Trailing edge blowing helps to mitigate the noise radiation by addition of fluid to improve mixing process. Amiet's trailing edge noise theory was used to predict the aeroacoustic noise from airfoil and the mechanism of noise reduction with blowing technique has been studied.

For high Mach number flows above 0.3, the CFD computation has to be treated as compressible due to the density changes and the need to resolve the low amplitude acoustic pressures for aeroacoustics simulation. Recently [Gloerfelt and Berland, 2013] have studied the turbulent boundary layer noise generated over flat plate at Mach number 0.5 using unsteady compressible LES method. A small step was introduced in the spanwise direction to create the turbulence at the leading the edge of flat plate. LES computation with finite difference scheme and selective filtering without any eddy viscostiy model was used for prediction of the wall pressure fluctuations on the flat plate. Spatio-temporal characteristics of wall pressure like mean, coherence and wavenumber frequency spectrum are calculated from the simulated wall pressure data and match well with experiments. Direct numerical computation was used to calculate the acoustic radiation and directivity patterns of the turbulent noise sources . The acoustic domain and convective domain in the wavenumber frequency spectrum are noticed clearly but they are inseparable due to the high speed flow and the low amplitude of the acoustic components. Quantifying the acoustic contribution(low wavenumber) to the radiated noise from wavenumber frequency spectrum analysis is very challenging task.

[Senthooran *et al.*, 2006] have compared the experimental and simulated wall pressure fluctuations on the side glass of a full scale production automobile for different flow conditions. The CFD simulation was carried out in PowerFLOW, based on Lattice Boltzmann Method (LBM), combined with RNG turbulence model. Flow around the full vehicle was simulated at 0 and 10 degrees yaw and wind noise sources was predicted using spectral analysis on the simulation data and the results are compared with the microphone data during the wind tunnel testing. The results match well with experiment up to a high frequency cut-off around 2000 Hz, which is dependent on the grid resolution. This work demonstrates the capabilities of LBM in the prediction of wall-pressure fluctuations for a subsonic external flow around an automobile.

2.6.2 Statistical and Stochastic models based on steady RANS

Statistical models

In the research study of wall pressure fluctuations beneath turbulent boundary layers, there exists numerous approaches in literature to estimate wall-pressure and those practiced in industry. Although there is no single optimal approach that predicts the wall-pressure accurately and the approach selected might vary with kind of application at hand and the accuracy needed. In a broad sense, these approaches can be categorised into classical analytical, empirical and semi-empirical models derived from experiments, stochastic and statistical models based on RANS, LES or DNS and wind tunnel experiments. The classical analytical approach mostly involve solving the Poisson equation for fluctuating pressure using mathematical simplification or numerical approach. It is limited to low Mach number turbulent flows with self-similar velocity profiles. As analytical approaches have their limitations, empirical and semi-empirical methods are considered as a better choice to estimate wall pressure due to their inclusion of the physical phenomena using turbulent boundary layer parameters as discussed in Section 2.3.3. Stochastic models rely on synthetic turbulence generated from mean flow inputs and turbulence parameters obtained from a time and cost-effective steady RANS calculations, whereas statistical models rely on curve fitting procedures and turbulent boundary layer parameters obtained from RANS for the prediction of wall-pressure prediction. Stochastic approaches like Stochastic Noise Generation and Radiation (SNGR) and Random Particle Method (RPM) take advantage of the mean flow results from RANS simulations to reconstruct the turbulent wall-pressure fluctuations with help of synthetic or artificial turbulence to reduce the CFD computational effort involved in resolving the turbulent fluctuations.

In the early 1950's [Kraichnan, 1956] deduced an analytical relation for mean wall pressure statistics in terms of the velocity fluctuations namely mean velocity profile and two point

quadratic velocity correlation perpendicular to the boundary surface. He had deduced a theoretical expression for wall pressure and velocity fluctuations on a rigid flat plate incompressible turbulent flow based on integration of Poisson's equation. The Poisson equation is as follows

$$\partial^2 p/\partial {x_i}^2 = -\rho\, \partial^2(u_i u_j)/\partial x_i \partial x_j \tag{2.24}$$

The basic concept in this analytical relation is that wall pressure acting on the surface of the flat plate is given by the summation of the various turbulent velocity fluctuations over the boundary layer wall normal coordinate and represented mathematically by Kraichnan integral. Two kinds of interactions are observed in the Poisson equations corresponding to turbulent velocity fluctuations, the first one is turbulence-mean shear interactions which are linear and turbulence-turbulence interactions that are quadratic. Turbulence-mean shear interactions are dominant compared to the turbulence-turbulence interactions due to their linear nature. The final outcome was to estimate the root mean square(rms) value of the pressure fluctuations using the triple integral of pressure over the volume with turbulent source terms or five-fold integral when Fourier transformed. The mathematical details of the triple and five-fold integrals are presented by [Panton and Linebarger, 1974] as shown below

$$\phi(k_1) = 4\rho^2 \int_{-\infty}^{\infty}\int_{-\infty}^{\infty}\int_{-\infty}^{\infty} \frac{k_1^2}{k^2} exp(-k(x_2 + x_2')S_{22}(k_1, x_2, x_2', k_3)\frac{dU_2}{dx_2}(x_2))\frac{dU_2}{dx_2}(x_2'))\, dx_2 dx_2' dk_3 \tag{2.25}$$

where $k = k_1^2 + k_3^2$, $\phi(k_1)$ is the wavenumber spectral density and $S_{22}(k_1, x_2, x_2', k_3)$ is Fourier transform of the velocity correlation coefficient

$$R_{22}(r_1, x_2, x_2', r_3) \equiv \overline{u_2(x_1, x_2, x_3)u_2(x_1 + r_1, x_2', x_3 + r_3)}/(\hat{u_2}(x_2)\hat{u_2}(x_2'))$$

$$S_{22}(k_1, x_2, x_2', k_3) = \frac{u_2(x_2)\hat{u}_2(x_2')}{4\pi^2}\int_{-\infty}^{\infty}\int_{-\infty}^{\infty} R_{22}(r_1, x_2, x_2', r_3) exp[-i(k_1 r_1 + k_3 r_3)]\, dr_3 dr_1 \tag{2.26}$$

where $\hat{u}_2 \equiv \sqrt{\bar{u_2^2}}$ is the turbulent intensity component. The triple integral in Equation 2.25 for wavenumber spectral density is transformed into a five-fold integral by incorporating

the double integral relation in Equation 2.26. The turbulence quantifying parameters required for evaluation of this five-fold integral are the mean shear profile $\frac{dU_1}{dx_2}$, the turbulent intensity field $u_2'(x_2)$ and normal velocity correlation coefficient R_{22}. The Kraichnan's analytical relation in Equation 2.25 and Equation 2.26 forms the basis for statistical models like [Remmler *et al.*, 2010] and [Rozenberg and Roger, 2010]. [Panton and Linebarger, 1974] implemented the analytical work of [Kraichnan, 1956] to estimate the wall pressure beneath equilibrium boundary layers using numerical techniques. The mean velocity profile was assumed to follow the law of wall and Cole's wake function to estimate the wall pressure spectrum. He has used the Monte Carlo method to numerically integrate the five-fold integral of fourier transformed pressure instead of mathematical approximations. He has studied the effects of various parameters like Reynolds number, anisotropy and turbulence scales on the wall pressure spectra under different pressure gradients. The computed wave number frequency spectra have good agreement with experiments conducted by [Bradshaw, 1967] except at high frequencies. Both [Kraichnan, 1956] and [Panton and Linebarger, 1974] approaches involve analytical methods to estimate the wall pressure fluctuations for simple flat plate boundary layers flow with mild pressure gradients with many mathematical and physical assumptions. For an industrial case of flow induced noise, these above mentioned classical approaches fall short in its accuracy and replication of the real physics of the problem. Hence a widely used time-efficient and cost-effective RANS approach is used to compute the steady flow field (mean component of turbulence fluctuations).

[Glegg *et al.*, 2010] has adopted a different kind of statistical approach to determine the space-time velocity correlation and wavenumber spectra from the steady RANS calculations which is based on vortex sheet strength spatial distribution of turbulent kinetic energy and its relation to turbulence spectrum and mean flow velocity distribution. Recently [Lee *et al.*, 2005] have tried to determine the wall- pressure spectrum for equilibrium flows with zero pressure gradient using spectral correlation model. The spectral model is obtained from Green's function formulation and modeling of the spanwise and streamwise wavenumber spectra. [Lee *et al.*, 2009] later adapted spectral modeling to non-equilibrium flows like Backward facing step(BFS). In similar direction, [Peltier and Hambric, 2007] used a RANS based surface-pressure space-time covariance model with closure from flow specific assumptions to estimate the wall pressure spectra. The covariance model needs much more validation for stronger adverse and favorable pressure gradients at different Reynolds numbers and more three dimensional realistic cases. Unlike the earlier BFS test cases, [Remmler *et al.*, 2010] has calculated the airfoil trailing-edge noise from the wall pressure estimated from RANS based statistical model. [Rozenberg *et al.*, 2012] extended the

Goody's empirical model to include the adverse pressure gradient effects in the prediction of wall-pressure spectrum. His model is based on the mean steady flow inputs from a RANS simulation. [Albarracin *et al.*, 2012] combines the statistical model for velocity fluctuations and steady RANS simulations to predict the trailing edge noise for NACA airfoils. The far field acoustics was estimated using half-plane Green's function formulation. Although statistical models when combined RANS give good results of wall-pressure spectra for certain cases, they need to vigorously tested for a wide variety of case studies and different flow parameters. [Juvé *et al.*, 2015] discusses in detail on the limitation of empirical and statistical models in the estimation of wall-pressure spectra compared with unsteady CFD numerical approaches. There is a lack of consensus among of researchers on the use of RANS based statistical models compared to unsteady LES based approaches especially for aeroacoustic applications.

Stochastic Models

Another class of wall-pressure modeling approaches used in automotive industry to predict the flow induced noise are the stochastic methods like SNGR (Stochastic Noise Generation and Radiation). SNGR depends on the steady state RANS calculations. These methods were first developed by [Kraichnan, 1970] to study the particle diffusion by random velocity fields in incompressible turbulence and extended by [Bechara *et al.*, 1994] for free turbulent flows. In this method, turbulent velocity fluctuations wall-pressure fluctuations also termed "synthetic turbulence" are reconstructed using stochastic approaches from steady RANS calculations. SNGR makes use of the steady RANS calculations to obtain the time-averaged statistics like turbulent kinetic energy, integral length scales and time scales, Reynolds stresses, spatio-temporal statistics of turbulent flow. Stochastic methods are mainly categorized as Fourier based methods and digital filter based methods. Stochastic methods have been also used to generate inflow or inlet turbulence for LES simulations. In Fourier modes approach a finite summation of Fourier modes with random amplitudes and phases are used to generated over the mean statistical quantities of turbulence calculated from RANS simulations [Bechara *et al.*, 1994]. Fourier modes approach has two major limitations, it is computationally intensive due to the large number of modes required to meet the target the statistical turbulence values and its inability to generate inhomogeneous turbulence due to the inherent use of Fourier modes. Hence the filter based methods that make use of digital filter are computationally efficient to generate the target value of turbulence quantities. Random particle methods (RPM) proposed by [Ewert *et al.*, 2011] and [Ewert, 2007] fall under the category of digital filter based methods. In this method the stochastic turbulent velocity field is denoted by stream function generated from appropriate filtering

of white noise and the transient state of convection is denoted by Langevin's equation. Other such methods are [Klein *et al.*, 2003] and [Careta *et al.*, 1993]. In RPM, once it is discretised, it can be interpreted as a collection of random vortex particles. RPM has an advantage that it is able to generate wide variety of inhomogeneous, anisotropic turbulence flows and its statistics such as turbulent kinetic energy and its second-order time and spatial statistics. RPM method by its nature generates divergence free (solenoidal) in an affordable computational cost compared to random fourier modes approach. Fast Random Particle method (FRPM) and Random Particle Method(RPM) are two different kinds of numerical implementation of the Stochastic particle model developed by [Ewert *et al.*, 2011]. Spatio-temporal correlations are generated in case of RPM method in contrast to wavenumber-frequency spectrum like fourier modes approach. RPM method can take into account the source convection speed implicitly as it is a correlation based model in time domain. RPM has been used to predict airframe noise, trailing edge noise, slat noise and jet noise. SNGR is better suited in the iterative design of aero-acoustic components and for prototype comparison purpose during development. [Védy *et al.*, 2005] have applied SNGR technique coupled with LEE Solver to predict the A-pillar vortex and side mirror noise and validated with side mirror experiments conducted by PSA Groupe. [Siefert *et al.*, 2010] has used RPM method to obtain the spatial and temporal wall-pressure fluctuations for a flat panel cavity and predict the turbulent boundary layer noise inside the cavity. Assuming a turbulent pressure field that follows Poisson's equation, turbulent velocity and pressure fields are synthesized with averaged parameters like convection velocity, amplitude and spatial temporal characteristics that are deduced from RANS simulations. The synthesized pressure field correlations , kinectic energy and velocity profiles are validated with those obtained from solving Poisson's equation. Once the stochastic RPM model has been validated, it is adapted to use RANS averaged quantities as inputs. Structural acoustic response to the wall-pressure fluctuations has been calculated using Finite Element (FE) approach in ANSYS software. The synthesized wall-pressure fluctuations from stochastic RPM model are mapped onto a structural FE mesh and act as a distributed correlated excitation. The wall pressure excitation gets coupled with the structural modes of panel to radiate sound into the cavity. Finally panel response and acoustic sound power levels inside the cavity were estimated due to the turbulent wall pressure excitation.

2.7 Measurement of TBL wall pressure fluctuations

Measurement challenges

Empirical models of the wavevector-frequency spectrum rely on experimental data to establish values for dimensionless coefficients developed in the theory. Due to the requirement of sophisticated sensor (MEMS) and signal processing technology, the accurate measurement of boundary layer wall pressure fluctuations had proved difficult. The measurement of low frequency components of the TBL were often masked by the noise of the measurement facility. And also due to the large size of the pressure transducers employed, the high frequency components were subject to attenuation due to area averaging over the face of the transducer. In other words, the measurement of the low wave number region of the TBL wall pressure spectrum may be characterised essentially as the measurement of a relatively low amplitude signal in the presence of much higher amplitude signals. The various measurement techniques for low wavenumber frequency spectrum are given by [Pope, 1979]. A detailed mathematical description of turbulence wall-pressure fluctuations and flow-induced noise-source generation are given in a text book by [Blake, 2017] in Chapter 8.

Measurements techniques

The measurement techniques for wave number-frequency spectrum can be categorised as

- Two-point measurements
- Direct measurement of wave number-frequency spectrum by spatial discrete Fourier transformation of cross power spectral density
- Wave vector filtering: use of array of pressure transducers (linear combination of measurement of signals with known distances between the transducers).
- Measurement with thin membrane or structure as a wavenumber filter

Two-point measurements

[Wills, 1971] measured two-point wall-pressure cross spectra and then used a spatial Fourier transform to obtain an estimate of the wavenumber-frequency spectrum. Both streamwise and spanwise spectra were presented. Will's estimate of the wavenumber-frequency spectrum was limited to the region in the wavenumber near the convective ridge. Two-point measurements have been used to infer the wavenumber-frequency characteristics of the wall pressure from cross spectrum. They often lack the spatial resolution needed to resolve the wavenumber-frequency spectrum. The limitations were primarily due to the phase matching of the electronics and acoustic contamination in the test section.

[Keith *et al.*, 1992] discussed that the pressure sensors should be sufficiently small to resolve the turbulent scales of the order of ten viscous lengths and should be calibrated to establish their wave number-frequency response. They suggested noise cancellation techniques to reduce the back ground noise. [Schewe, 1983] studied the effect of spatial averaging on the wall pressure measurements such as spectra, RMS level and the probability density function. Schewe suggested that the largest allowable value of the non-dimensional sensing diameter of the transducer that can resolve the significant turbulent scales of motion was $d^+ = \frac{du_t}{\nu} = 19$, where d is the sensor diameter, "+" subscript denotes scaling with kinematic viscosity of fluid ν and shear velocity u_t. This decision was made from the extrapolation of data from the smallest sensor (d^+ =19) to the infinitesimally small transducer (d^+ =0) rather than measurements. He suggested that the measurement of the wavenumber-frequency spectrum of turbulent wall pressure fluctuations requires a line of array of closely spaced sensors. [Lueptow, 1995] has found the size and shape of the transducer resolution for measurement of wave number frequency spectrum at high frequencies through a numerical application of wave-number filters. The highest measured frequency is given by $\frac{\omega_{max} d}{U_c} = C$, where C is 2π, 7.7 and 11 for square piston, circular piston and circular deflection microphones respectively, d is the diameter of the circular piston and d is replaced by L the size of square piston. U_c is the convection velocity. However, the wide range of wave numbers of the wall pressure fluctuations that contribute to the spectrum imposes constraints on sensor size, spacing and number.

Direct measurement: Spatial Fourier transform of CPSD

The direct measurement of the wavenumber-frequency spectrum has proved to be an extreme difficult task. This method requires a low-pass wave number filtering and large number of sensors based on Shannon sampling theorem. [Abraham and Keith, 1998] used the direct measurement method. [Manoha, 1996] performed the direct measurement of the wavenumber-frequency spectrum of wall pressure over a cylindrical body using 32 transducers in air. Their measurements were limited at low wavenumber by background facility noise. [Arguillat *et al.*, 2010, 2005] measured the pressure fluctuations in case of flow over a flat plate. She measured the pressures over a surface instead of a line so that two dimensional wave number frequency spectra can be calculated. Remote microphone probes were used for measurement. The measurement arrays consists of 63 remote microphone probes placed along the diameter of a rotating disk to measure the pressure at each time step. The cross power spectral density (CPSD) is obtained from the Fourier transform of the temporal and spatial wall pressure functions using Weiner-Khinchin relations (Hanning window). Then the spatial Fourier transformation of the CPSD was done to obtain the

wavenumber-frequency spectrum (rectangular window). Post processing was developed to transform the two dimensional space-frequency data into wave number-frequency spectra. The direct measurements method will also yield the same estimate of the wavenumber-frequency spectrum as that from transforming two-point cross-spectrum measurements. However, the direct method has advantages in that sensors do not need to be moved and any alignment errors are essentially constant. [Salze *et al.*, 2015] have improved experimental setup to measure wall-pressure data under pressure gradients using linear antenna of microphones. Direct measurement of wavenumber-frequency spectra are conducted with rotating linear antenna of microphones with various probe spacing. The investigation of the acoustic component of the wall-pressure is not fully done and needs further study.

Wavevector filter: array of pressure sensors

[Maidanik and Jorgensen, 1967] designed the wavenumber filter that will admit data in low wavenumber region and yet reject both sonic and convective components. The array consists of linear streamwise rows of uniformly spaced and identical pressure transducers. With this array, it is possible to filter out unwanted wavenumber components of the wall pressure spectrum. The two types of arrays published in literature are the common-phased array (low pass spatial filter) and alternate-phased array (band pass spatial filter). This type of arrays is termed as wavevector filters by [Maidanik and Jorgensen, 1967]. Using this wavevector filters a white wavenumber spectrum in the sub-convective range was observed. For the case of turbulent boundary layers at moderate to high Reynolds numbers, the wavenumber filter design requires micro fabrication technology. The signal processing chart for wavevector filtering is shown in Figure 2.10.

2.8 Vibroacoustic analysis due to TBL Excitation

2.8.1 Approximate analytical methods

When the turbulent WPF are known in space-time, space-frequency and wavenumber-frequency domain then the problem becomes a classical example of random excitation. Typical examples of this type of excitation are, plate-cavity system excited by TBL, structure excited by diffuse acoustic field and rain-on-roof excitation (spatially uncorrelated). [Strawderman and Brand, 1969] have developed an analytical solution for the response of a simply supported rectangular panel excited by turbulent boundary layer. They have neglected the radiated acoustic pressure considering the TBL excitation only. Corcos model was used to model the wall pressure fluctuations on the plate to obtain the excitation auto and cross spectrum. The convection velocity was assumed to be constant. Finally the plate vibration velocity was calculated in spatial domain and validated with wind-tunnel

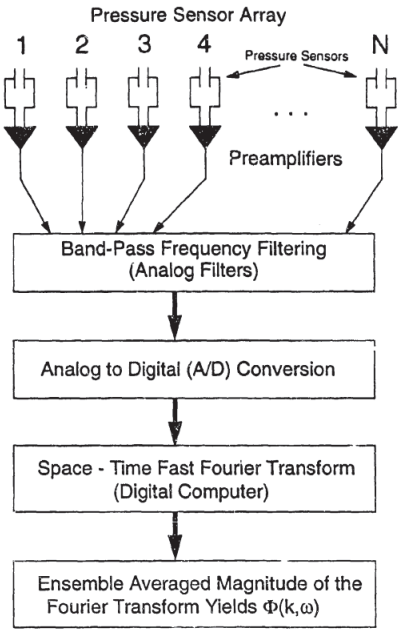

Figure 2.10 Signal processing chart for wavevector filtering [Keith and Abraham, 1994]

measurements. Further analytical studies on flow induced response was done by [Davies, 1971] using space integration in frequency-space, modal summation by [Robert, 1984], wavenumber-frequency integration by [Mazzoni, 2003] and [Maury *et al.*, 2002]. Analytical methods were used for flow induced response like Rayleigh-Ritz by [Park *et al.*, 2004].

[Park *et al.*, 2004] investigated the effect of seal mechanical and geometries on the sound and vibration response of a plate-cavity system. In an open-circuit wind tunnel (speed 50 m/s) with uniform and corrugated fence, reattached flow and separated/reattached flow was generated over the plate backed by anechoic cavity as shown in Figure 1.4. The plate size was similar to that of the side glass of a car window. The two types of fences were used in creating turbulent wall-pressure field on the plate. The other noises are such as wind tunnel noise and sound radiation from flanking are minimised. The wall pressure spectra of reattached flow, equilibrium flow and separated/reattached flow was rich in low frequency content. There is a 30 dB increase in amplitude of wall pressure spectrum of reattached and separated/reattached flow when compared to the equilibrium flow. Corcos model was used for finding the wavenumber-frequency spectrum of TBL with decay rates determined from curve fitting of measured coherence data. Rayleigh-Ritz method was used to find the vibration response of the plate (with seals modelled as springs) for the turbulent flow excitation. This study will be re-examined in this thesis using a direct PowerFLOW code based numerical algorithm for the WPF excitation.

2.8.2 Modal based element methods: FEM and BEM

Prediction of flow induced vibration and sound can be studied in spatial or wavenumber domain. In case of spatial domain the turbulent wall pressure excitation is defined in terms of auto and cross spectral density. The spatial Fourier transform of cross spectral density gives the wavenumber frequency description of the wall pressure excitation. Figure 2.11 describes the various domains in which the response is calculated. A classical reference book that describes in detail about the structural response and its sound radiation due to the TBL excitation is [Blake, 2017]. Usually element based methods make use of normal mode superposition or modal summation approach to achieve faster computation of response compared to the full frequency solver approach.

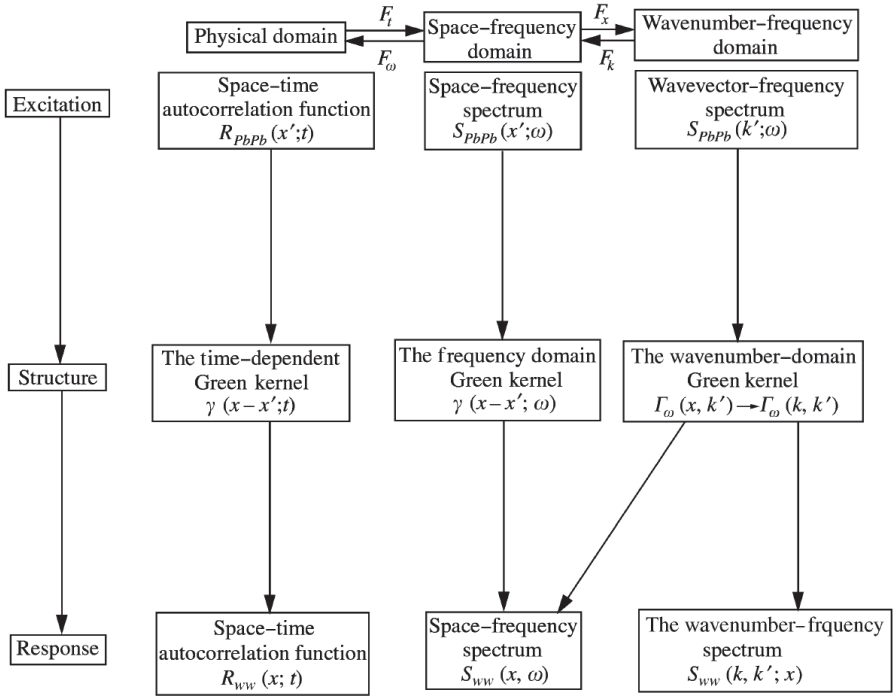

Figure 2.11 Various domains in response calculation [Maury *et al.*, 2002]

Finite element method by [Allen and Vlahopoulos, 2001] predicted the noise generated from a plate excited by TBL considering a plate-cavity system for flow induced noise analysis. The WPF are determined from [Smol'yakov and Tkachenko, 1991] model. The structural with seals are modelled in FE to find the vibration response due to the WPF and the sound radiated into the cavity is calculated using BEM. But it sufferred high frequency resolution problem.

[Han *et al.*, 1999] have used EFEM to account for the non-uniform, distributed excitations while taking aerodynamic flow/structural coupling. The power input was calculated using plate mechanical impedance and empirical models. Two flows were considered separated

and reattached and turbulent flows. The [Smol'yakov and Tkachenko, 1991] wave number-frequency model was used to estimate the fluctuating pressure underneath turbulent boundary layer. The Corcos model was used to estimate the wall-pressure field under non-uniform, separated reattached flows. Chase model and the Smol'yakov and Tkachenko model were found in best agreement with experimental data for cases where the outer Mach number is low and the structures are relatively stiff. These models are used at high frequencies, when the structural vibration response is dominated by resonant modes lying in the low wave number region of the wave number spectrum. Corcos model for the same conditions, over-predicted the structural response and the radiated sound power.

[Finnveden *et al.*, 2005] investigated the vibration response of plate excited by TBL using SFEM and validated with measurements. Corcos and Chase WPF models are compared with measured cross spectrum. Most of the turbulent energy is indeed around the convective region, but these are not important for the response of the structures at frequencies above aerodynamic coincidence. The largest structural response has a characteristic length greater than the boundary layer thickness, under this condition the faster, low wave number or sub-convective components are largely responsible for structural excitation, despite the fact that they contribute very little to the wall pressure. Experiments were conducted in close circuit wind tunnel (120 m/s) to generate turbulent flow over a clamped aluminium plate. The parameters in Corcos model were made frequency and flow dependent to improve the WPF. In Chase model, two parameters were introduced to better fit the spanwise coherence to measurements. Vibration response with both models agrees in the low frequency region with error of 3 dB and above aerodynamic coincidence frequency only modified Chase model was correct. Their experiment shows the superiority of Chase models over Corcos models for predicting the vibration response above aerodynamic coincidence.

[Mazzoni, 2003] calculated the vibro-acoustic response of a turbulent boundary layer excited panel and compared the random model with deterministic models. In case of low Mach number turbulent flow, he confirms that the sub-convective region of the turbulent excitation power spectrum contributes significantly to the response of the panel.

[Caro *et al.*, 2006] have investigated the noise due to the flow over a simplified side mirror fixed to plate backed cavity. An incompressible unsteady CFD simulation was done using FLUENT code to compute the pressure fluctuations instead of the empirical models due to the limitations of models. The acoustic simulations were performed in FFT Actran FE code which has an inbuilt Corcos and Goody models for TBL pressure fluctuations. The simulations were validated with plate backed cavity system. The plate backed cavity has been validated for mechanical and acoustical excitation to take care of the vibro-acoustic

part of the problem. The mean square velocity of the plate calculated using Corcos model and CFD does not match well but the predicted acoustic pressure in the cavity match well with the measured data. This strange result is because only a part of vibrating energy of the plate is transformed into acoustic radiation, the rest of the vibration energy does not radiate. The CFD simulations can include the effect of side mirror and higher order modes when compared to Corcos model. The modal approach of Corcos model takes less computation time and works well.

[Ragnarsson *et al.*, 2007] have found the vibro-acoustic response of the plate backed by cavity excited by a reattaching turbulent boundary layer using FEM/BEM software along with Corcos model and CFD software. They have calculated the turbulent wall-pressure fluctuations using two methods namely deterministic approach (CFD) and random approach using Corcos models. In deterministic approach the turbulent WPF were determined from PowerFLOW and interpolated to the fit the coarse acoustic mesh. The vibro-acoustic response of the cavity was calculated using random vibro-acoustic module of LMS Virtual Lab. In the random approach the power spectral density of the WPF determined from Corcos Model was decomposed into orthogonal deterministic load cases using singular value decomposition. Then the response is calculated for each deterministic case and the complete solution is obtained by combining the result of each load case. The plate surface velocity obtained from random approach and deterministic model were compared with the measurements from the Purdue cavity. The random and deterministic approaches overpredict the measurements due to the overprediction of the PSD in CFD and Corcos model. But the agreement between the random and deterministic approach is quite good.

2.8.3 Band averaged energy based methods: SEA

[Totaro and Guyader, 2003] used the Frequency Averaged Input Power (FAIP) model to find the response of a simply supported plate excited by TBL. Turbulent WPF (blocked pressures) are modelled in terms of wavenumber-frequency spectrum using Corcos and Efimtsov models and frequency averaged power input was calculated. Validations were done with modal summation method. The characteristic function was evaluated first to find the power input. Power input was calculated with Corcos model with coefficients given by [Robert, 1984]. [Davies, 1971] approximation was used to find the lower frequency limit for its applicability by comparing with modal summation results. FAIP model neglected the radiation damping and it is independent of the loss factor of the plate. The maximum of 3 dB variation is observed in one third octave band. The FAIP results are independent of the WPF model used. [Blake, 1970] power input model, gives 10 dB over estimates

when compared to FAIP model results below aerodynamic coincidence. FAIP model based on Efimtsov gives good approximation for whole frequency range.

[Bremner and Wilby, 2002] describes a SEA/CFD combined approach for solving the wind noise in automobiles. They have combined the wind tunnel and CFD tests to define empirical models for aerodynamic noise sources. Using SEA along with the CFD to provide a most cost-effective and integrated design solution for wind noise problems in automobiles. Similar SEA based method are discussed by [Dejong *et al.*, 2001] and [Strumolo, 2002].

2.8.4 Random sampling methods

Random sampling is widely used in solving the stochastic structural dynamics problems,whenever the traditional element based determintic methods fail to adapt the random nature of excitation and response. Due to the random nature of the turbulent boundary layer wall-pressure excitation, random sampling could be used to as an alternative to deterministic approaches. The motivation for our present work is to circumvent the traditional full-fledged CFD-FE simulation of TBL excitaion by utilising random sampling based on Corcos and CFD derived cross-spectral density matrix. In the recent literature [Coyette *et al.*, 2009; Hekmati *et al.*, 2010, 2013] have used random sampling to decompose the turbulent boundary layer (TBL) excitation in terms of spatially uncorrelated point force excitation with random phases. They have used an Corcos model to model the turbulent wall pressure and predicted the vibroacoustics of plate using finite element software. Similar kind of TBL modelling studies were carried out by [Tengzelius, 2010] to compare the direct FE, FE/Modal and random FE computation approaches for TBL excitaion. The numerical alogirthm used in random sampling is given in [Coyette *et al.*, 2009] and [Wittig and Sinha, 1975]. The major assumptions in this method are turbulent wall pressure on the plate is a weakly stationary and homogeneous random process with positive definite cross spectral density matrix (Hermitian matrix for TBL and real matrix for diffuse field). The essence of this method is approximating the spatially correlated TBL excitation with multi load distributed, time correlated deterministic excitation. Using this approach the power input is calculated using a traditional deterministic multiload solver instead of the expensive joint acceptance integration in spatial domain.

2.9 Conclusions

The bulk of the research on modelling the TBL WPF is based on empirical or semi-empirical models. The empirical models for WPF till date are essentially curved fits for the scaled experimental data which are not capable of capturing the physics of the low speed separated flows with realistic flow conditions and geometry. Even though Chase and it's derivative models looks promising, they are suitable for few applications. The contribution of low

wave numbers and acoustic region to the response is well evident from literature. Even with today sensor, capturing the low wavenumber WPF were very difficult as it requires of costly MEMS sensors and control of the background noise in the wind tunnel. These demands on the wind tunnel facilities make the wind tunnel tests prohibitive. Hence a CFD based numerical model that can capture accurately the low wavenumber and acoustic component of WPF is investigated in this study. The numerical method based on LBM combined with a turbulence model such as VLES will be used as it provides an accurate and efficient approach to high Reynolds number flow simulation unlike other DNS and LES codes. From the exhaustive literature review, it can be concluded that the TBL input power to structure due to WPF excitation can be calculated in three numerical methods. All the three methods, makes use of the finely resolved unsteady CFD WPF. These three methods were to deduce an empirical model from CFD predicted WPF, caluclate TBL power input in wavenumber domain using CFD WPF and random sampling of CFD WPF. Finally the vibro-acoustics will be calculated in modal domain and validated with experiments.

CHAPTER 3

IDENTIFICATION OF EMPIRICAL TBL MODEL PARAMETERS FROM CFD WALL PRESSURE [1]

3.1 Introduction

An accurate unsteady CFD simulation is required to capture not only the convective ridge but also the acoustic contribution to the wall-pressure cross-spectral density and then compute the power input transmitted to a structure by the flow excitation accurately. The complex pressure field on a side-glass usually stems from two main sources: the wake of the side-mirror on the one hand, and the flow separation and large vortical structures generated at the A-pillar on the other hand. So these two typical bluff bodies a) flat fence representative of A-pillar and b) side mirror are considered in the present study. Most of the earlier studies [Höld *et al.*, 1999; Pérot *et al.*, 2009; Senthooran *et al.*, 2006] were based on power spectral density of the wall pressure calculated from a short pressure time history (0.5-1.5 sec) which could not yield two-point correlations that needed to be modeled to compute the vibroacoustic response. Indeed, as turbulent wall-pressure excitation on the plate is clearly a spatial random process, it requires a two-point statistical description of the excitation. In this chapter, the statistical description of the wall pressure fluctuations (WPF) in a non-equilibrium turbulent boundary layer (TBL) are obtained from a lengthy CFD run using Lattice-Boltzmann solver PowerFLOW. To achieve statistically converged turbulent flow, a lengthy computational fluid dynamics (CFD) simulation was conducted. The long period of time history helps to obtain a better estimate of the second order statistics accurately. Statistical descriptors such as mean flow, wall pressure spectra and two point correlations of the wall-pressure results are validated for both cases with experiments conducted at wind tunnel in Purdue University. The resulting aerodynamic numerical results are compared to the experimental data. Unsteady numerical simulation results are also validated at every stage with experiment. The wall-pressure PSD roll-off slopes were also identified and verified. The post-processing of the unsteady wall-pressure fluctuations were done using k-ω code developed as a part of this work. The mathematical relations behind the k-ω code are available in[Arguillat *et al.*, 2005; Francois *et al.*, 2011]. The in-house code developed has dual purposes, firstly to handle larger amount of wall-pressure

1. Part of this chapter was published in AIAA conference see [Vadavalli *et al.*, 2011]

data due to the long enough time histories and secondly as a convenience in the calculation of TBL power input to structure. k-ω code is based on FFT techniques and can be used to study non-homogeneity. The k-ω code has been thoroughly validated with analytical Corcos model in Section 3.4.4 similar to [Arguillat *et al.*, 2005]. From a spatio-temporal analysis of the turbulent flow the convection and acoustic zones are captured correctly, which are the major sources of excitation and transmission respectively. Using the CFD wall-pressure coherence on the plate, homogeneous zonal based Corcos model parameters like convection velocity and decay coefficients have been determined by non-linear curve fitting. The homogeneous zone are segregated based on the mean skin friction and PSD variation on the plate. The identified empirical model parameters are validated with experiments and later used to predict the vibro-acoustic indicators for the plate. Vibro-acoustic indicators for fence and side mirror cases are calculated using both CFD-derived parameters and finite element method. These results are validated with experiments on a plate-cavity system.

3.2 Aerodynamic simulations

3.2.1 Test cases and experimental data

The flat fence and side mirror placed in a wind tunnel experimental set-up at Purdue University [Park *et al.*, 2004] are shown in Figures 3.1(a) and 3.1(b). The fence is at a 55° with respect to the wind tunnel floor. In those experiments, an array of accelerometers is used to measure the plate velocity and a microphone is used inside the anechoic enclosure under the plate to measure the transmitted sound. Wall-pressure measurements were made with a 6.5 mm diameter microphone array spaced at 38 mm for side mirror and 50 mm for fence. The probe measurement locations in the CFD simulations are shown in Figures 3.2(a) and 3.2(b). These are exactly the same locations as those used in the Purdue University wind tunnel experiment. The present study aims at simulating these experimental set-ups with a Lattice-Boltzmann method [Chen, 1998; He and Luo, 1997] (LBM) using the commercial solver PowerFlow 4.2c and validate the accuracy of the method by comparing its unsteady prediction of the wall-pressure field on the plate with measurements.

A full wind tunnel set-up is created around each bluff body (fence and side-mirror) mimicking as closely as possible the Purdue experimental setup and probe locations. Uniform inflow is imposed upstream. A CFD simulation was setup with flat fence and side mirror solid models inside a PowerCASE digital wind tunnel template. The inlet and outlet boundary conditions for the wind tunnel are streamwise velocity and static pressure respectively with reflection damping. The ceiling and walls are friction less except a little roughness added

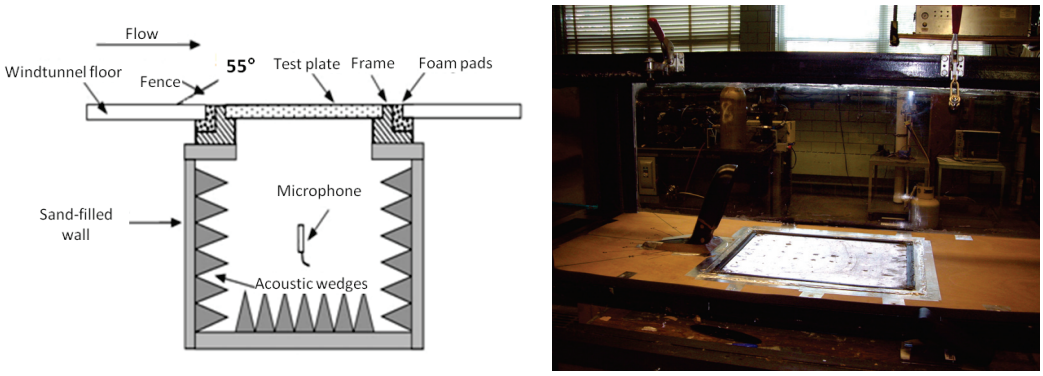

(a) Sketch of the flat-plate experimental set-up (b) Side mirror experimental set-up

Figure 3.1 Test cases considered

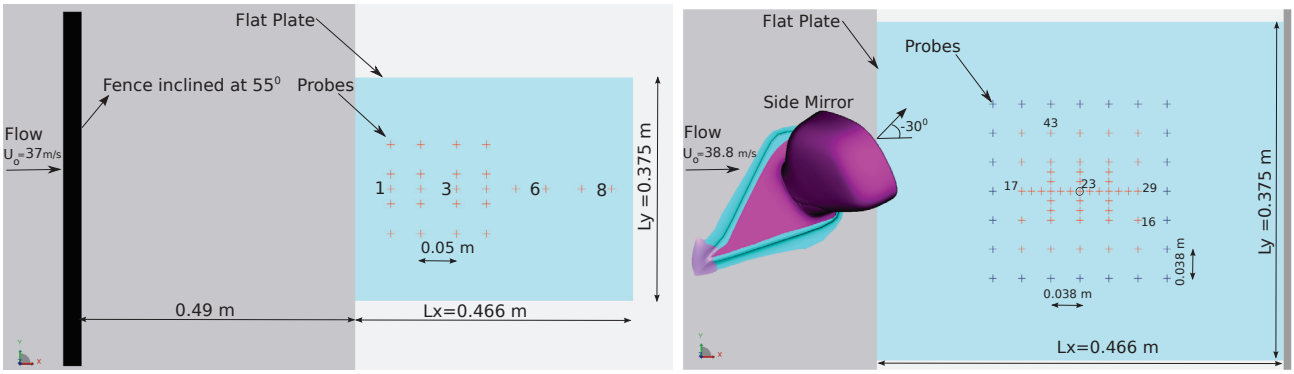

(a) Sketch of the flat-plate experimental set-up (b) Side mirror experimental set-up

Figure 3.2 Probe locations in Experimental set-up

before the leading edge of plate to create sufficient turbulent flow. The finer surface mesh is approximately 1 mm to 2 mm in physical space on the flat plate and finest timestep is around 3.7 to 4.6 millionth of a sec, so as to resolve the unsteady wall-pressure. Figures 3.3 and 3.4 depict the solid models, Variable Resolution (VR) regions and CFD grids for fence and side mirror case respectively. The probes on the plate have finer diameter (1mm) than in the experiment.

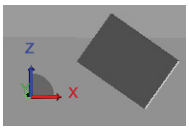

(a) solid model of flat-plate

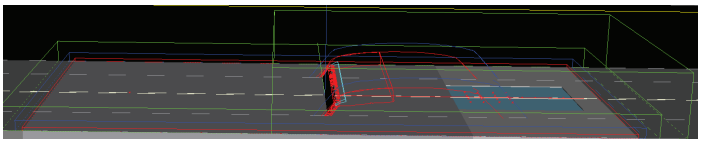

(b) Variable Resolution regions for flat-plate

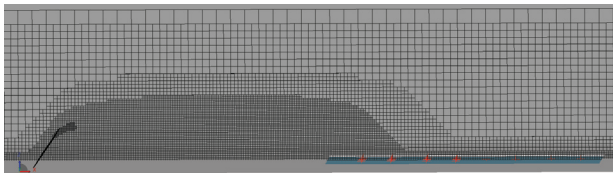

(c) CFD grid for fence

Figure 3.3 CFD simulation setup for Flat Fence

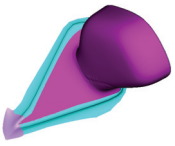

(a) sidemirror-geometry

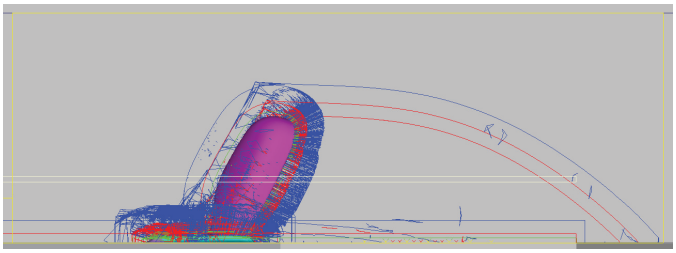

(b) Variable Resolution regions for mirror

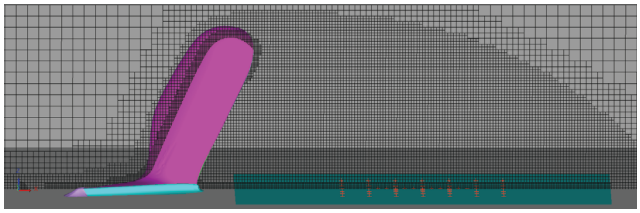

(c) CFD grid for mirror

Figure 3.4 CFD simulation setup for side mirror

The smallest voxel size (the elementary cubic element in the LBM method) is 0.75 mm for the fence and 1 mm for the side mirror with 7 levels of grid refinement for both cases to yield 20.4 (8.65 Fine-equivalent Million voxels) and 12.58 millions voxels (7.5 Fine-equivalent Million voxels) in the fence and the side-mirror grids respectively. The fine grid on the

plate shown in Figure 3.5 is a visualization of surfels (planar elements) with spacing of 0.75 to 1 mm to capture the turbulent wall-pressure fluctuations. The CFD simulation run time is approximately 72 hours for flat fence and 120-160 hours for side mirror case on a Calcul Québec super computer.

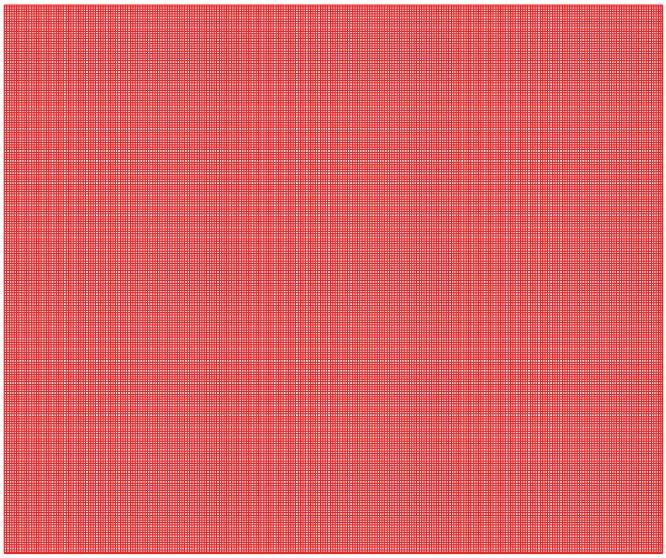

Figure 3.5 Fine grid on the plate for fence and mirror cases

3.2.2 Monitoring the CFD simulation run

A 3D Very Large-Eddy Simulation (VLES) is performed on this virtual wind tunnel volume size (40.06 m x 1.152 m x 1.024 m) for a long enough time, larger than 10 sec for both cases, which has not been done in previous works to achieve statistical convergence similar to the measurements and resolve the low frequency content of the pressure fluctuations. The time stationarity required was achieved with a long simulation run. Due to the long enough CFD simulation, there exists an inconvienience in post-processing of huge amount of transient wall-pressure data. As a statistically steady state was reached that was checked by monitoring the Cp, lift and drag history for the whole plate-mirror system inside the digital wind tunnel as shown in Figure 3.6. But in fence case, the pressure coefficient Cp was calculated instead of lift due to non-flush plate mounting in case setup. Mean values, first and second-order correlations have been collected after skipping the first few seconds of transients to get a total steady state time history for 6 sec for the fence (1 time step = 3.686e-06 sec) and 7 sec (1 time step = 4.593e-06 sec) for the side-mirror, which are similar to the actual measurement times in the experiment.

Lift and drag time history for the flat fence and side mirror as shown in Figure 3.7 was time-averaged over 1 sec. The coefficient of lift C_l for fence and side mirror was 0.58 and 0.055 respectively. The coefficient of drag C_d for fence and side mirror was 0.87 and 0.62

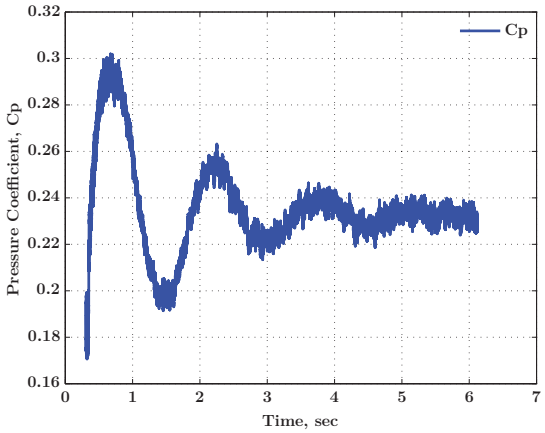

(a) fence: Fluid Probe Cp at x= 0,y= 0,z= 0.045 m

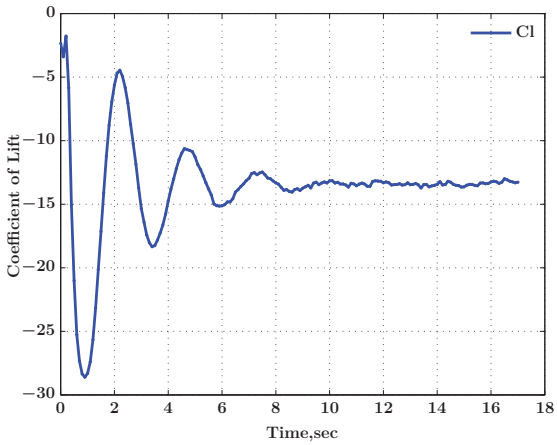

(b) mirror: Coefficient of lift for full system

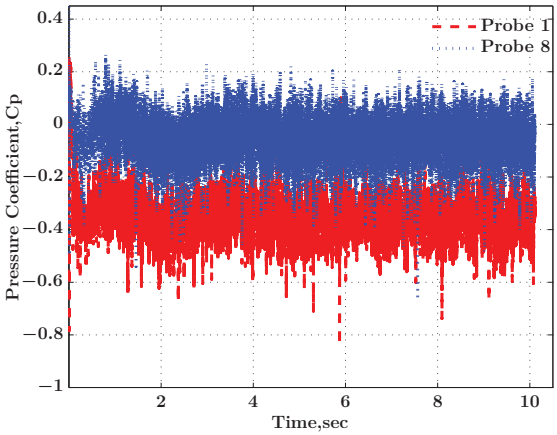

(c) fence : Plate Surface Probe Cp

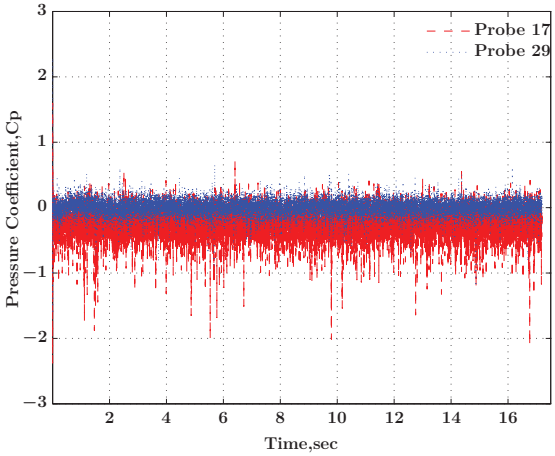

(d) mirror: Plate Surface Probe Cp

Figure 3.6 Cp and lift time history for the whole plate-side mirror system

respectively. The ratio of lift to drag ratio for fence and side mirror was 0.67 and 0.089 falls well within the range of typical bluff bodies around 0.1- 0.05 [White, 1999]. In bluff bodies, the drag force is dominant term compared to lift force unlike streamlined bodies. The drag force is 1.5 times the lift force in fence case. In side mirror case, drag force is 11 times stronger than the lift force. It implies that flat fence inclined at an angle (representative of A-pillar) is more streamlined than the side mirror. There is limited amount of literature related to aerodynamics of flat fence and side mirror. But typical values of drag coefficient for various simple geometrical shapes are outlined in Chapter 7 of [White, 1999]. The drag coefficient for a generic side mirror determined from an incompressible Detached eddy simulation is 0.44 [Ask and Davidson, 2009]. Similarly, the drag coefficient for a half-cylinder (a broad representative of side mirror) determined from an incompressible LES is 0.71 [Pérot *et al.*, 2004]. In the present study, the drag coefficient for side mirror determined from compressible VLES is 0.62, perfectly falls within the range of 0.44-0.71 available in literature. It can be noted that an incompressible and compressible solver does not differ drastically in their estimates of drag and lift coefficients as noticed by [Khalighi *et al.*, 2010].

The instantaneous wall-pressure coefficient C_p on plate for fence and mirror case from CFD simulation is shown in Figure 3.8. In the case of side mirror, the wall-pressure on the entire plate is negative C_p compared to the flat fence that has almost positive C_p . It is evident from the drag values also that the side mirror is a stronger bluff body than the fence as it creates more suction area after mirror. The snapshot of flow structures are described from the perspective view of instantaneous Iso-surface at fixed value of lambda2 $= -0.1$. Figure 3.9 illustrates the wakes and vortices generated by the flat fence and side mirror.

3.3 Mean flow analysis

Figure 3.10 shows the flow topology in the mean streamwise cross-section of the wind tunnel. In Figure 3.10 (left), the fence triggers a large flow separation whose reattachment point extends beyond the leading edge of the plate as in the experiment Figure 3.10 [Park *et al.*, 2004]. In Figure 3.10 (right), the side-mirror also triggers a flow separation behind it but of much more limited extent. This is again very similar to Khalighi's LES results on a similar GM side-mirror [Khalighi, 2010]. The different flow regions (stagnation zone, recirculation zone and reattached zones) for flat fence and side mirror are clearly seen in the mean static pressure and velocity contours shown in Figure 3.11, which compare well with similar cases found in the literature. Mean turbulent kinetic energy(TKE) results for fence and mirror at the streamwise mid-section were shown in Figure 3.12.

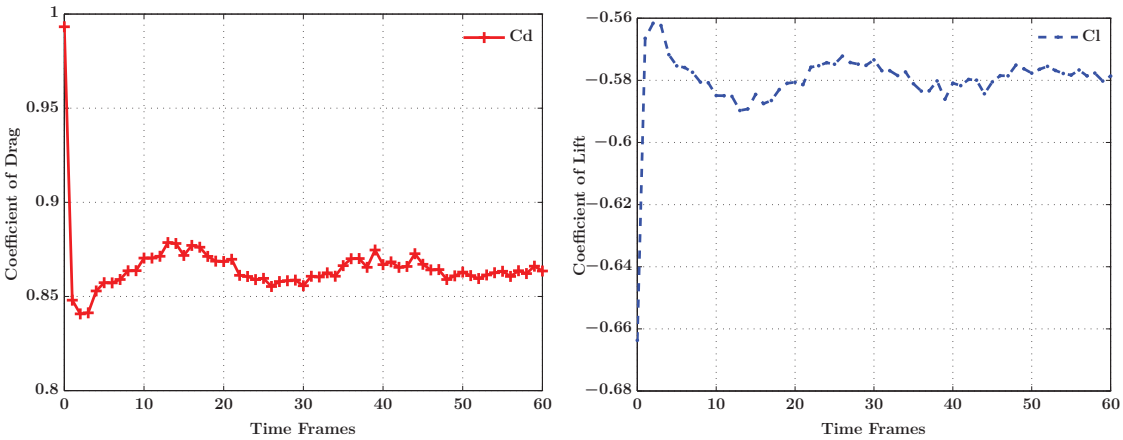

(a) Drag for fence (b) Lift for fence

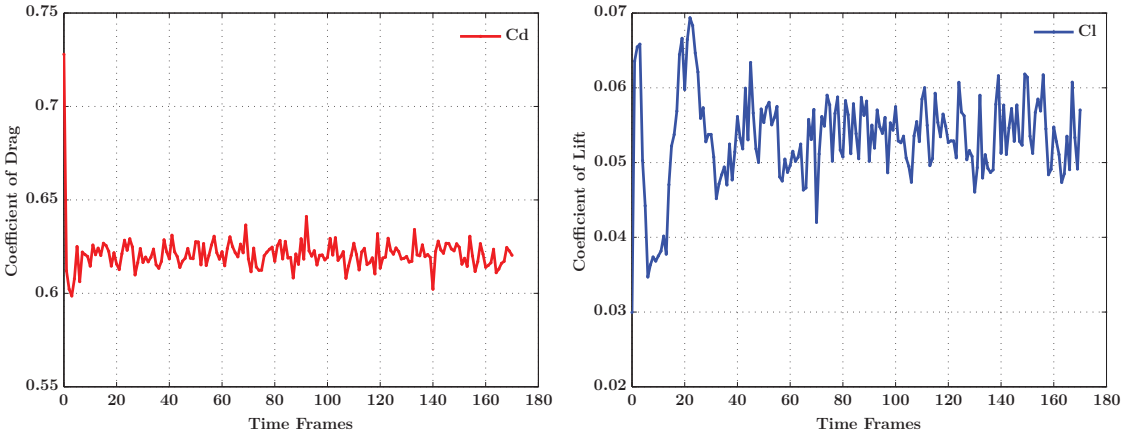

(c) Drag for side mirror (d) Lift for side mirror

Figure 3.7 Lift and Drag for fence and side mirror

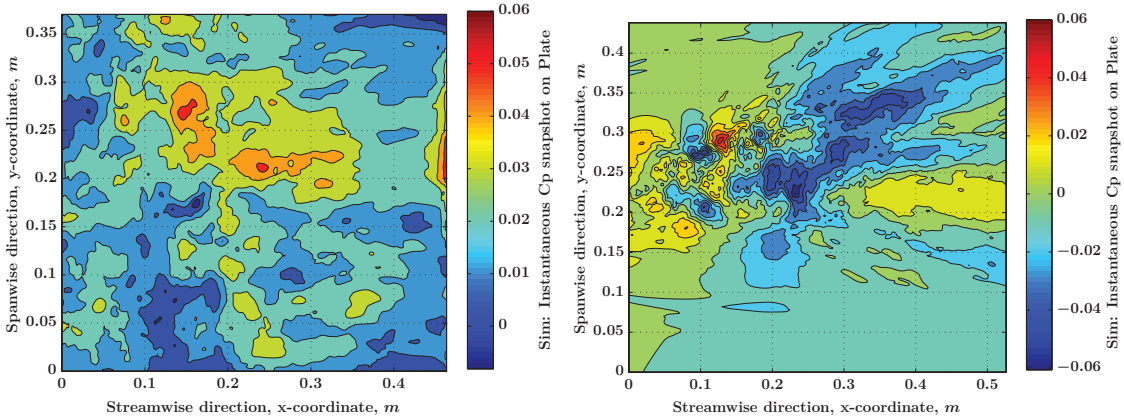

(a) fence-instant-cp (b) mirror-instant-cp

Figure 3.8 Instantaneous C_p for fence and side mirror

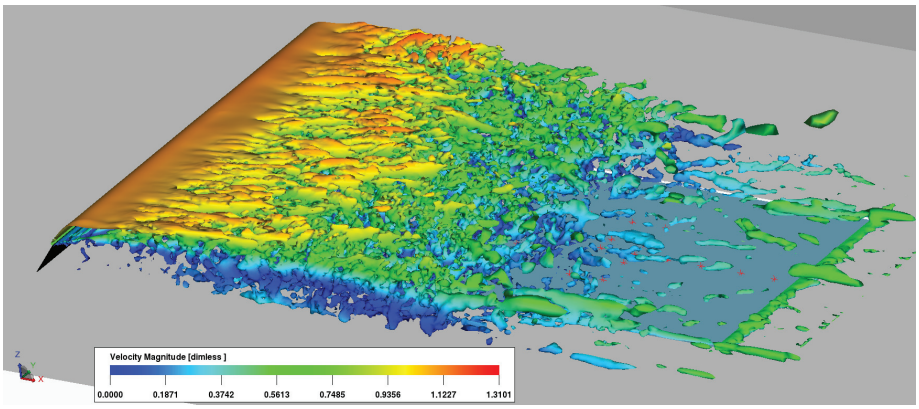

(a) fence-instant-iso-surface-lamda2

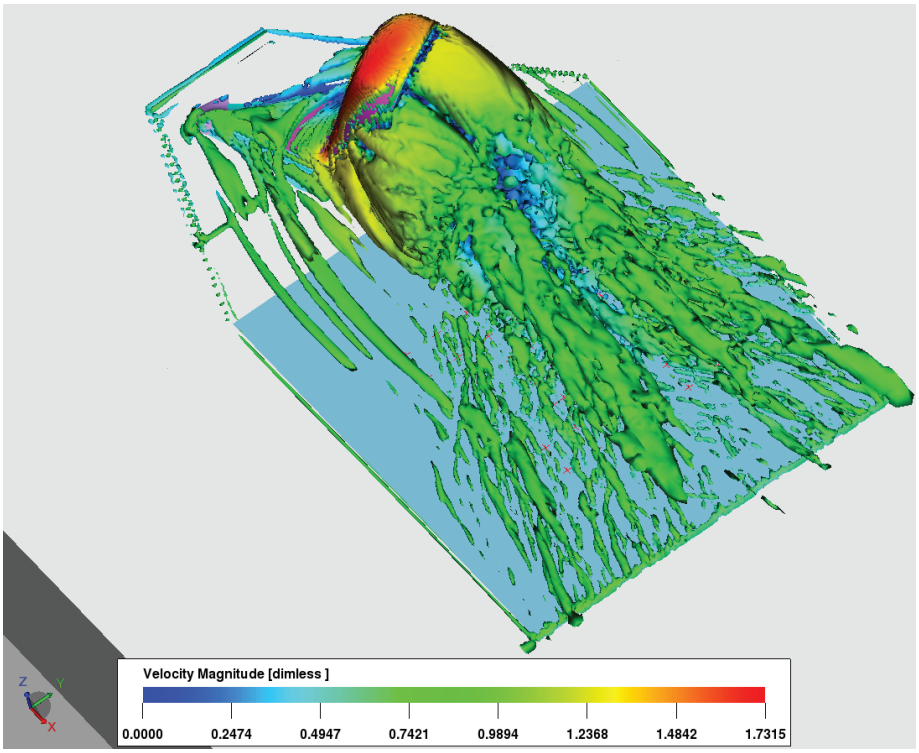

(b) mirror-instant-iso-surface-lamda2

Figure 3.9 Instantaneous iso-surface at lambda2 = −0.1 for fence and mirror

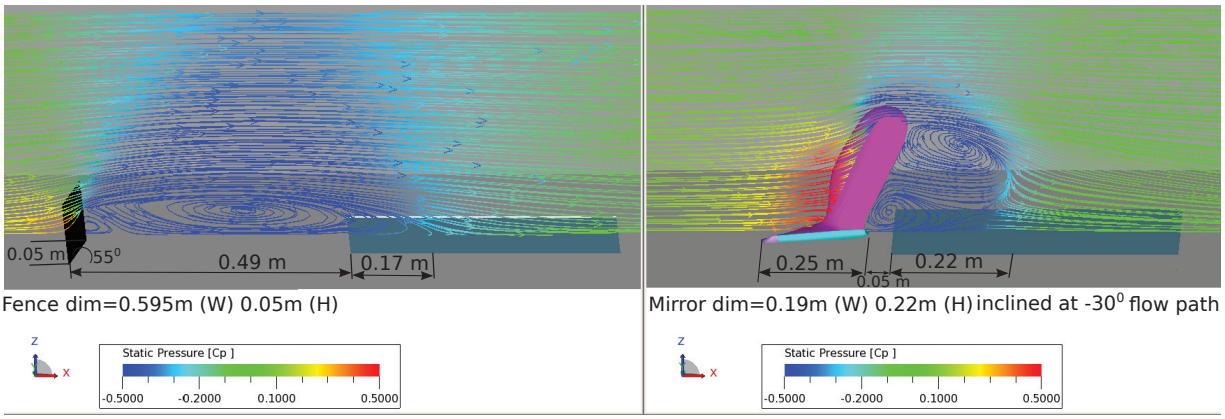

Figure 3.10 Flow field around the simulated bluff bodies fence and side mirror with reattachment distances

The array of 7 by 7 experimental probes locations on plate are shown in Figure 3.13(a), which are the same locations in CFD simulations. More quantitative assessment can be obtained with the comparison of the numerical wall-pressure coefficient C_p (normalized by the free stream variables) with the Purdue measurements in Figure 3.13(b) (experiment) and 3.13(c) (PowerFlow). The difference in C_p between the recirculation and the stagnation zone is 0.7 for the flat fence and 0.75 for the side mirror, which is a typical of bluff bodies. The recirculation zone for the fence is much larger than for the side mirror because the pressure drop across the fence is large. The mean wall-pressure distribution in Figures 3.13(b) and 3.13(c) behind the side-mirror in the separated and re-attachment zone are partially validated to what was measured with the pressure probes in the wind tunnel at Purdue University possibly due to the uncertainity error bars in measurement.

In mirror case, mean static pressure on part of the plate was obtained from CFD simulations and validated with experiments from Purdue University wind tunnel, see Figures 3.13. For the fence case, there was no experimental data available for comparison,therefore mean static pressure over the entire plate was shown in Figure 3.14.

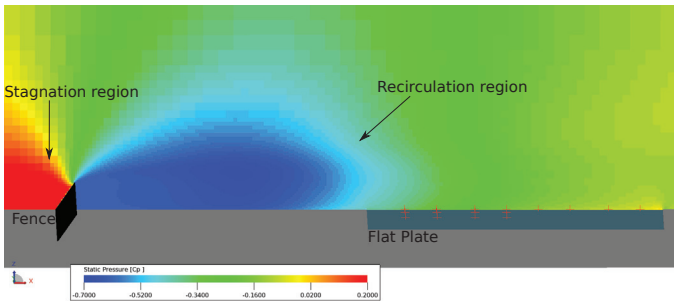

(a) Mean static pressure in the midsection of the plate for flat fence

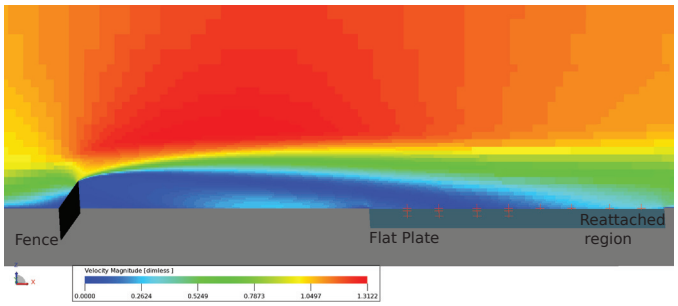

(b) Mean velocity magnitude in the midsection of the plate for flat fence

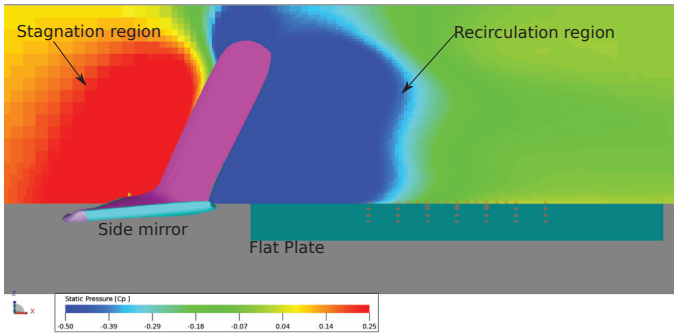

(c) Mean static pressure in the midsection of the plate for side mirror

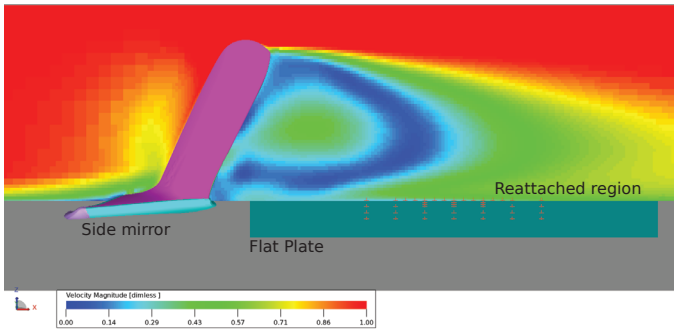

(d) Mean velocity magnitude in the midsection of the plate for side mirror

Figure 3.11 Mean flow results

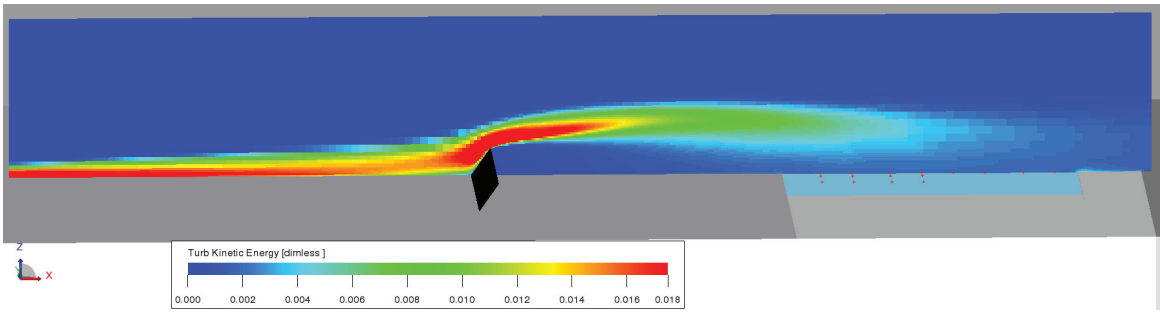

(a) Mean TKE in the midsection of the plate for flat fence

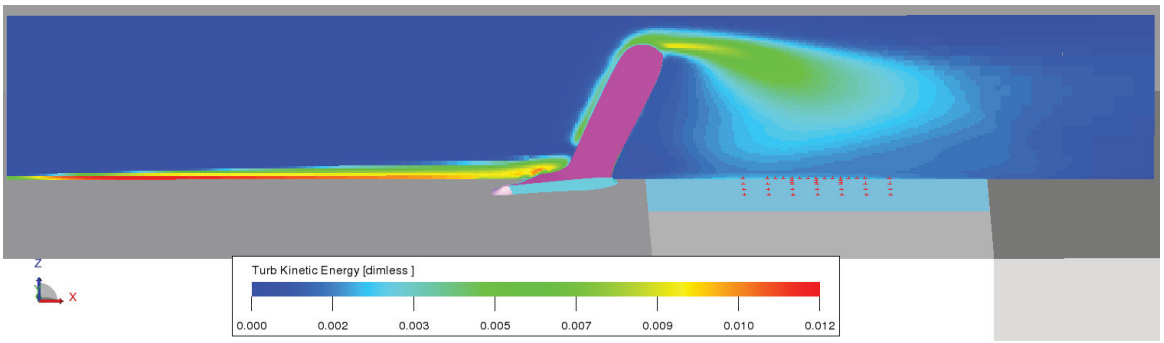

(b) Mean TKE in the midsection of the plate for mirror

Figure 3.12 Mean TKE flow results for fence and mirror

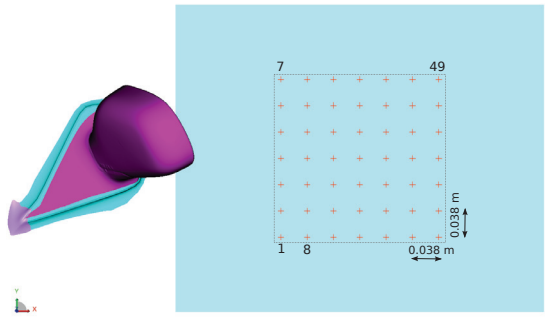

(a) Mean static pressure on the plate for side mirror case from 49 probes

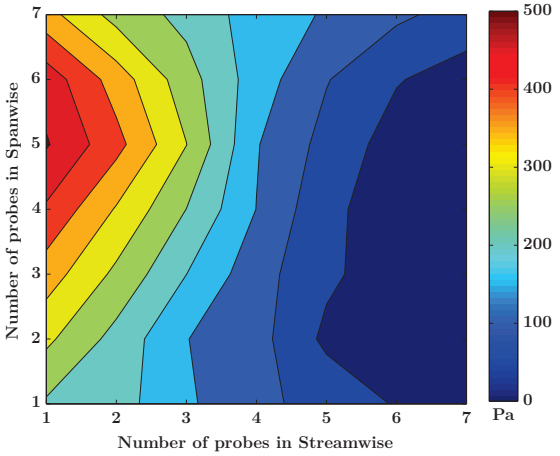

(b) Mean static pressure on probe section of plate for side mirror case from 49 probes in Purdue experiments

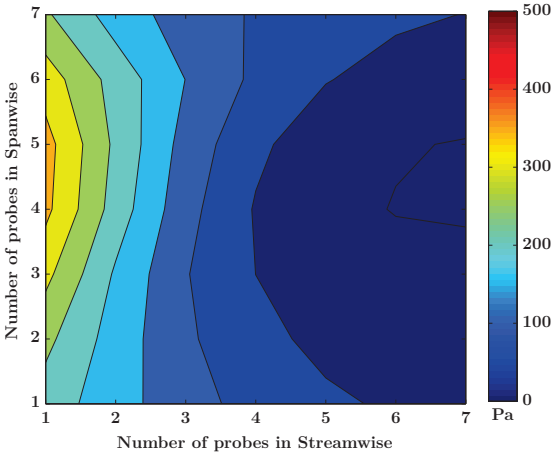

(c) Mean static pressure on probe section for side mirror case from 49 probes in CFD simulation

Figure 3.13 Mean Cp: Experiments and PowerFLOW

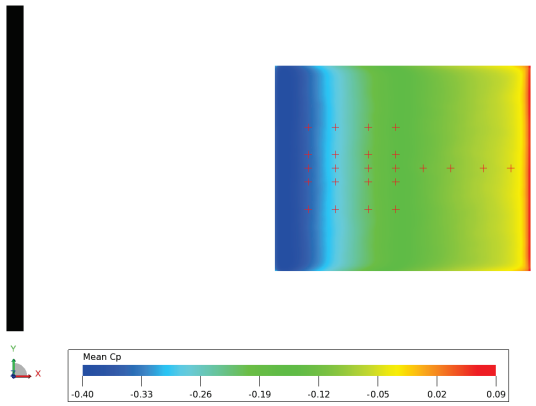

(a) Mean static pressure on the whole plate for fence case

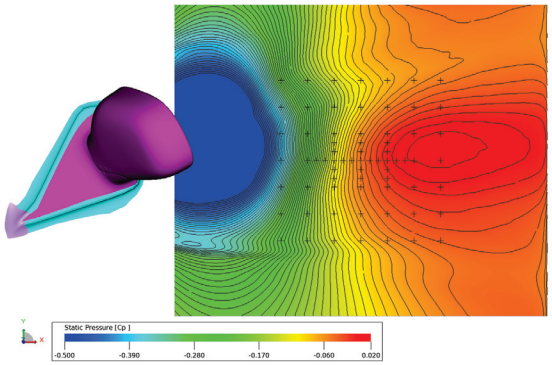

(b) Mean static pressure on the whole plate for side mirror case

Figure 3.14 Mean C_p from CFD (PowerFLOW) over entire plate

Boundary layer parameters and velocity profiles

Boundary layer parameters like inner variables and outer variables that are used in normalised PSD are determined from CFD simulations. These parameters are calculated at a location 1 m away from fence and mirror to ensure fully attached flow condition. The inner and outer variables are displayed in Table 3.1

Inner variables and outer variables	Fence	Mirror
$U_\infty, m/s$	37	38.8
δ, m	0.105	0.198
$\Delta = \frac{\delta}{\delta^*}$	3.78	8.96
δ^*, m	0.027	0.022
$H = \frac{\delta^*}{\theta}$	2.21	1.47
θ, m	0.012	0.015
τ_w, Pa	0.29	0.63
τ_{max}, Pa	3.3	18.13
β_c	0.04	0.024
Π	0.51	0.49

Table 3.1 Inner variables and outer variables used in normalised PSD at Location 1 m away from fence and mirror

The mean streamwise pressure coefficient C_p and the corresponding mean streamwise velocity u_x at the centreline of the flat plate for fence case are shown in 3.15. Similarly in the Z-direction(height wise), both Cp and u_z are plotted for fence case in 3.16. For the mirror case, the mean streamwise and Z-direction dimension less pressure and velocity plots are shown in 3.17 and 3.18 respectively. The fence creates a larger pressure drop compared to the mirror. The mean C_p and u_x results depict the features of a typical bluff body flows. A surface contour plot in mid-streamwise section, across the centre line of the plate are shown in 3.19(a) for fence case and 3.19(b) for mirror case.

The streamwise development of velocity profile across the plate starting from the free-stream to the plate leading edge and beyond the plate trailing edge is presented in Figures 3.20(a) and 3.20(a). Boundary layer parameters mentioned in Table 3.1 like Turbulent Boundary Layer(TBL) thickness are determined from these mean velocity profiles. These boundary layer parameters form the basic inputs for certain RANS based semi-empirical spectral models. To get a better understanding of the streamwise velocity profiles, the velocity

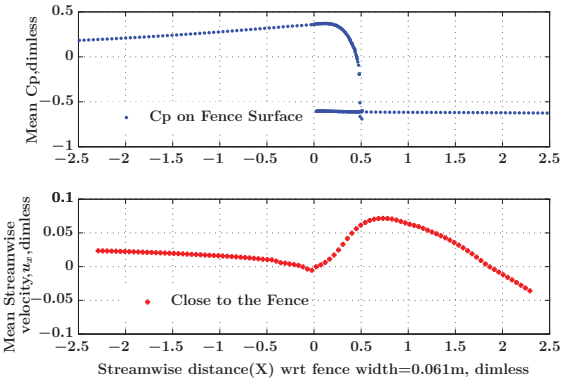

Figure 3.15 Mean streamwise C_p and u_x at the centreline of the plate for fence

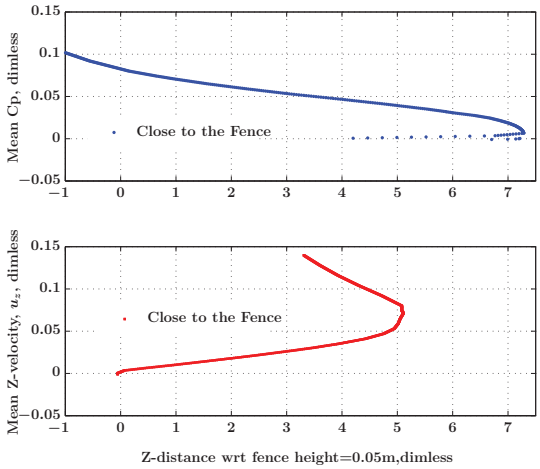

Figure 3.16 Mean streamwise C_p and u_x in the z-direction for fence

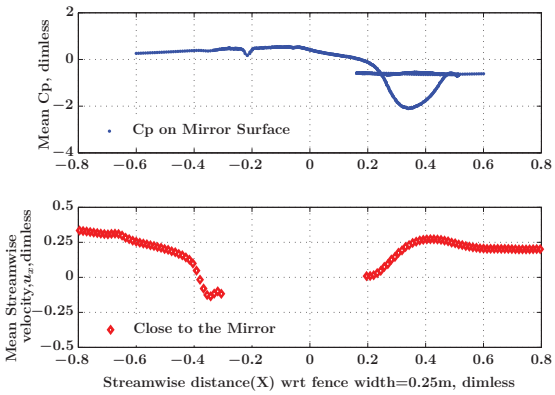

Figure 3.17 Mean streamwise C_p and u_x at the centreline of the plate for mirror

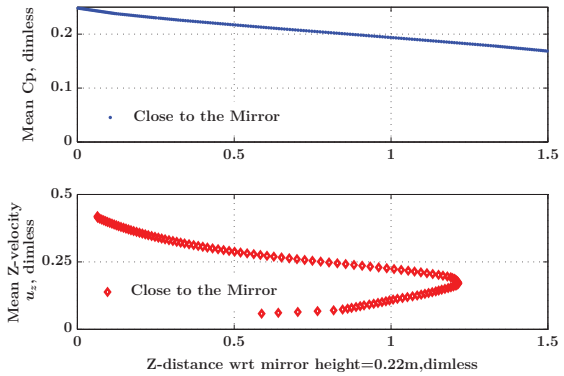

Figure 3.18 Mean streamwise C_p and u_x in the z-direction for mirror

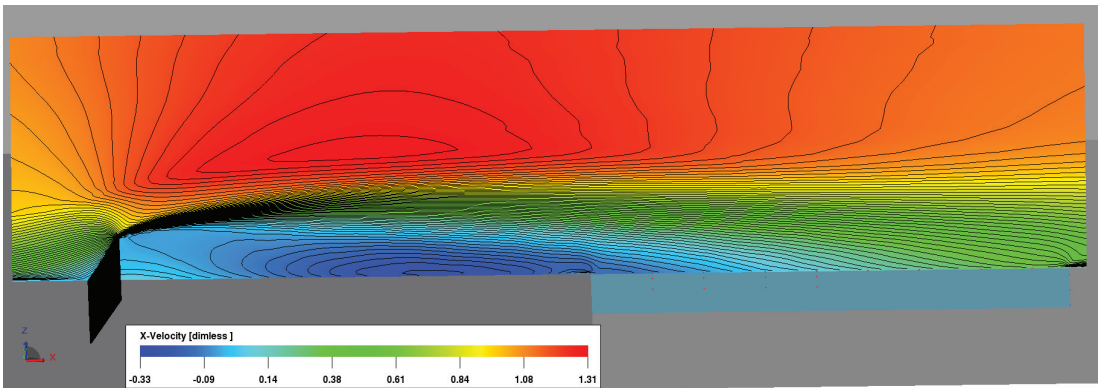

(a) Mean streamwise x-velocity at mid-streamwise contour for fence

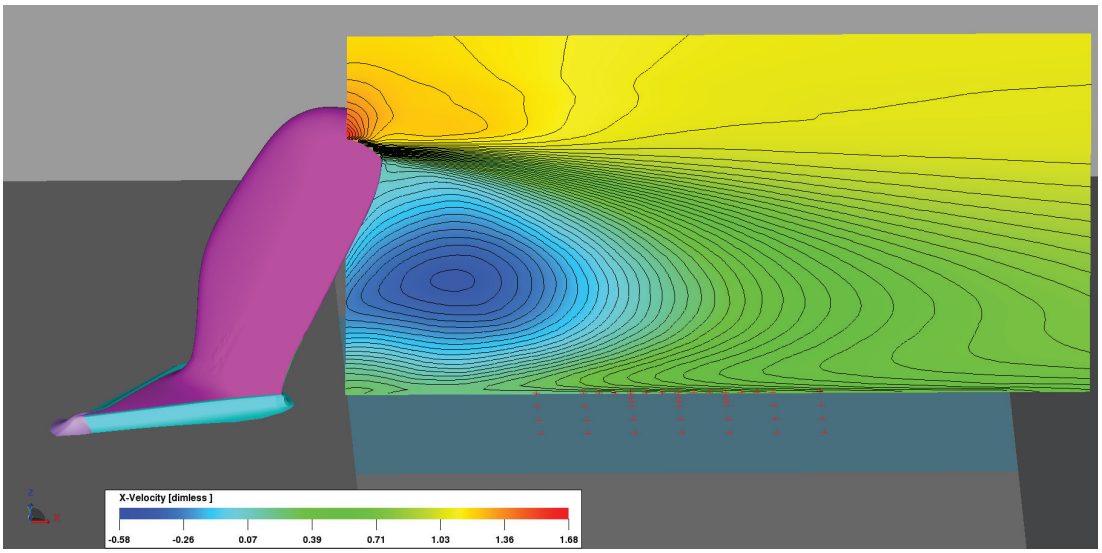

(b) mirror xvelocity midspan contours

Figure 3.19 Mean streamwise X-velocity at mid-streamwise contour for mirror

profiles are normalised with respect to inner variables as outlined in Table 3.1. The comparison of normalised velocity profiles with respect to the log-law (law of the wall) and Coles wake law [Coles, 1956] are presented in Figures 3.21(a) and 3.21(b). As discussed earlier in Section 2.3.4, the classical Blasisus velocity profile does not compare well with fully developed turbulent mean streamwise velocity profile for fence and mirror as shown in Figure 3.22 which is normal and as expected due to the presence of pressure gradients in both test cases.

3.4 Unsteady flow analysis

In this section, we move from time invariant statistics to time-variant statistics to characterise the pressure field. The next step has been to compare the wall-pressure spectra at several locations for both configurations. Figures 3.23(a), 3.23(c) and 3.23(f) clearly show excellent agreement between the LBM results and the measurements. Similar agreement is found at all sensor locations. The difference in autospectrum seen at higher frequencies is attributed to the experimental probe diameter cutoff frequency (around 1500 Hz for a 6.5 mm diameter probe). In the side-mirror case, even the slight vortex-shedding frequency seen in the experiment at 65 Hz is well captured. When moving to the second-order correlations that proved to be much more challenging in the past, both the coherence in the streamwise and spanwise directions show nice decays with an exponential shape as expected in Corcos model.

3.4.1 PSD: simulations vs experiments for side mirror

The wall-pressure auto power spectral density (PSD) simulated and measured over 45 probes on the plate surface for side mirror case is shown in Figure 3.24(a) and Figure 3.24(b) respectively. The spatially averaged PSD over 45 probes from experiments and simulation match well above base frequencies except a minor mismatch at the vortex shedding frequency as shown in Figure 3.24(c). This mismatch may be possible due to large frequency resolution in the PSD from CFD simulations. The spatial schematic representing the exact location of 45 probes over the plate remain the same, both in experiment and simulation as shown in Figure 3.24(d). These probes are spaced with distance varying from 12.7 mm to 38 mm to capture the second order statistics like cross spectrum, coherence. Although the PSD amplitude levels and roll-off were predicted well in simulation, there exists a slight spread in the amplitude levels compared to that of experiments. Due to the probe diameter cutoff limitations, some of the experimental probes could not measure the high frequency variations in wall-pressure PSD. But on a whole, the CFD simulation results have predicted good quality PSD.

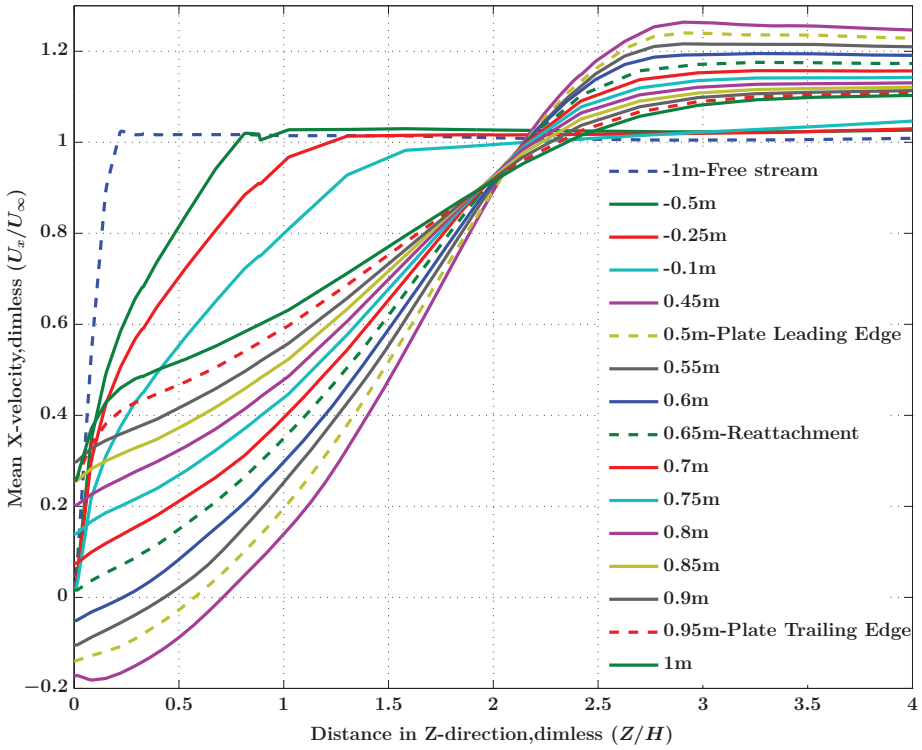

(a) Mean streamwise center-line velocity for fence case

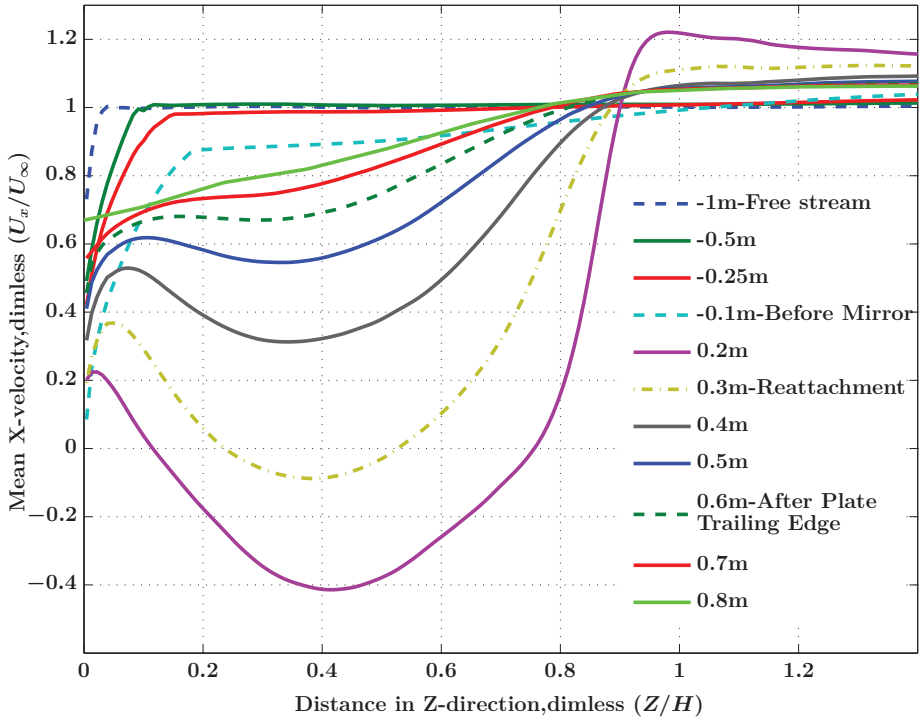

(b) Mean streamwise center-line velocity for side mirror case

Figure 3.20 Mean velocity profile development across the plate

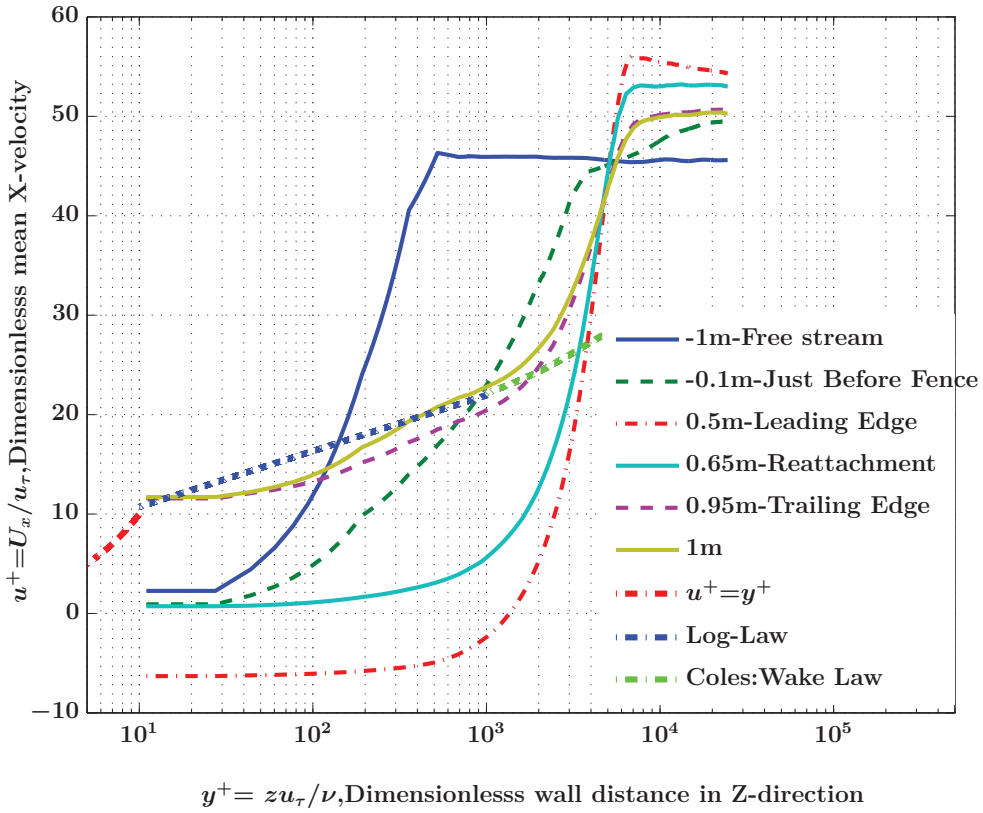

(a) Mean streamwise center-line velocity for fence case

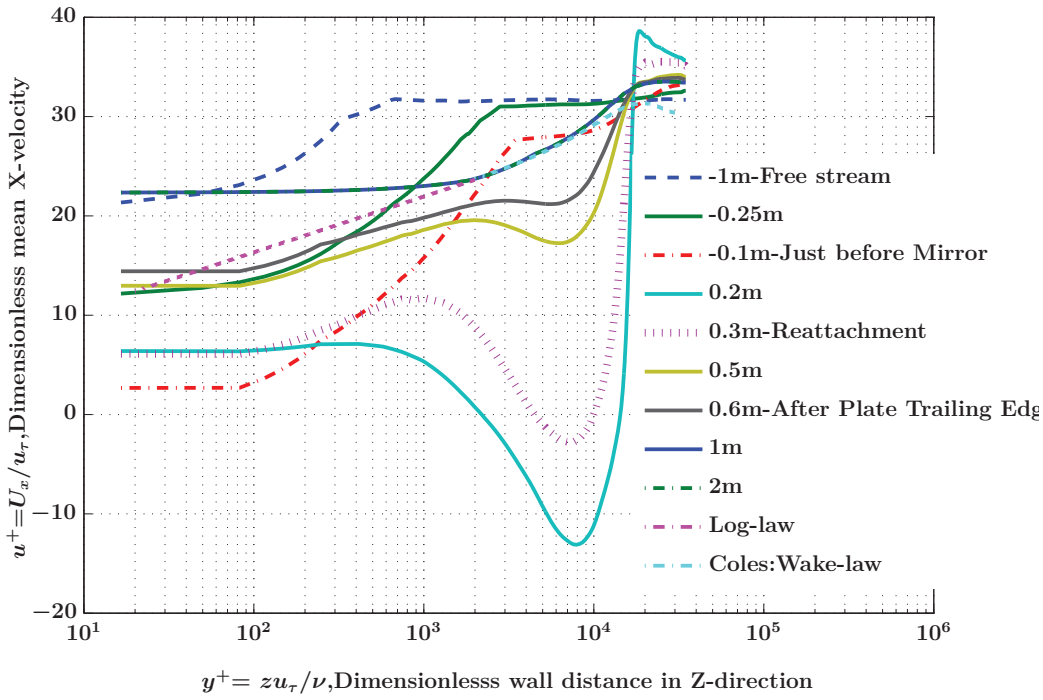

(b) Mean streamwise center-line velocity for side mirror case

Figure 3.21 Mean streamwise center-line velocity profiles normalised wrt inner variables

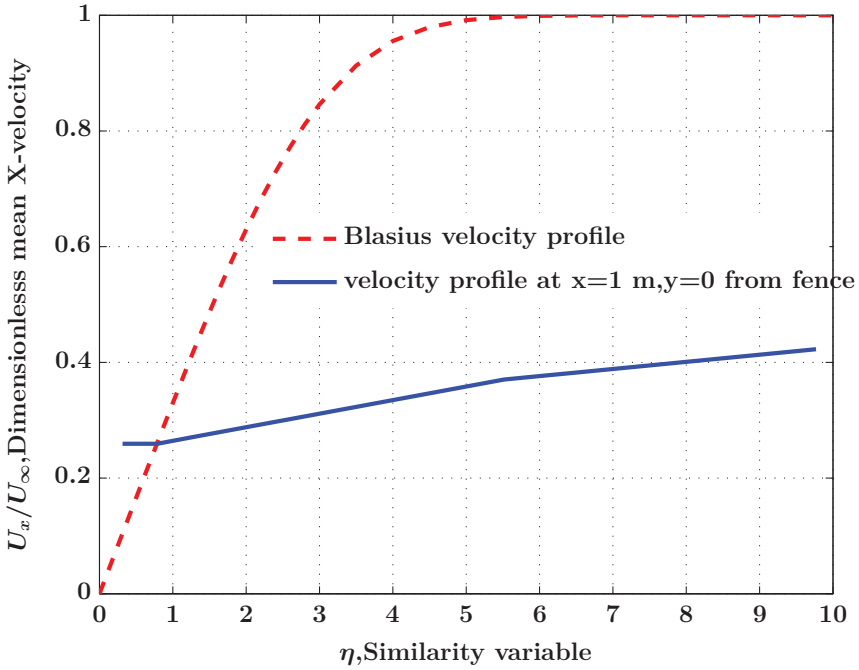

(a) Comparison of mean streamwise center-line velocity for fence case with Blasius Profile

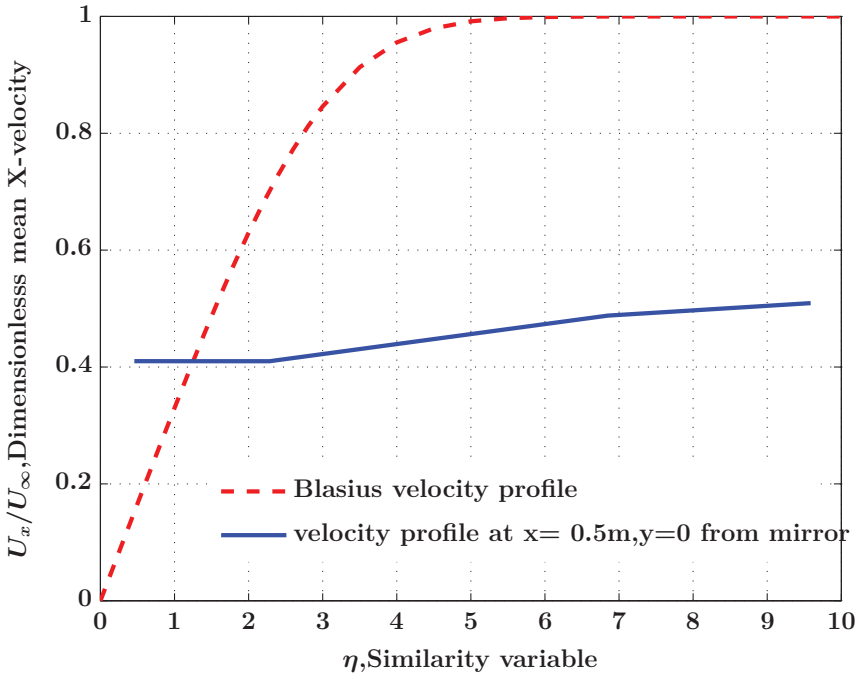

(b) Comparison of mean streamwise center-line velocity for side mirror case with Blasius Profile

Figure 3.22 Comparison of mean streamwise center-line velocity profiles with Blasius Profile

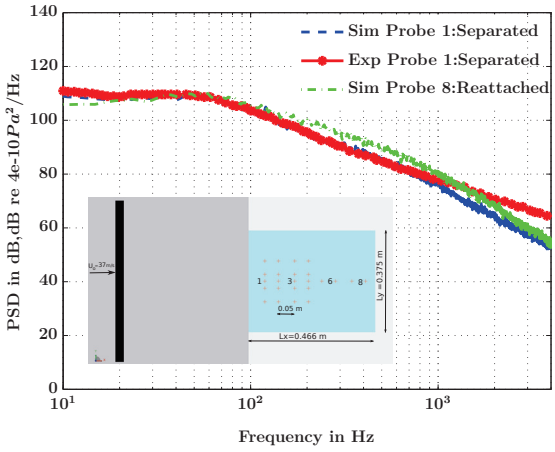

(a) Validation of the wall-pressure PSD or auto spectrum with experiments for the flat fence case

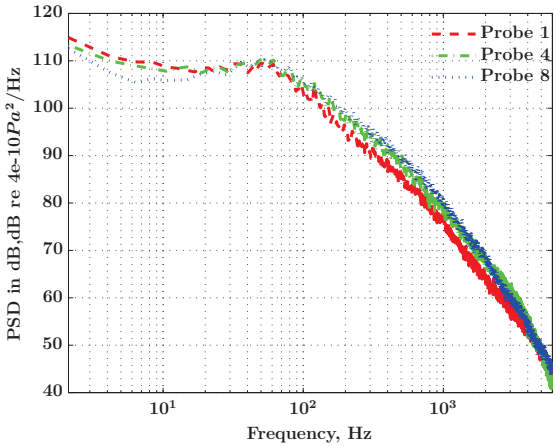

(b) PSD at various streamwise locations to test Homogeneity

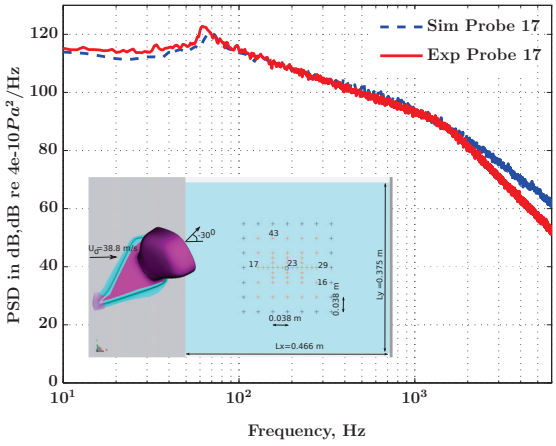

(c) Validation of the wall-pressure PSD in Separated region for side mirror case

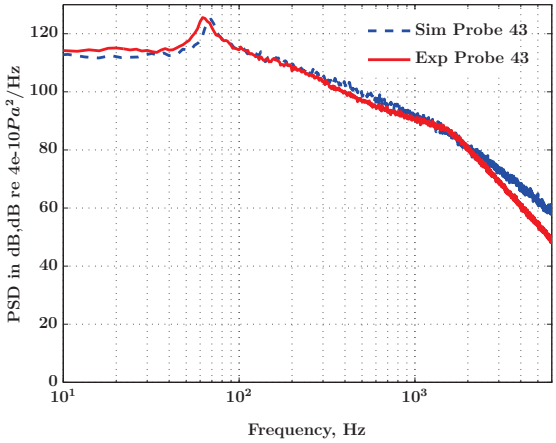

(d) Validation of the wall-pressure PSD in separated region for side mirror case

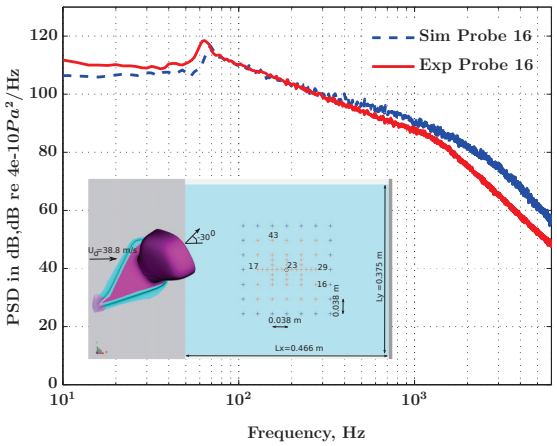

(e) Validation of the wall-pressure PSD in reattached region for side mirror case

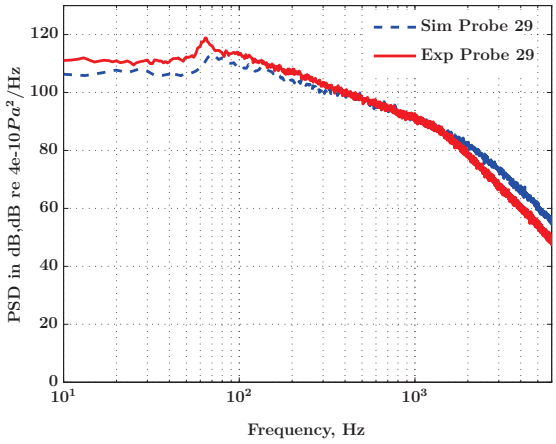

(f) Validation of the wall-pressure PSD in reattached region for side mirror case

Figure 3.23 PSD for fence and mirror

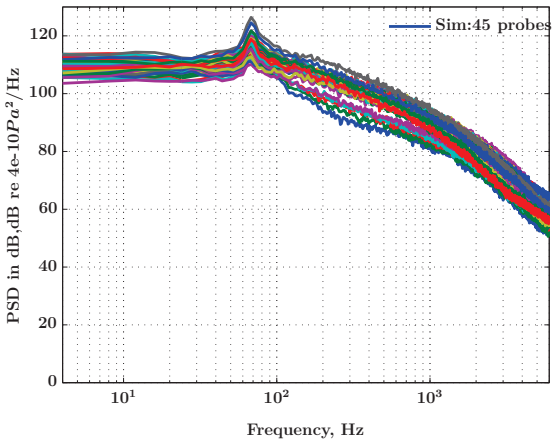

(a) Simulation: PSD for probes in side mirror case

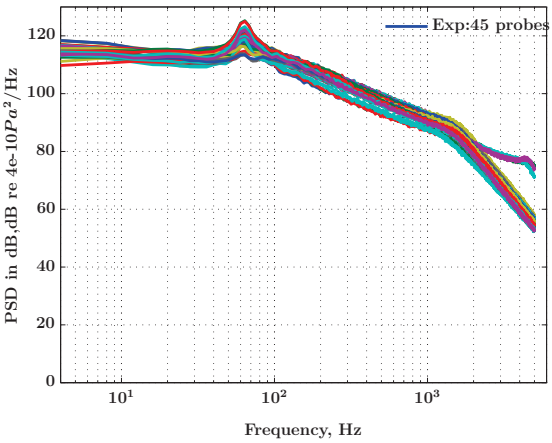

(b) Experiment: PSD for probes in side mirror case

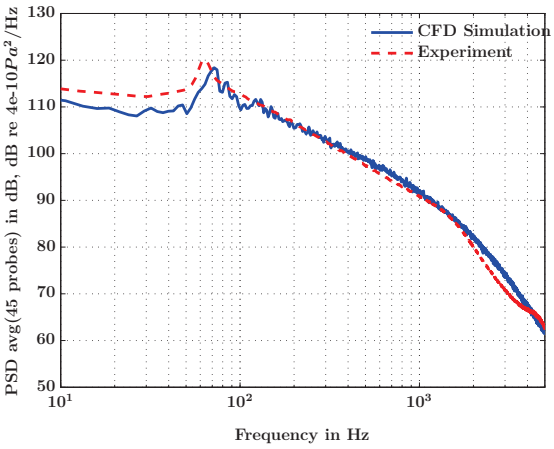

(c) Spatially averaged PSD simulation and experiments for side mirror

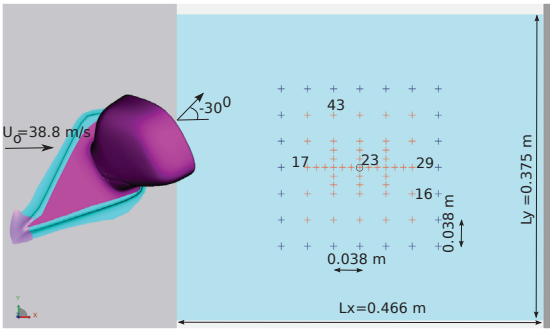

(d) Location of Probes in CFD Simulation and experiments for side mirror case

Figure 3.24 Spatially averaged PSD simulation and experiments

3.4.2 Fence side mirror PSD roll off

The term "roll-off" is mostly used in the electronic design of fiters in the area of signal processing but its concept can be attributed to random signals too. Roll-off determines the drop in the signal power per fixed frequency band width, usually denoted in terms of decibels per decades or dB/octave. To have an estimate of the roll-off, the power (square of amplitude term) and frequency are plotted in terms of logarithmic scales, dB and Hz. If its a power spectral density of the signal, the power spectrum has to be normalised with the freqency bandwidth. The PSD determined in separated and reatached regions using CFD simulations are shown in Figure 3.25(a) and Figure 3.25(b). The PSD roll-off (decay rate or change in slope) for separated region in Figure 3.25(a) is 20 dB/decade in fence case and with a decay of 22 dB/decade in mirror case. With an approxmiate selective curve fit at high frequencies for the PSD roll-off in separated region, the PSD would be proportional to $f^{-7/3}$ that closely matches with the generalized TBL wall PSD [Hwang *et al.*, 2009]. It may be noted that some of the empirical wall spectrum model like [Smol'yakov and Tkachenko, 1991] follows the similar decay rate at higher frequencies as discussed by [Hwang *et al.*, 2009]. The PSD roll-off (change in slope) for reattached region in Figure 3.25(b) is 20 dB/decade in fence case and with slower decay of 17 dB/decade in mirror case. The PSD roll-off for mirror in reattached region would be proportional to $f^{-5/3}$. To our knowledge, there is not much literature that deals with the PSD roll-off or decay rate for separated flows encountered with side mirror. In summary, the PSD roll-off for the fence case in separated and reattached regions remain same but in side mirror case due to the presence of strong separations and pressure gradients, the roll-off is faster in separated region when compared to reattached region.

The PSD obtained from the present CFD simulations have been compared with empirical wall pressure models namely [Goody, 2004] that incorporated the effect of Reynolds number and [Rozenberg *et al.*, 2012] that incoporates adverse pressure gradients. From a quick comparison of empirical models as seen in Figure 3.25(c) and Figure 3.25(d), it can be noticed that at higher frequencies above 1000 Hz, PSD using Rozenberg model matches well with that of CFD and experiments considering the fact that it was based on adverse pressure gradients in attached regions. The reason may be due to the inclusion of effect of adverse pressure gradients. As expected the Goody model underpredicts as it's proposed for zero-pressure gradient flows. Recently [Catlett *et al.*, 2015] also noticed that [Rozenberg *et al.*, 2012] model does not predict well, the PSD in the entire frequency spectrum, see Fig 18 Page 582 of [Catlett *et al.*, 2015]. Also [Hu and Herr, 2016] developed a new empirical spectral model for adverse pressure gradient with different experimental set of boundary layer scaling parameters and compared to that of earlier researchers like [Catlett *et al.*, 2015]

and [Rozenberg *et al.*, 2012]. It can be observed that, each model has its own limitations and works well with its own set of boundary layer parameters and experimental data. The benefit of using the empirical models is that they are not time intensive compared to the full CFD simulations and can be used for design iterative studies. The above empirical spectral models that include effect of Reynolds number and pressure gradients are highly dependent on the method and accuracy of extraction of boundary layer parameters either from RANS or experiments. Henceforth to predict the aeroacoustics or far field noise prediction, it is advisable to use the CFD simulations inplace of the empirical models due to their inability to precisely estimate the wall PSD over entire frequency range. It's noteworthy that the magnitude of the wall-pressure PSD combined with cross PSD always dictates the final amplitude of the far field sound pressure generated.

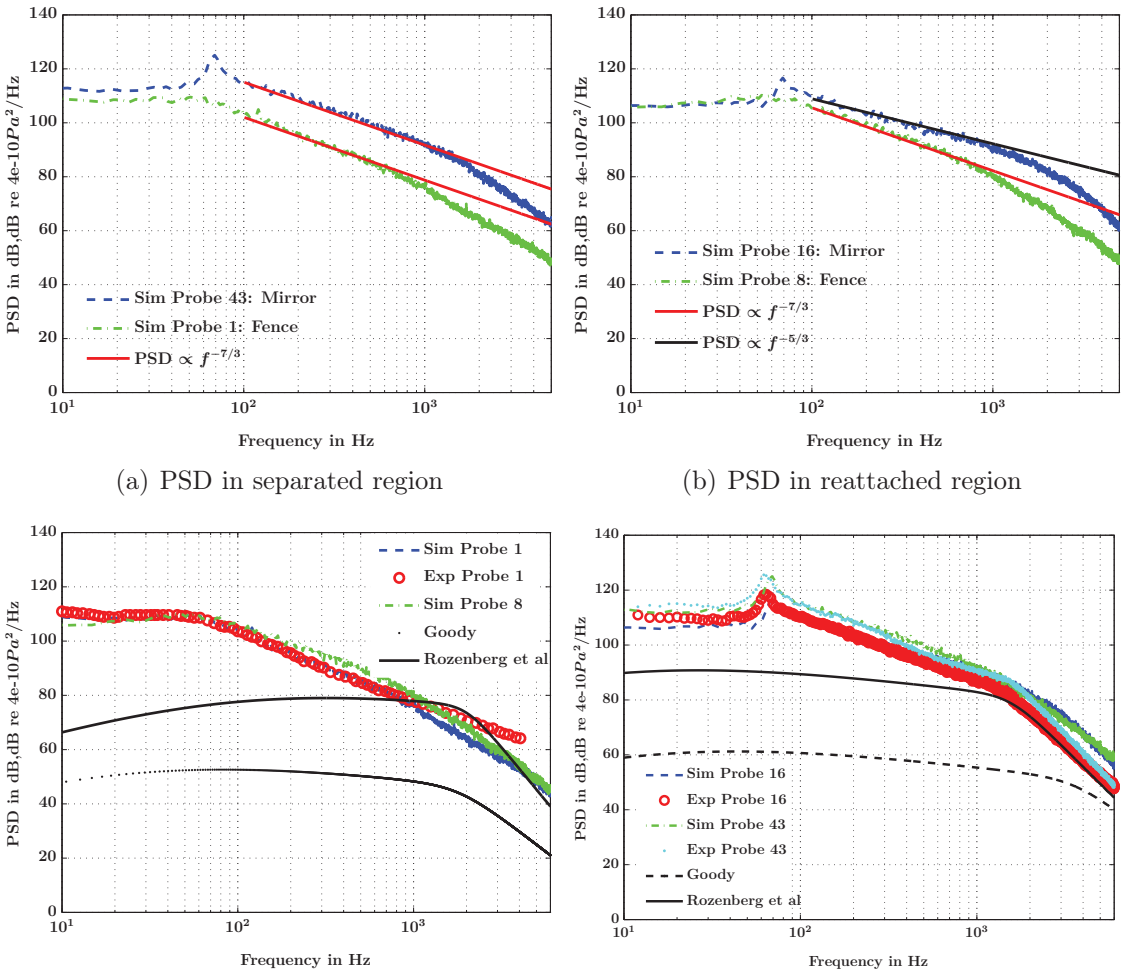

(a) PSD in separated region

(b) PSD in reattached region

(c) Fence: PSD via CFD vs Empirical models

(d) Mirror: PSD via CFD vs Empirical models

Figure 3.25 PSD roll-off from CFD and comparison with empirical spectral models for fence and mirror

3.4.3 Effect of side mirror yaw angle on PSD

The effect of side mirror yaw angle(clockwise and anticlockwise across the flow) on the wall-pressure PSD has been studied, keeping the same flow speed. As discussed in Section 1.4.2, the wall-pressure measurements were captured for the side mirror in positive yaw angle corresponding to $30°$ and negative yaw angle corresponding to$-30°$ across the flow direction. In both cases, the spatially averaged the wall-pressure PSD remains the same as shown in Figure 3.26. Henceforth with no effect on PSD due to the yaw angle of mirror, all the CFD simulations have been carried out with $-30°$ position in Figure 3.2(b).

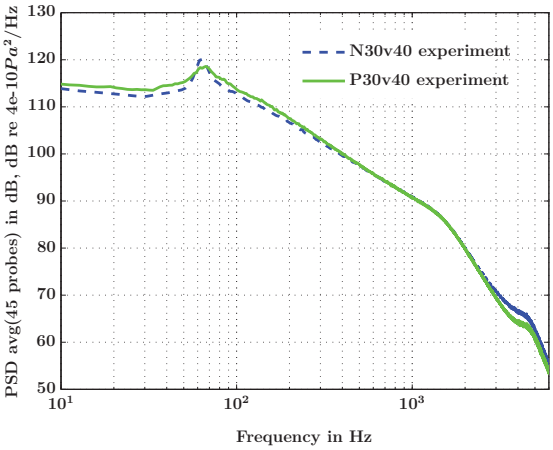

Figure 3.26 Spatially averaged PSD for mirror in $-30°$ vs $30°$ to flow direction

3.4.4 Spatio-temporal analysis of turbulent flow

This section basically deals with the study of two-point wall-pressure statistics like auto and cross-correlation (time-domain), cross-spectrum(frequency-domain), complex coherence(normalised quantity in frequency-domain), frequency-wavenumber spectrum(wavenumber-frequency domain). For a detailed descripton of mathematical expressions and its physical significance the reader is recommended to [Bendat and Piersol, 2011]. In the present study, most of the CFD post processing and acoustic calculations are performed frequency domain due to the computational easiness compared to time-domain. Two-point statistics are obtained from the post-processing of the CFD unsteady wall-pressure fluctuations. The raw pressure-time spatial history that is indicative of the unsteady turbulent flow is post-processed using k-ω code developed as a part of this work based on Spatial and time domain FFT techniques. Researchers like [Arguillat *et al.*, 2010, 2005], [Francois *et al.*, 2011] and [Gloerfelt and Berland, 2013] measured the unsteady wall-pressure fluctuations using wind tunnel experiments and post processed the raw data in case of flow over a flat plate with zero-pressure gradients. Other researchers like [Salze *et al.*, 2014] and [Salze *et al.*, 2015] have improved the experimental setup to measure wall-pressure data under pressure gradients

using linear antenna of microphones. They have presented wavenumber-frequency spectral results for pressure gradient flows. The coherence and wavenumber-frequency spectrum for Corcos model are plotted at fixed frequency in Figures 3.27(a), 3.27(b) and 3.27(c) as a benchmark for future comparisons. The k-ω code has been thoroughly validated using analytical Corcos model in Figure 3.27(d) and it's similar with that available in literature [Arguillat *et al.*, 2005]. More advanced methods like proper orthogonal decomposition POD [Druault *et al.*, 2013] have been adopted to separate the acoustic and aerodynamic component from TBL wall-pressure compared to the conventional Fourier techniques. For a very detailed review of the post processing methods adopted in CFD simulation and experiments, the reader is advised to look at [Millan and Riethmuller, 2003]. The post-processing of the CFD wall-pressure was implemented in MATLAB. The post-processing consists of three steps 1) reading the presssure-time data 2)Auto PSD and Cross-PSD analysis based on vectorised Welch 3) wavenumber-frequency spectrum analysis based on Spatial FFT. Vectorisation in MATLAB can be achieved using *reshape repmat* and *bsxfun*. FFT function in MATLAB is based on the FFTW software library. The PowerFLOW simulation generates the unsteady wall-pressure and stores in a netCDF binary format(.snc file extension). A very *important* note in extraction of real time wall-pressure from netCDF binary file is to convert the lattice pressure and other lattice units to real pressure in terms of pascal. This conversion from lattice units to mks units could be achieved by using PowerFLOW command line utilities *exaritool coord.ri* coupled with *exa_ meas_ copy* and *exafile*. A one-sided auto spectral density is obtained from the diagonal of the complex cross-spectral density matrix. Cross-spectral density matrix is obtained from the product of conjugate of discrete-time fourier transform of pressure and its transpose over each frequency. The complex coherence matrix is calculated as the ratio of complex cross-spectral density matrix and square root of the product of streamwise and spanwise auto spectral density matrix. A two dimensional spatial fourier transform of complex cross-spectral density matrix using the *FFT2* function gives a wavenumber-frequency spectrum. In an non-homogeneous flow, the wavenumber-frequency spectrum varies with spatial co-ordinates and it's separation distances along with frequency. Streamwise and spanwise wavenumber-frequency spectrum are calculated by averaging in spanwise and streamwise directions respectively. The final full form of wavenumber-frequency spectrum is obtained by spatial averaging in spanwise and streamwise direction with same indices. This spatially averaged full form of wavenumber-frequency spectrumfor is used in TBL power input calculations. The computational input data needed for k-ω code is presented below for flat fence and side mirror. In the flat fence case, the first 4 seconds out of 10 sec CFD run was skipped leaving behind a 6 second pressure-time history. This time history was

used to calculate the PSD and wavenumber-frequency spectrum. Incase of side mirror,the first 10 sec are skipped out of 17 seconds retaining the 7 second pressure-time history for post-processing.

Flat fence case: number of nodes in x-direction = 155, number of nodes in y-direction =124, time frames=48853, number of time windows=24, total nodes=19220, spatial mesh size in x-direction, dx=0.003 m, spatial mesh size in y-direction, dy=0.003 m, wavenumber mesh size in x-direction,dk_x=2.1645 $1/m$, wavenumber mesh size in y-direction,dk_y= 2.7100 $1/m$, sampling frequency = 8141.9 Hz, FFT window width = 2048, overlap percentage = 50%, time and spatial Window= Rectangular, frequency bandwidth = 3.975 Hz.

Side mirror case: number of nodes in x-direction = 132, number of nodes in y-direction =110, total nodes= 14520, time frames=152404, number of time windows=37, spatial mesh size in x-direction,dx=0.004 m, spatial mesh size in y-direction,dy=0.004 m, wavenumber mesh size in x-direction,dk_x=1.9084 $1/m$, wavenumber mesh size in y-direction, dk_y= 2.2936 $1/m$, sampling frequency = 21772 Hz, FFT window width = 4096, overlap percentage = 50% , time and spatial Window= Rectangular, frequency bandwidth = 5.3154 Hz.

A dB-map was plotted in Figures 3.28 for flat fence and side mirror case. A dB-map is nothing but a spatial distribution of Auto PSD over the plate at fixed frequency. As expected the dB-map for fence case is almost constant value with not much variation across the plate as seen in Figure 3.28(a) but for side mirror case the vortex shedding phenomenon is clearly visible in Figure 3.28(b) with high dB values located just after the mirror location.The vortex shedding frequency of 65 Hz matches well with experiments.

In Figures 3.29(a) and 3.29(c), the coherence contours are plotted showing the size of influence zones with respect to a reference probe at centre of the plate. The influence zone is much larger in the mirror case than the fence case due to presence of strong pressure gradients in mirror case. The corresponding coherence plot with respect to probe spacing show the decay rates in Figures 3.29(b) and 3.29(d). These coherence plots have been used for identification of empirical model parameters and also help to check for homogeneity of flow. As a future prospect in FE analysis of TBL flow, the joint acceptance can evaluated as the sum of joint acceptance in these influence zones instead of a full plate calculation to reduce the cost of computation. One might note that the influence zone are close to elliptical in shape with the major axis of ellipse inline with flow direction.

The streamwise CFD wall-pressure coherence was validated with experiments in separated and reattached regions for mirror case shown in Figures 3.30(a) and 3.30(b). The coherence in reattached region shows an excellent agreement with experiments in Figure 3.30(b) and

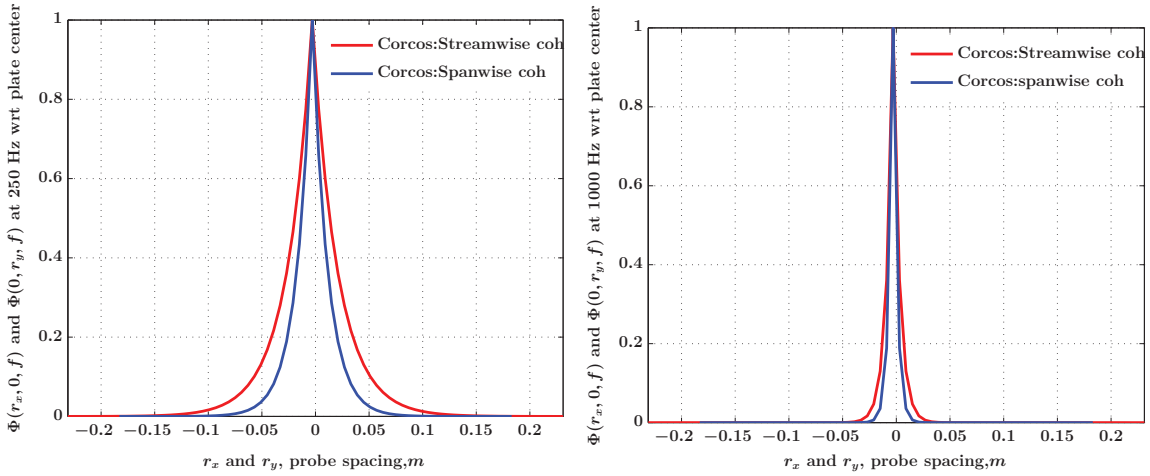

(a) Coherence for Corcos analytical model at 250 Hz

(b) Coherence for Corcos analytical model at 1000 Hz

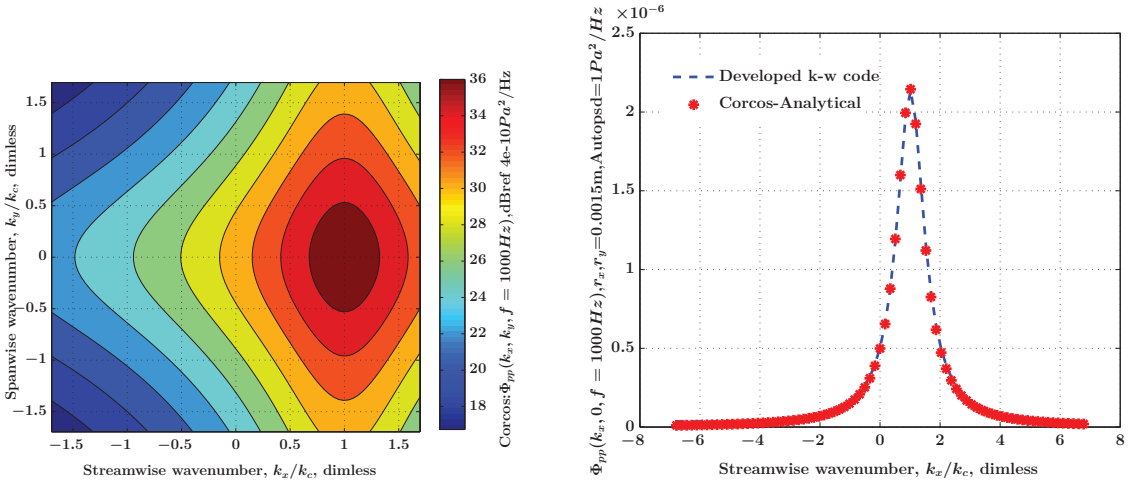

(c) kx and ky spectrum for Corcos analytical model at 1000 Hz

(d) Validation of k-ω code with Corcos kx-w Analytical Model at 1000 Hz

Figure 3.27 Validation of k-ω code with Corcos analytical model

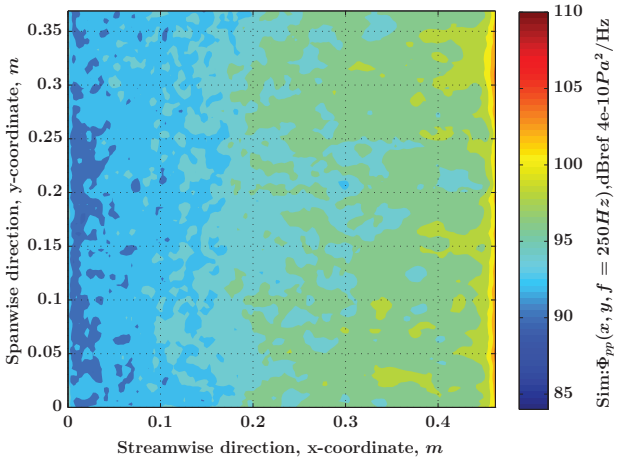

(a) dB Maps at constant frequency on the plate for fence case using k-ω code

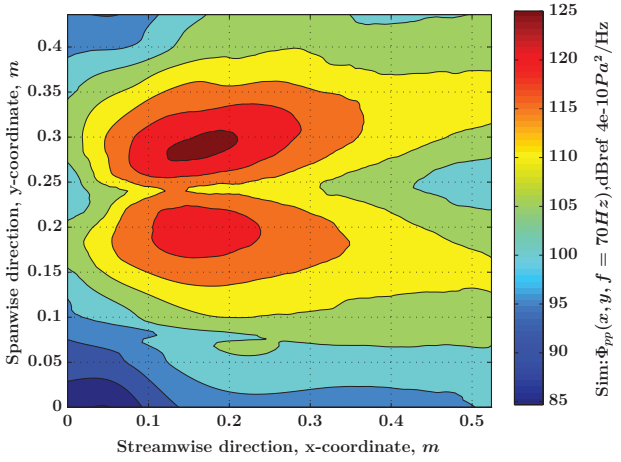

(b) dB Maps at vortex shedding frequency on the plate for mirror case using k-ω code

Figure 3.28 dB maps at constant frequency using k-ω code

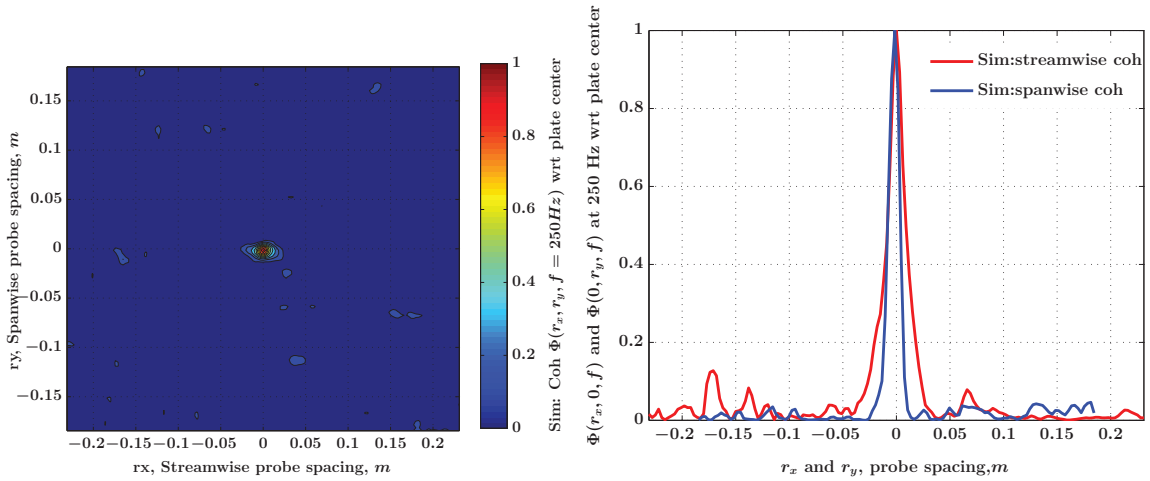

(a) Coherence influence zone on the plate for fence case

(b) Coherence correlation length on the plate for fence case

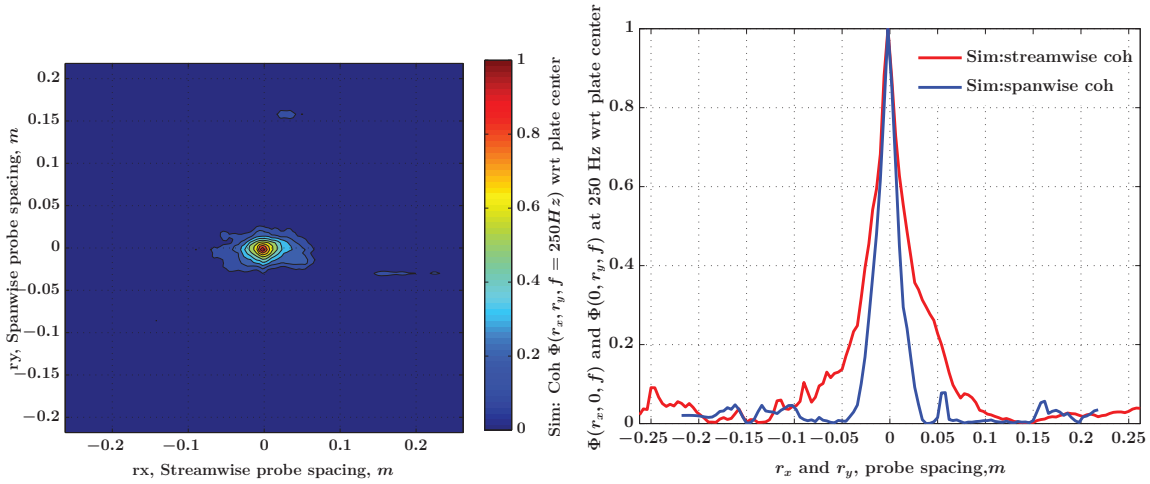

(c) Coherence influence zone on the plate for mirror case

(d) Coherence correlation length on the plate for mirror case

Figure 3.29 Size of coherence influence zone with respect to plate center

a close range match in separated region with decay captured well. For a homogeneous flow, the coherence should be indifferent from the location of probes rather it should be function of probe separation distance. In the check for homogeneity of flow, the coherence computed with same probe spacings. It was then compared with respect the different probes in the center line of the plate as shown in Figure 3.30(c). There exists no homogeneity in the mirror flow as the coherence with same probe spacing varies strongly across the centreline of plate.

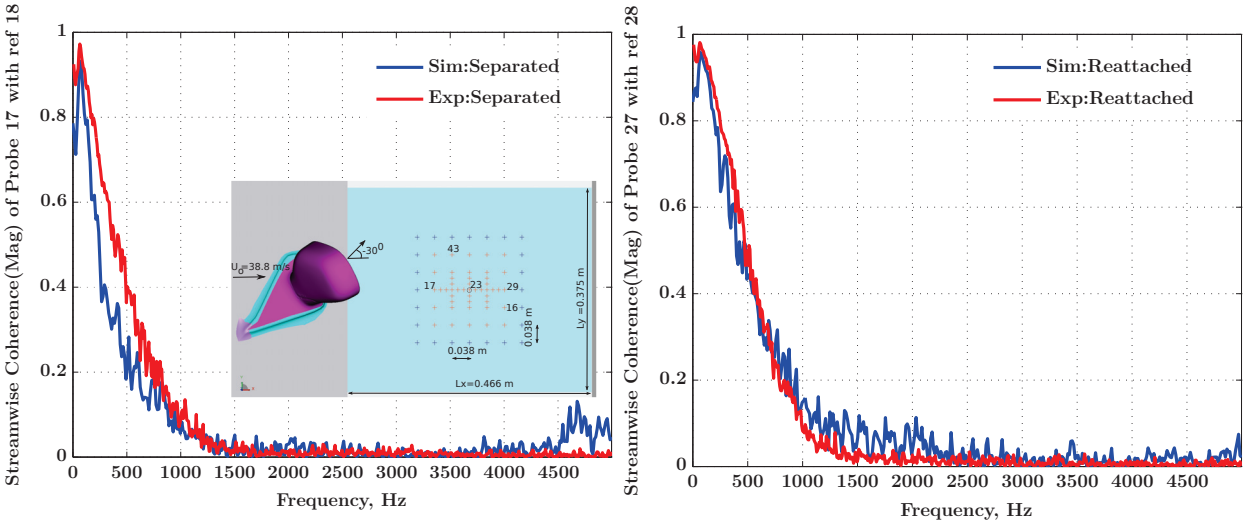

(a) Validation of coherence in separated region

(b) Validation of coherence in reattached region

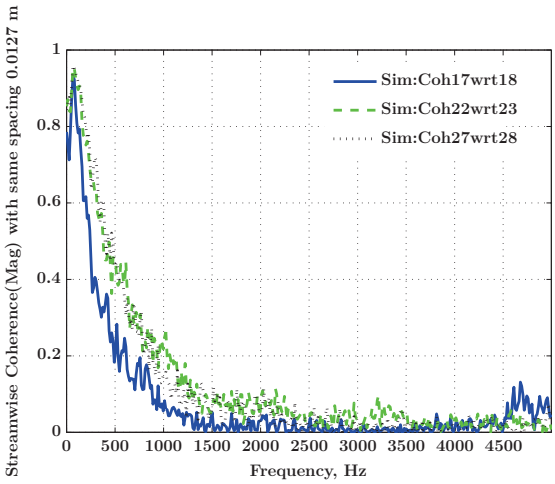

(c) Homogeneity test with same probe spacing in streamwise direction

Figure 3.30 Validation of the wall-pressure streamwise coherence with experiments for the side mirror

The k-ω contour spectrum at fixed frequency for flat fence in Figure 3.31(a) resembles the elliptical shape [Mellen, 1990] and for side mirror resembles the rhombic shape as

shown in Figure 3.31(c). In comparison with wavenumber-frequency spectrum results available in literature, the acoustic zones are identified clearly in streamwise wavenumber frequency spectrum along with convective ridge in Figures 3.31(b) and 3.31(d). This an encouragement that a finely resolved unsteady CFD with a lengthy run helps to achieve a better higher order statistics very much needed for aero-acoustic calculations.

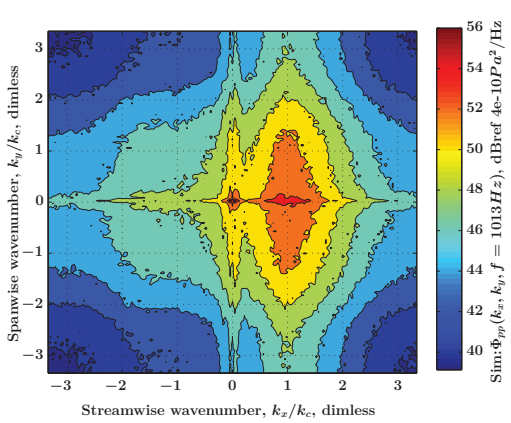

(a) k-w convection and acoustic zone on the plate for fence case using k-w code

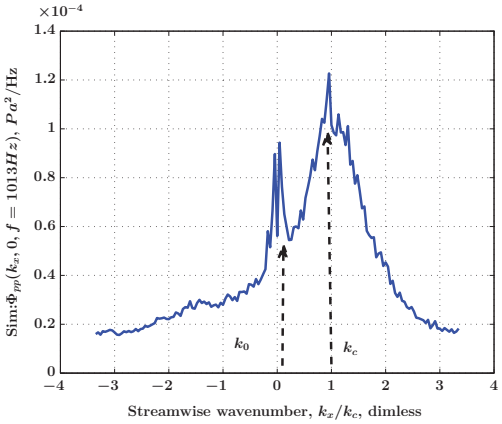

(b) single slice of k-w convection and acoustic zone on the plate for fence case using k-w code

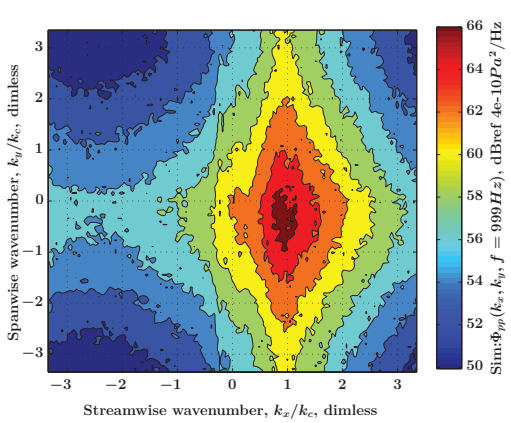

(c) k-w convection and acoustic zone on the plate for mirror case using k-w code

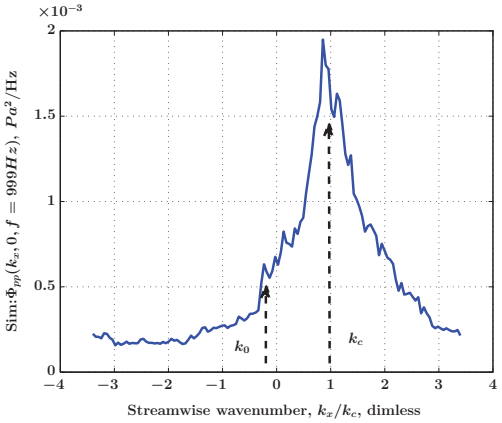

(d) single slice of k-w convection and acoustic zone on the plate for mirror case using k-w code

Figure 3.31 Two dimensional wavenumber-frequency spectrum plots at fixed frequency

Another level of validation of k-ω code is presented at wavenumber stage. In the mirror case, the CFD streamwise wavenumber-frequency spectrum plotted in Figure 3.32(b) compares well with that of experiments(Figure 3.32(a)). The vortex shedding frequency and convective contour zone are cleary visible in Figure 3.32.

Even more striking, the streamwise wavenumber spectrum over the entire plate shown in Figures 3.33(a) and 3.33(b) clearly shows three characteristic directions that can be

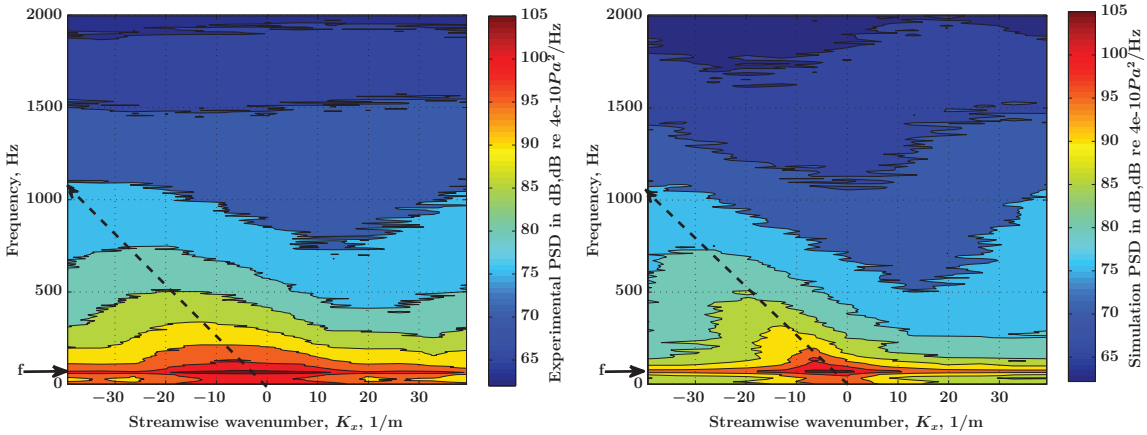

(a) Experiment:streamwise wavenumber frequency PSD for mirror case

(b) Simulation:streamwise wavenumber frequency PSD for mirror case

Figure 3.32 Validation of streamwise wavenumber frequency PSD of probes 17-29 for mirror case

identified as the convective ridge with a convection velocity Uc = 25 m/s and the acoustic cone. The simulation is therefore able to capture both convection and acoustic contributions to the surface pressure fluctuations, which was not evidenced in the Purdue experiment [Park *et al.*, 2004] but was observed by [Arguillat *et al.*, 2010] in their most recent resolved wall-pressure measurements. The spanwise frequency wavenumber spectrum for the side mirror case in Figure 3.34(b), is no longer symmetric compared to the flat fence in Figure 3.34(a). This is caused by some lateral convection caused by the side mirror yaw angle of $-30°$ with respect to the flow direction.

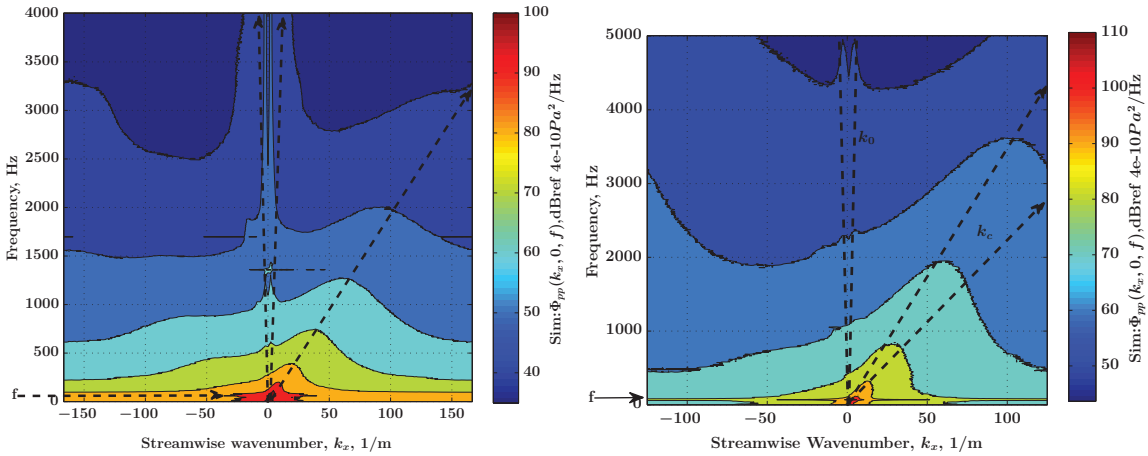

(a) Streamwise frequency wave number spectrum for the flat fence

(b) Streamwise frequency wave number spectrum for the side mirror

Figure 3.33 Streamwise k-ω spectrum for fence and mirror cases

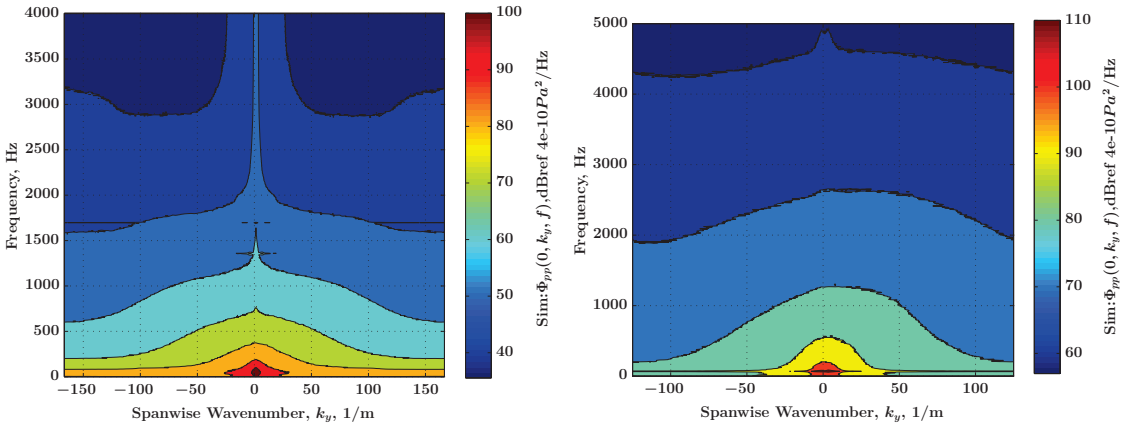

(a) Spanwise frequency wave number spectrum for the flat fence

(b) Spanwise frequency wave number spectrum for the side mirror

Figure 3.34 Spanwise k-ω spectrum for fence and mirror cases

3.4.5 Spatial variation of wavenumber-frequency spectrum for side mirror

The k-ω code has been used to study the non-stationarity and non-homogenity of the side mirror flow by computing the wavenumber spectrum at different locations on the plate removing the assumption of homogenity. In a non-homogeneous condition, the wavenumber-frequency spectrum is function of spatial co-ordinates, wavenumbers in each direction and frequency. In a homogeneous the wavenumber-frequency spectrum becomes spatial indifferent and only function of wavenumbers and frequency. The probe setup to calculate the spatial variation of wavenumber spectrum is shown in Figure 3.35.

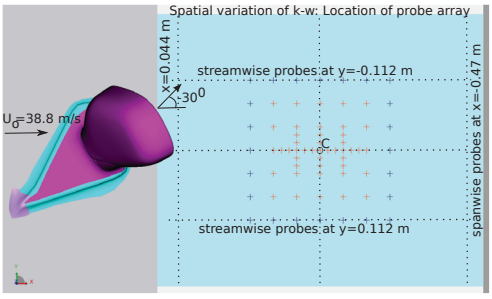

Figure 3.35 Location of probe array for non-homogeneous k-ω spectrum

The streamwise wavenumber-frequency spectrum was obtained with a set of symmetrically spaced streamwise probes in spanwise direction as shown in Figures 3.36(a), 3.36(b) and 3.36(c). Similarly spanwise wavenumber-frequency spectrum was obtained with a set of symmetrically spaced spanwise probes in streamwise direction as shown in Figures 3.36(d), 3.36(f) and 3.36(f). These set of wavenumber spectrum could be used for computing the TBL power input for highly non-homogenous flows and could also be used

to find the local convection velocity variation over the plate. It is confirmed that the mirror flow is not symmetric around spanwise direction and also non-homogenous as the equidistant wavenumber spectrums do not match with each other.

3.5 TBL model parameter identification from CFD WPF

In this section, empirical TBL model parameters are identified from the CFD wall pressure coherence and cross spectrum. Many researchers [Arguillat *et al.*, 2010; Coney *et al.*, 1999; Dejong *et al.*, 2001; Park *et al.*, 2004], have used wind tunnel measurements to estimate the empirical constants for the TBL model by data regression. Corcos model is the most widely used empirical model for describing the wall pressure fluctuations due to its analytical simplicity and its ability to describe the coherence decay functions in both streamwise and spanwise directions appropriately. Yet a simple regression for the entire domain is only realistic in academic cases studying homogeneous wall-pressure fields. As emphasized above in Section 3.3, non-equilibrium turbulent boundary layers with strong inhomogeneity are developing in both the flat fence and the side-mirror cases. Recently, [Pérot *et al.*, 2009] have simulated the turbulent flow over a full sedan vehicle with two yaw angles and computed the wall pressure signals on the side glasses over a short period of time because of the complexity of the full vehicle model and the cost of the simulations. They evaluated the parameters Corcos model locally in more or less homogeneous flow regions. In the present work, the same strategy is used to identify Corcos model parameters for the flat fence and side mirror cases using again the simulated wall pressure coherence but this time over a much longer time to improve the accuracy of the data regression of the coherence magnitude and cross spectral phase. Curve fitting methodology used to determine the empirical model parameters is described below.

3.5.1 Identification of convection ratio and coherence decay

Identification procedure for Corcos model parameters is described as follows. In Corcos model, the TBL wall pressure cross spectrum

$G_p\left(r_x, r_y, \omega\right)$ consists of a power spectrum $S_{pp}\left(\omega\right)$ and a coherence $\psi\left(r_x, r_y, \omega\right)$ where

$$G_p\left(r_x, r_y, \omega\right) = S_{pp}\left(\omega\right)\psi\left(r_x, r_y, \omega\right) \tag{3.1}$$

After incorporating the exponential decaying coherence functions, the cross spectrum becomes

$$G_p\left(r_x, r_y, \omega\right) = S_{pp}\left(\omega\right) e^{-\alpha_x \frac{|\omega r_x|}{U_c}} e^{-\alpha_y \frac{|\omega r_y|}{U_c}} e^{-i\frac{\omega r_x}{U_c}} \tag{3.2}$$

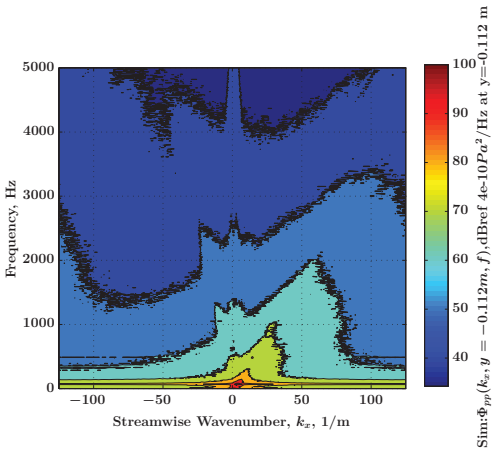

(a) Streamwise frequency wave number spectrum at y=-0.112m

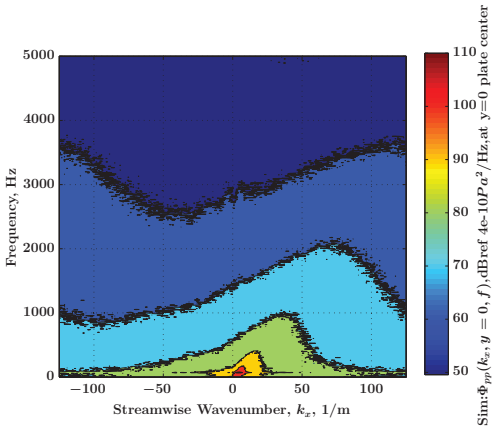

(b) Streamwise frequency wave number spectrum at y=0 m

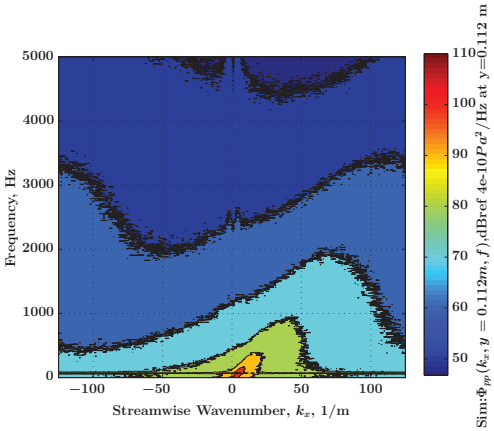

(c) Streamwise frequency wave number spectrum at y=0.112m

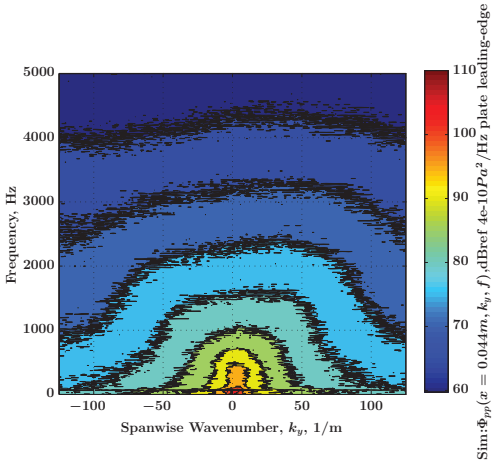

(d) Spanwise frequency wave number spectrum at x=0.044 m

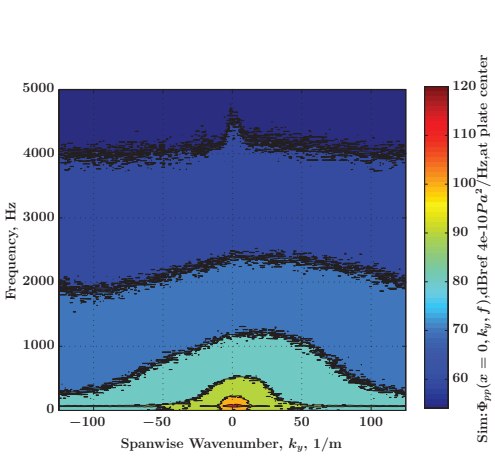

(e) Spanwise frequency wave number spectrum at x=0 m

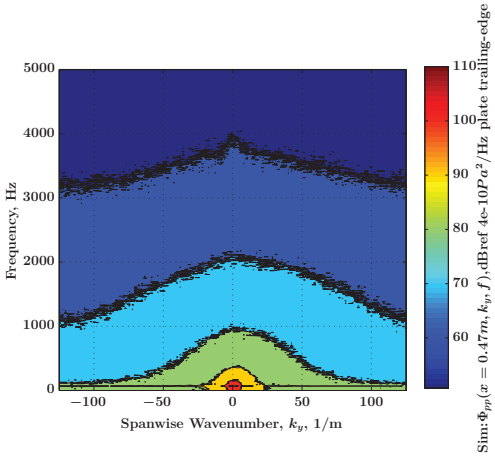

(f) Spanwise frequency wave number spectrum at x=0.47 m

Figure 3.36 Spatial variation of streamwise and spanwise k-ω spectrum for mirror case

Now coherence can be written as

$$\psi(r_x, r_y, \omega) = \frac{G_p(r_x, r_y, \omega)}{\sqrt{S_{ppx}(\omega) S_{ppy}(\omega)}} = e^{-\alpha_x \frac{|\omega r_x|}{U_c}} e^{-\alpha_y \frac{|\omega r_y|}{U_c}} e^{-i \frac{\omega r_x}{U_c}} \tag{3.3}$$

Complex coherence between two probe locations was calculated from CFD wall pressure and the cutoff frequency $f_{cut} = \frac{0.65 \times U_c}{n \times r_x}$ is determined based on the spacing of probes r_x, convection velocity U_c and n is number of probes required to resolve the convection lengths. The cutoff frequency is calculated based on values of n varying between 2 and 6. Once the streamwise coherence between two probes is known, the streamwise decay coefficients can be determined once the convection velocity U_c is obtained. Similarly, the spanwise decay coefficient can be determined from the spanwise coherence magnitude. The convection velocity of the flow is identified from the phase information of the cross spectrum or complex coherence in the streamwise direction as shown in Equation (3.4)

$$Phase = \gamma(\omega, r_x) = \left| \frac{\omega\ r_x}{U_c} \right| \tag{3.4}$$

The phase is unwrapped from the interval of $[0; 2\pi]$ to the interval $[0; \infty]$ and a linear interpolation of phase with respect to the circular frequency was done to identify U_c

$$U_c = \frac{\omega r_x}{\gamma(\omega, r_x)} \tag{3.5}$$

After the estimation of the convection velocity, the Corcos decay coefficients are identified in each direction separately using linear curve fit of logarithm of modulus of coherence or a non-linear (exponential) curve fit for coherence in each direction. The coherence in streamwise direction is

$$\psi(r_x, 0, \omega) = \frac{G_p(r_x, 0, \omega)}{\sqrt{S_{ppx}(\omega)\, S_{ppy}(Y, \omega)}} = e^{-\alpha_x \frac{|\omega r_x|}{U_c}} e^{-i \frac{\omega r_x}{U_c}} \tag{3.6}$$

Linear curve fitting of the logarithm of the modulus of the coherence, gives the Corcos decay coefficient in the streamwise direction

$$\alpha_x = -\ln |\psi(r_x, 0, \omega)| \frac{U_c}{|\omega\ r_x|} \tag{3.7}$$

Similarly, the Corcos decay coefficient for the spanwise direction is given by

$$\alpha_y = -\ln|\psi(0, r_y, \omega)| \frac{U_c}{|\omega\, r_y|} \tag{3.8}$$

The first step in the identification of Corcos model parameters would be to find the convection ratio and then the decay parameters can be identified from each homogeneous zone decided by the flow structure and its reattachment. From the Figures 3.37(a) and 3.37(b), the convection ratio for fence is 0.5 and 0.65 for mirror. The convection ratio varies with frequency and indifferent from probe spacing.

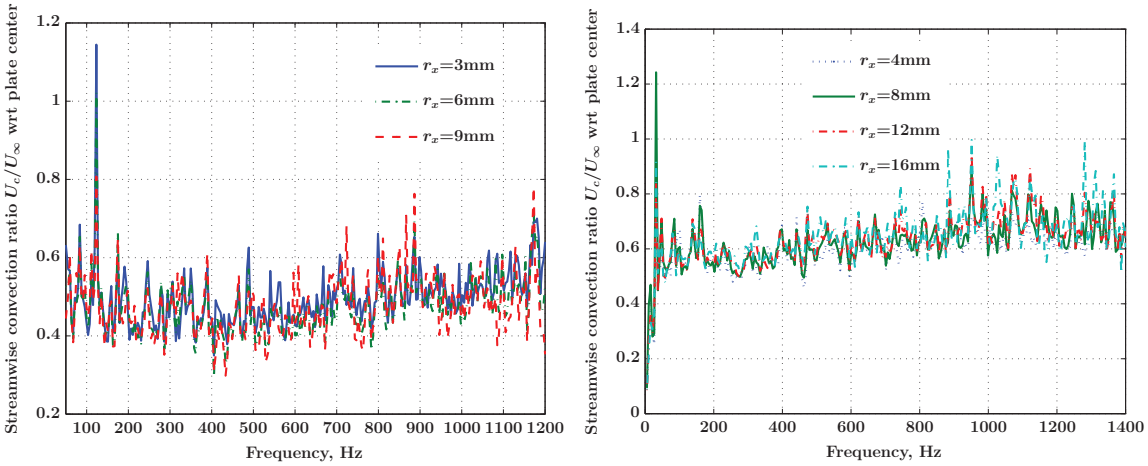

(a) Convection velocity ratio from Unwrapped Phase of Complex coherence for flat fence

(b) Convection velocity ratio from Unwrapped Phase of Complex coherence for mirror

Figure 3.37 Convection ratio for flat fence and side mirror

3.5.2 Identification of homogeneous zone based on flow reattachent and dB map

As the Corcos model assumes a homogeneous flow conditions, the identification of those parameters also have to conducted homogeneous zone to get a better estimates. Based on the position of flow reattachment, an appropriate placement of probes can be determined to identify the Corcos model parameters. This identification process could be done after the reattachment zone in quasi-homogeneous zone. The flow structure parameters like the reattachment zone and isosurface contour based on lamda2 criterion are presented for fence and mirror in Figure 3.38. In identification of Corcos parameters for the fence case, locations close to the trailing edge and away from reattachment have been used.

For each test case, the plate behind the obstacle is divided into homogeneous zones where Corcos model estimation is adequate. Wall pressure PSD and skin frictions were taken as

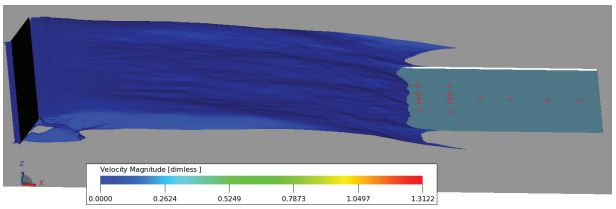

(a) Fence:reattachment

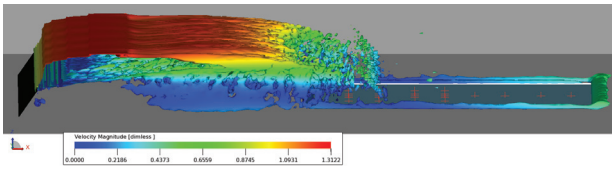

(b) Fence:isosurface lamd2 at -0.01

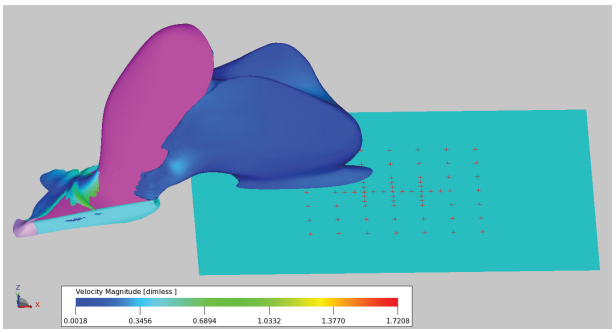

(c) Mirror:reattachment

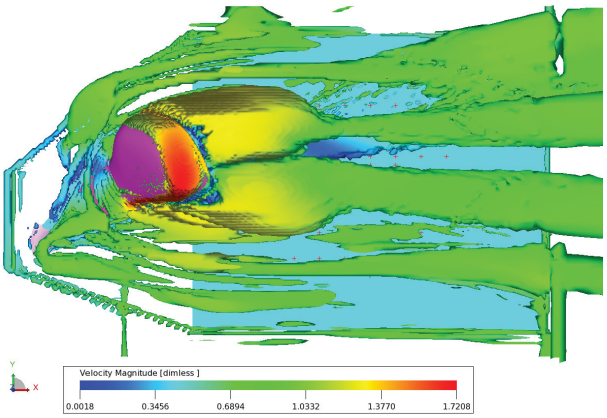

(d) Mirror::isosurface lamda2 criterion

Figure 3.38 Reattachment iso-surface at lamda2 = -0.01 for fence and side mirror

criteria to identify the flow gradients. Figures 3.39(a) and 3.39(b) show the homogeneous zones based on the wall-pressure autospectrum for the flat fence and the side mirror respectively.

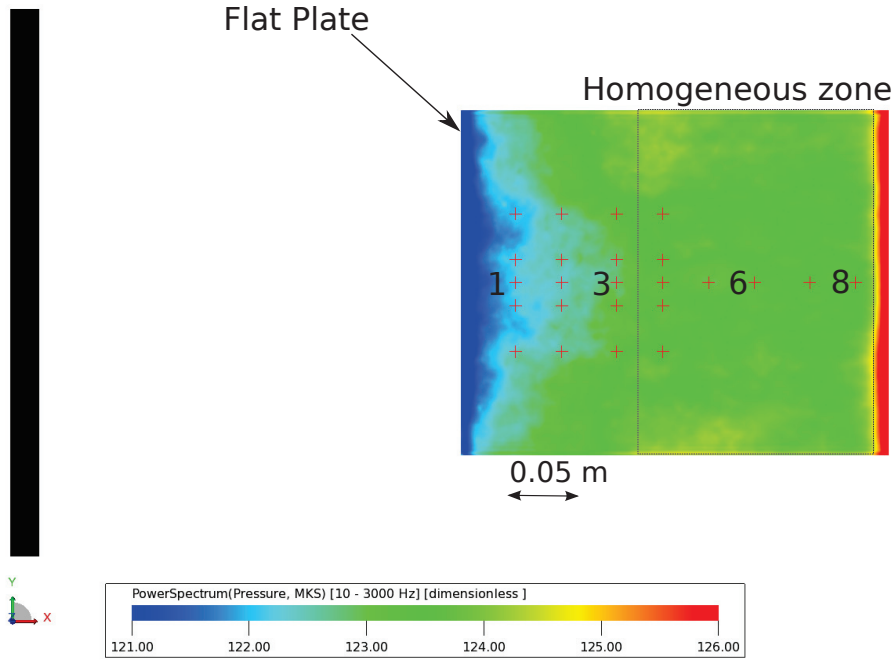

(a) Flat fence. Pressure auto spectrum on the plate in the frequency band 10-2000 Hz

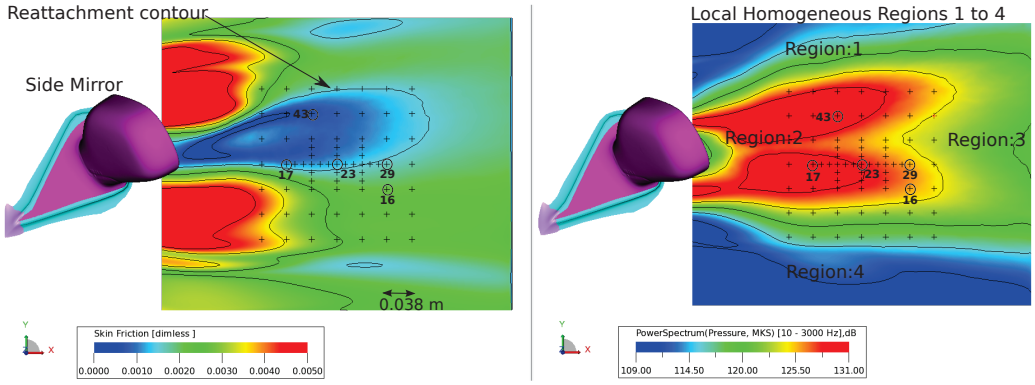

(b) Side-mirror. Mean skin friction on the plate (left) Pressure auto spectrum on the plate in the frequency band 10-2000 Hz (right)

Figure 3.39 Homogeneous zones based on autospectrum and mean skin friction

For the side mirror, the mean skin friction that clearly highlights the separated region is also shown in Figure 3.39(b). After studying the different regions of influence in the flow with a fixed reference probe for each zone, the size of homogeneous zone need to be specified. In the flat fence case as shown in Figure 3.39(a) there was not much variation in the autospectum of the wall pressure in the attached zone; hence this entire zone was

selected for the estimation of Corcos parameters. In the side mirror case however, as shown in Figure 3.39(b) the plate is subdivided into four regions based on the strong variation of pressure fluctuations and the flow reattachment contour. These four regions can be named as 1) the shear zone that consists of the two side mirror shear layers on either side of the mirror 2) the separated zone (vortex zone) where the highest autospectrum is observed and that is the major source of plate excitation 3) the reattachment zone, where the flow fully attaches to the plate and finally 4) the tail wake zone caused by the tail end portion of the side mirror, which is the quietest zone among all zones.

3.5.3 Empirical TBL parameter identification for the flat fence

In the flat fence case, complex coherence was calculated from the CFD wall pressure coherence in the homogeneous zones located earlier Figure 3.39(a). The homogeneity checks were conducted by comparing the coherence with the same probe spacing and different reference probes before curve fitting. Typical curve fitting results for phase of cross spectrum and coherence magnitude for a particular reference probe are shown in Figures 3.40. Homogenetiy checks were performed in streamwise and spanwise as shown in Figures 3.40(a) and 3.40(b). In the streamwise direction, five probes per convection wavelength are used to calculate the cutoff coherence. The minimum probe spacing that was used is 1.5 mm to have the best cutoff coherence magnitude and phase. In both fence and side mirror, the curve fitting procedure was based on a least square minimization and the nonlinear (exponential fit) regression. Nonlinear (exponential) regression provides a better fit of the coherence magnitude compared to the linear fit. In the spanwise direction, the empirical identification of Corcos parameters used five probes per convection wavelength. As the spanwise decay rates are much faster than the streamwise direction consistently with Corcos analytical model, a higher number of probes per convection wavelength was used to resolve the spanwise coherence scales. The spanwise decay parameter was estimated till the cutoff coherence with Equation (3.8) using both nonlinear curve fitting shown in Figure 3.40(f). The cutoff coherence was calculated based on the probe spacing and convection velocity as described in Section 3.5.1. The summary of the identification process for the flat fence case is shown in Table 3.2. Good agreement is found with experimental values obtained from Purdue university wind tunnel on a similar test up described in Section 3.2.1. There is an excellent match between the estimated convection velocity and decay coefficients with experimental values.

3.5.4 Empirical TBL parameter identification for side mirror

In the side mirror case, the empirical identification of TBL parameters for the attached region3 (as shown in Figures 3.41) is presented. Similar procedure was adopted for empirical

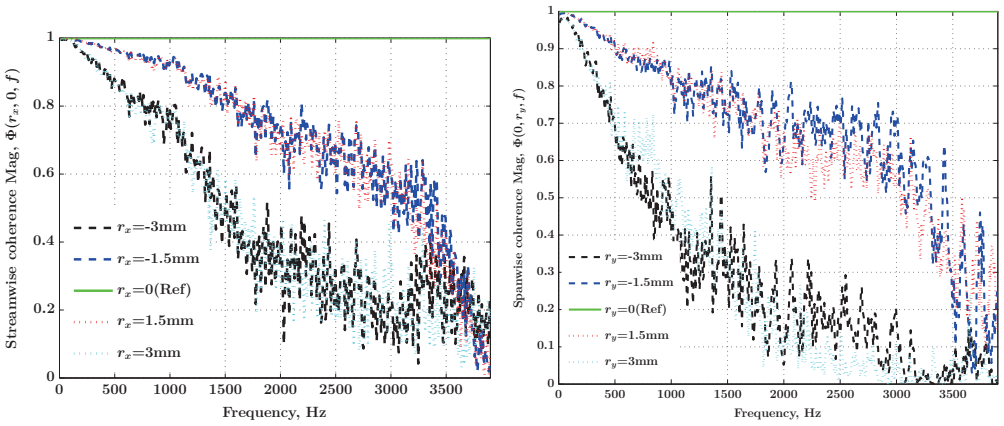

(a) Ref: probe 7 homogeneity verification based on coherence with same probe spacing

(b) Ref: probe 6d homogeneity verification based on coherence with same probe spacing

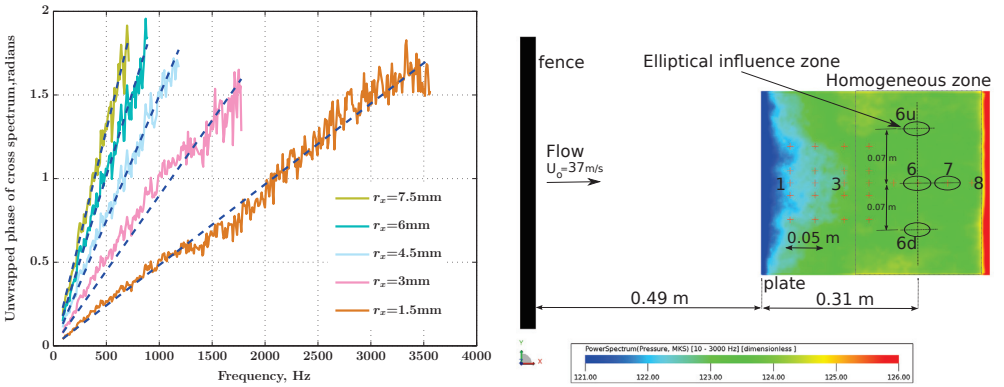

(c) Ref probe 7 :linear fit for the unwrapped phase of cross spectrum with various probe spacing

(d) Fence: schematic of reference probe locations for estimation of coherence mag and phase

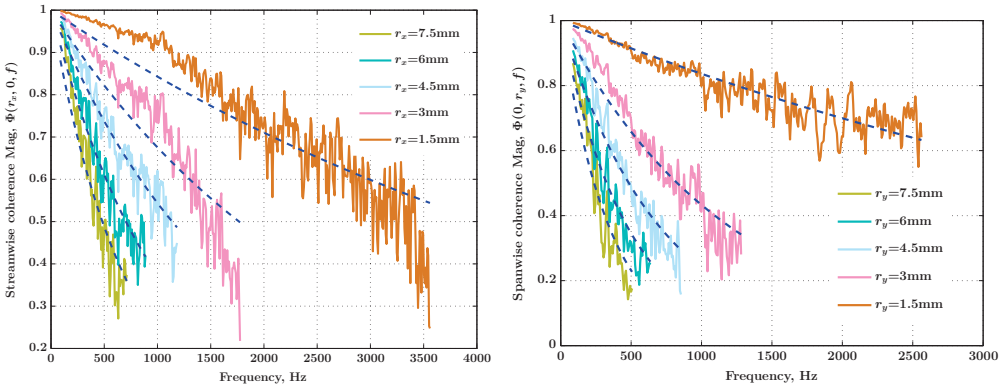

(e) Ref: probe 7 curve fitting for the streamwise coherence magnitude with various probe spacing

(f) Ref: probe 6d :curve fitting for spanwise coherence magnitude for with various probe spacing

Figure 3.40 CFD WPF coherence curve fitting in streawise and spanwise for fence: Ref probe 7 and probe 6d

	Attached zone(Mean Values)	U_c/U_∞	α_x	α_y
Simulation		0.52	0.51	0.98
Experiment ([Park *et al.*, 2004])		0.5	0.5	0.9

Table 3.2 Flat fence: Corcos parameters obtained from nonlinear curve fitting

identification of the remaining three zones. The homogeneity checks were conducted in each zone by comparing the coherence with same probe spacing and different reference probes before curve fitting procedure. Complex coherence was calculated from the CFD wall pressure coherence in the four homogeneous zones as discussed in Section 3.5.2. Typical curve fitting results for the phase of the cross spectrum and the coherence magnitude for a particular reference probe is shown in Figures 3.41(c), 3.41(e) and 3.41(f). In the streamwise direction, two probes per convection wavelength are used to calculate the cutoff coherence. The minimum probe spacing that was available is 2 mm on the plate. Nonlinear fit (exponential) were used to estimate the decay coefficients and linear fit for the unwrapped phase of the cross spectrum in the streamwise direction. Streamwise decay coefficients are presented for all four zones in Table 3.4. In the spanwise direction, the empirical identification of Corcos parameters used two probes per convection wavelength only, as there was sufficient decay and the flow was homogeneous in each zone. The spanwise decay parameter was estimated till the cutoff coherence with Equation 3.8 using the nonlinear curve fitting shown in Figure 3.41(f). The cutoff coherence was calculated based on the probe spacing and convection velocity as described in Section 3.5.1. The summary of Corcos parameters for the various zones is shown in Table 3.4. A few set of streamwise coherence measurements were done at Purdue wind tunnel for few probe locations namely probe 27 with respect to 28. Corcos parameters derived from CFD Coherence were validated for this set of probes with experimental values as presented Table 3.3. The present parameters compare well with experimental values from Purdue and also for half-cylinder bluff body presented by [Arguillat *et al.*, 2010] for similar flow speed. There is an slight mismatch between the estimated convection velocity and decay coefficients with Arguillat for the separated zone as these experimental coefficients were not obtained zone by zone. In all the flow zones, the convection velocity ratio falls in the typical experimental range of 0.5 to 0.7. Corcos decay coefficients are higher in the shear zone when compared to the attached and separated zones since the side mirror is yawed at an angle of $-30°$ with respect to the flow direction, and most of the flow energy is concentrated in the separated and attached zones. Because of the mirror $-30°$ yaw

angle, there was no convection noticed in the tail zone (quiet zone), hence negligible decay coefficients are obtained in this zone.

Separated zone(Mean Values)	U_c/U_∞	α_x
Experiment	0.71	0.53
Simulation	0.68	0.51

Table 3.3 Validation of coherence decay and convection ratio with experimental data for side mirror for Probe 27 wrt 28

	Mean Values for various zones	(U_c/U_∞)	α_x	α_y
Region1 Shear zone		0.52	1.7	1.79
Region2 Separated zone		0.58	0.93	1.36
Region3 Attached zone		0.66	0.35	1.14
Region4 Tail wake zone		No convection	0.03	0.04
Experiments on Half-Cylinder, Arguillat 2005-2855		0.79	0.13	1.32

Table 3.4 Side-mirror: Corcos parameters obtained from nonlinear curve fitting

3.6 Expressions for vibroacoustics indicators for plate excited by TBL

Mathematical expressions for vibroacoustic indicators for a plate-cavity system are presented in a) Modal Approach b) Band averaged values(SEA) c)Modal/FE approach. In the derivation of following expressions, the rectangular plate is assumed to be simply supported and analytical modeshapes are considered. Coupling between plate modeshapes and cavity modeshapes is neglected. Fluid-structure interaction (fluid loading) is also neglected. Rotational interia is neglected (thin plate theory). Flow Mach number is subsonic. The problem of aero-acoustics and vibro-acoustics are decoupled. It has to be noted that SEA assumptions like the plate modes are highly resonant and sufficient modes in each band are assumed to be present and no modal overlap exists. Coupling between the plate modeshapes is assumed to be weak due to light damping of plate. The plate excited by TBL is assumed to be radiating into free-field by treating the cavity with anechoic foam wedges in the experiments. TBL excitation is assumed to be homogeneous and stationary. The mathematical expressions for vibro-acoustic indicators for simply supported plate

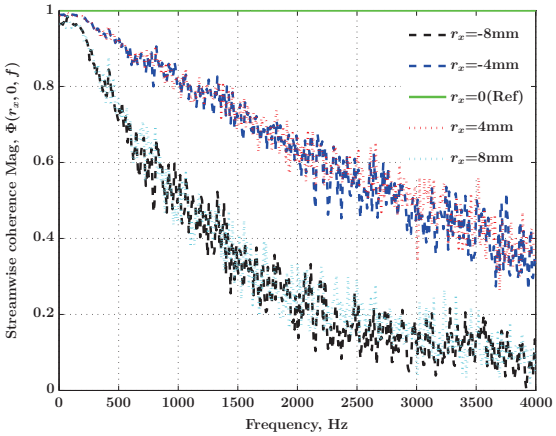

(a) Region 3 :Homogeneity verification based on streamwise coherence with same probe spacing

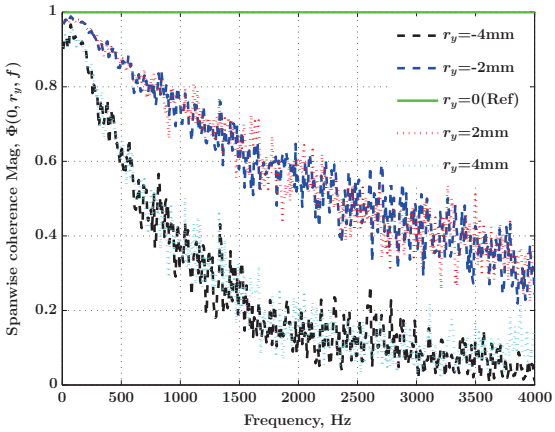

(b) Region 3 :Homogeneity verification based on spanwise coherence with same probe spacing

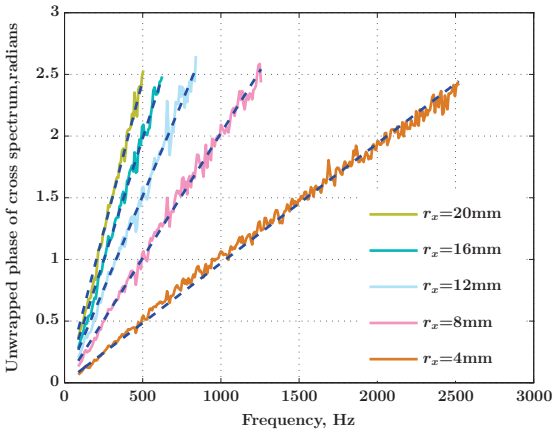

(c) Region 3 :Linear fit for the unwrapped phase of streamwise cross spectrum with various probe spacing

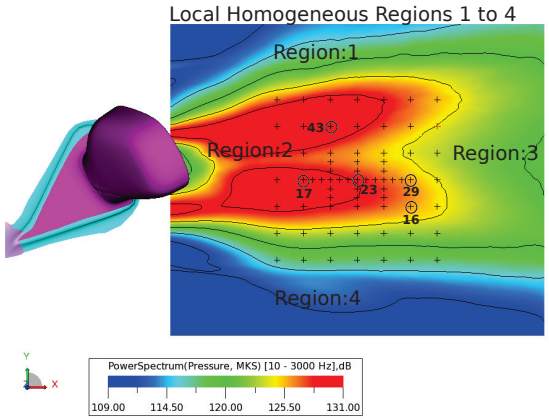

(d) Location of region3: Attached zone

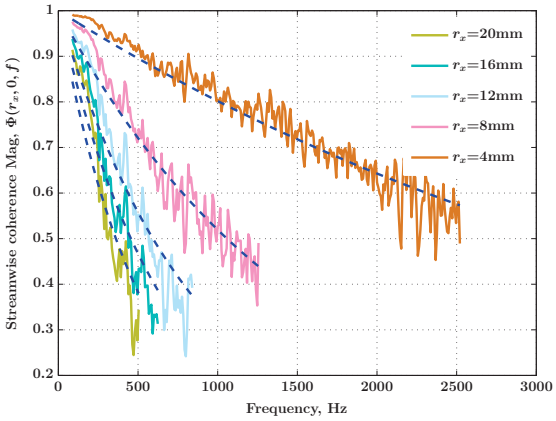

(e) Region 3 :Curve fitting for the streamwise coherence magnitude with various probe spacing

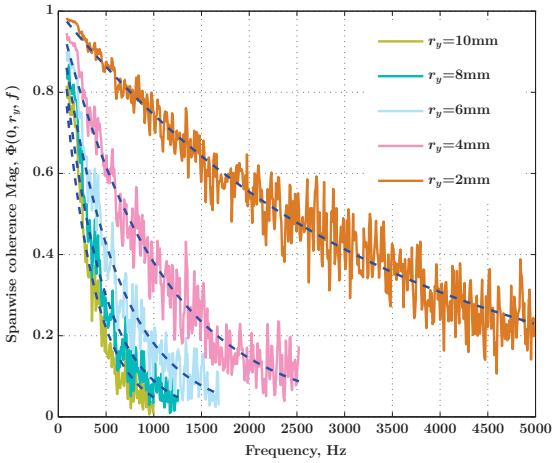

(f) Region 3 :Curve fitting for the spanwise coherence magnitude with various probe spacing

Figure 3.41 CFD WPF coherence curve fitting in streamwise and spanwise for region 3 of side mirror

excited by TBL is provided below. For a detailed derivation of these expressions, the reader is advisable to refer books like [Atalla and Sgard, 2015] and [Petyt, 1990].

Modal approach

Power input is given by

$$P_{in} = \frac{S_{pp}(\omega)}{8} \sum_{mn} A^2(\omega_{mn}) \eta_{mn} M) \frac{\omega_{mn}^2 j_{mn}^2}{M_{mn}^2 |Y_{mn}^2|} \tag{3.9}$$

Quadratic velocity is given by

$$\langle V^2 \rangle = S_{pp} \frac{\omega^2 A^2}{8} \sum_{mn} \frac{j_{mn}^2(\omega)}{M_{mn}^2 |Y_{mn}^2|} \tag{3.10}$$

Power radiated in the free-field

$$P_{rad} = -\omega^2 \sum_{mn} \frac{Re(Z_{rad,mn}) j_{mn}^2}{M_{mn}^2 |Y_{mn}^2|} \tag{3.11}$$

where the modal impedance of plate $Y_{mn} = -\omega^2 + \omega_{mn}^2(1 + j\eta_{mn})$ and modal mass for simply supported plate $M_{mn} = \frac{M}{4} = \frac{\rho_s h A}{4}$

Real part of $Z_{rad,mn}$ is the plate radiation resistance.

The coupling efficiency between the TBL excitation and plate modeshapes is given by Joint-acceptance. The joint acceptance in spatial domain is given by

$$j_{mn}^2(\omega) = \frac{1}{A^2} \int_A \int_A \phi_{mn}(x, y) \psi(x, y, x, y', \omega) \phi_{mn}(x', y') dx dy dx' dy' \tag{3.12}$$

and in wavenumber domain is given by

$$j_{mn}^2(\omega) = \frac{1}{2\pi A^2} \int_0^\infty \int_0^\infty \left| \phi_{mn}(k_x, k_y, \omega)^2 \right| \psi(k_x, k_y, \omega) dk_x dk_y \tag{3.13}$$

Band averaged values (SEA) Approach

Frequency band averaged vibro-acoustic indicators for SEA(resonant contributions). In TBL excitation, the plate response does not have non-resonant contributions unlike the diffuse field excitation. A detailed theory behind the SEA modeling of plate-cavity system is available in [Norton and Karczub, 2003] and [Lyon, 2014].

Band averaged power input spectral density is given by

$$\langle P_{in} \rangle_{\triangle\omega} = S_{pp} \frac{\pi A^2}{2M} n(\omega) \langle j_{mn}^2 \rangle_{\triangle\omega} \tag{3.14}$$

Band averaged velocity spectral density is given by

$$\langle V^2 \rangle_{\triangle\omega} = S_{pp} \frac{\pi A^2}{2M^2} \frac{n(\omega)}{\omega} \frac{\langle j_{mn}^2 \rangle_{\triangle\omega}}{\langle \eta_{mn} \rangle_{\triangle\omega}} = \frac{\langle P_{in} \rangle_{\triangle\omega}}{\omega \langle \eta_{mn} \rangle_{\triangle\omega}} M \tag{3.15}$$

Band averaged joint acceptance and damping loss factor is given by

$$\langle j_{mn}^2 \rangle_{\triangle\omega} = \frac{1}{N} \sum_{mn=1}^{N} j_{mn}^2(\omega) \tag{3.16}$$

$$\langle \eta_{mn} \rangle_{\triangle\omega} = \frac{1}{N} \sum_{mn=1}^{N} \eta_{mn} \tag{3.17}$$

where N are the resonant modes in each band of interest.

In SEA modeling, the coupling loss factor between plate(1) and cavity(2) is proportional to plate radiation efficiency $\sigma(\omega)$ and its given by

$$\eta_{12} = \frac{\rho_o c_o}{\omega m} \sigma(\omega) \tag{3.18}$$

Plate modal density is given by

$$n_1(\omega) = \frac{A}{4\pi} \sqrt{\frac{\rho h}{D}} \tag{3.19}$$

where h is plate thickness, ρ is plate density and D is flexural rigidity.

Cavity modal density is given by

$$n_2(\omega) \cong \frac{V \omega^2}{2\pi^2 c_o^3} \tag{3.20}$$

where V is cavity volume, c_o speed of sound in air.

Modal/FE matrix approach

In this approach, PSD of plate velocity is given by

$$[S_{vv}] = [\phi][S_{vv,mn}][\phi]^T \tag{3.21}$$

$$[S_{vv,mn}] = [H_{mn}][C_{mn}][\psi_{pp}][C_{mn}]^T[H^*_{mn}]^T \tag{3.22}$$

where $[C_{mn}] = [\phi]^T[C]$

where mechanical impedance matrix of the plate is given by

$$[Z_s] = -\omega^2\,[M] + [K] + j\omega[C_a]$$

where $[H]$ is the mobility transfer function matrix , $[H] = [Z_s]^{-1}$

Quadratic velocity is given by

$$\langle V^2(\omega)\rangle = \frac{1}{2A}\int_A v_m n v^*_{mn} dA = \frac{\omega^2}{2}(\langle V^2(w^*)\rangle)[C]\langle V^2(w)\rangle \tag{3.23}$$

$$S_{vv}(\omega) = \frac{\omega^2}{2A} trace([S_{ww}][C]) \tag{3.24}$$

where

$$[C_{mn}] = [\phi^T][C][\phi]$$

In modal form the quadratic velocity is given by

$$S_{vv}(\omega) = \frac{\omega^2}{2A} trace([S_{ww,mn}][C_{mn}]) \tag{3.25}$$

Power input is given by

$$P_{in} = \frac{1}{2} Re \int_s p v^*_n dA$$

$$P_{in} = \frac{1}{2} Re(trace(j\omega[H][C][\psi_{pp}][C]^T)) \tag{3.26}$$

Modal Approach

$$P_{in} = \frac{1}{2} Re(trace(j\omega [H_{mn}][\phi]^T [C][\psi_{pp}][C]^T [\phi]) \tag{3.27}$$

Radiated power is given by

$$P_{rad} = \frac{\omega^2}{2} Re(trace([H_{mn}][C_{mn}][\psi_{pp}][C_{mn}]^T [H^*_{mn}]^T [\phi]^T [Z_{rad}][\phi] \tag{3.28}$$

where Z_{rad} is radiation impedance matrix of the plate.

3.7 Vibroacoustics of plate using CFD derived Corcos model

In this section, the vibro-acoustic indicators and joint acceptance relations are determined using the expressions presented in Section 3.6. The CFD simulations will be used to compare predictions of the space averaged velocity and radiated acoustic pressure to Purdue measurements for the side mirror case. The measurements assume the panel to be radiating in free field. A cavity lined with sound absorbing wedges is used to approximate this condition. Moreover, the acoustic radiation is measured using a single microphone at a fixed location (14.5 inch below the center of plate); see Figure 3.1(a) Two predictions methods will be compared to the measured space averaged quadratic velocity. The first uses an FE simulation using the CFD calculated cross-spectral density matrix in frequency-space domain. The second used the Corcos model using the CFD derived decay coefficients given in Table 3.4 and spatially averaged PSD over entire plate. In both methods the excitation PSD was taken from the CFD simulations.

The space averaged quadratic velocity is calculated using a modal synthesis method in the two approaches. The plate's measured modal damping is used in the simulations. In the fence case in Figure 3.42, although the magnitude level of response match well the resonant frequencies in experiment does not match well with the CFD-derived Corcos model due to the presence of viscoelastic plate mounts as discussed [Park *et al.*, 2004]. Unfortunately there was no experimental data available for quadratic velocity beyond 500 Hz for fence case. The FE mesh convergence studies for mirror case as shown in Figure 3.43. In reality, the FE mesh cut-off frequency is similar to the criterion used for coherence cut-off described in curve fitting procedure in Section 3.5. But it is observed that an considerable amount of computation time could be saved if one could use six times the streamwise nodes compared to the spanwise nodes and obtain the same kind of response without having an equal

number of nodes in each direction. In Figure 3.44, CFD-derived Corcos model correlates well with experiments for mirror case until 700 Hz, beyond which there exists a slight mismatch. The mismatch could be attributed to the single set of global Corcos parameters for the entire plate instead of using zone wise set and then summing up the response. The correlation with the finite element results is good over the entire frequency range. The plate in experiments might be heavily damped hence the resonant modes are fully absent like incase of FE or CFD-derived Corcos approach.

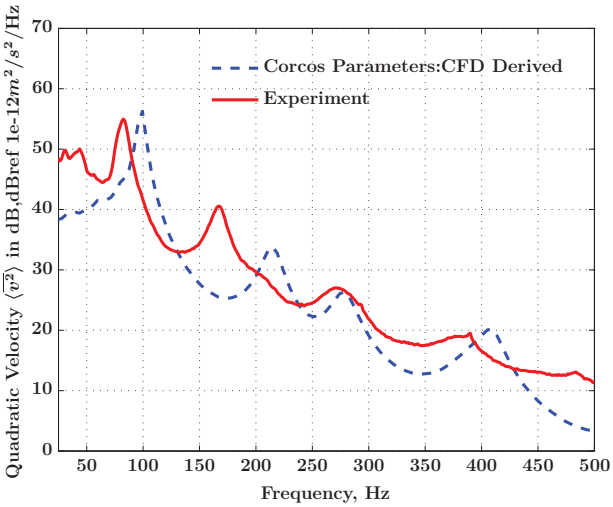

Figure 3.42 Spatial averaged quadratic velocity from CFD derived Corcos model and experiments for fence case

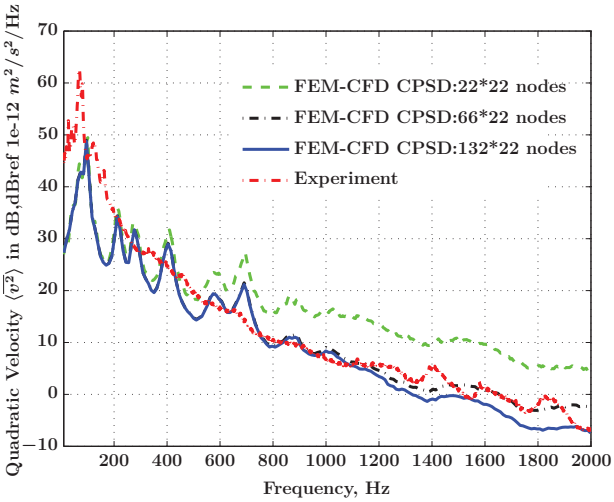

Figure 3.43 FEM mesh convergence study using CFD CPSD data and experiments for side mirror case

The quadratic pressure at the microphone location is predicted using Rayleigh integral. The input for the Rayleigh integral is the quadratic velocity obtained from CFD-derived Corcos

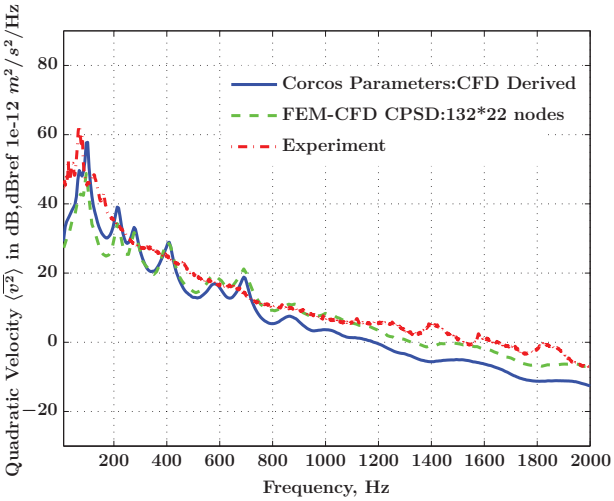

Figure 3.44 Spatial averaged quadratic velocity from FEM, CFD derived Corcos model and experiments for mirror case

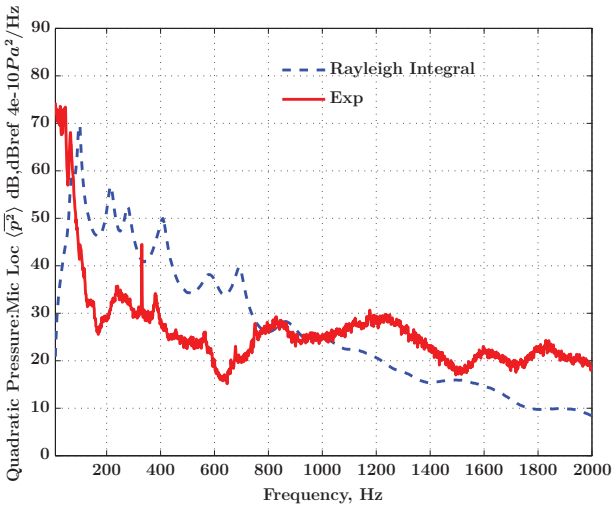

Figure 3.45 Quadratic pressure from CFD derived Corcos model, Rayleigh integral and experiments for side mirror case

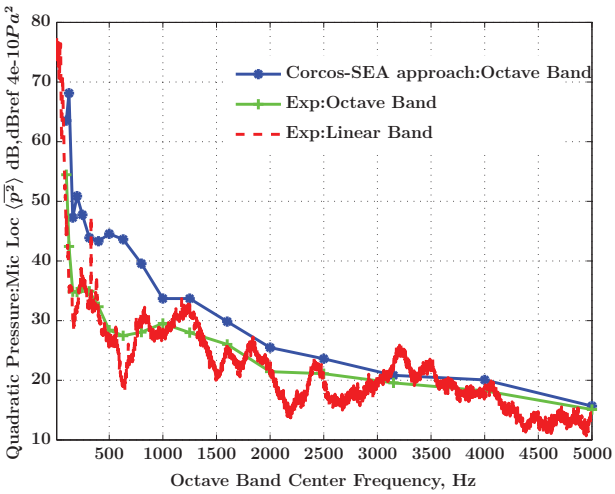

Figure 3.46 Quadratic pressure from CFD derived Corcos model, SEA and experiments for side mirror case

model. Rayleigh integral assumes a free field sound propagation. The results are given in Figure 3.45. The agreement with tests is poor at low frequencies. At higher frequencies, the comparison is better in the sense that the simulation follows the experimental trend. Several factors may explain the differences at low frequencies. Firstly, the prediction approach assumes the plate to radiate in free field. However, the used cavity is not totally anechoic at these low frequencies below 1500 Hz as noticed by [Caillet, 2008]. A simulation based on SEA using a plate-cavity system gave results similar to the Rayleigh's predictions shown in Figure 3.46. The SEA predictions are however highly sensitive to the used damping in the cavity and SEA method requires more resonant modes in cavity contrary to the anechoic cavity. An experimental characterization of this damping is needed to better assess the causes of the low frequency discrepancies. In addition, the measured pressure may be contaminated by flow noise.

3.8 Conclusions

Turbulent wall pressure statistics on the canonical cases for A-pillar and real vehicle side mirror are studied using CFD. Empirical model parameters for turbulent excitation are deduced from the CFD wall pressure coherence for both cases. A zone by zone identification helps to have local homogeneity inside the zone of study which makes the empirical curve fitting approach more suitable for non-homogeneous flows also. Empirical model parameters are in good agreement with experimental values and they are used to predict the vibroacoustics of plate. To have excellent prediction of the second-order statistics like coherence of wall pressure required, it would be recommended to have longer time histories as done in our study. The longer time history helps to have time convergence

and thereby better vibroacoustic power input predictions. The estimation of Corcos parameters from a statistically converged CFD wall-pressure, by segregating homogeneous zones based on auto-spectrum and reattachment contours forms an original contribution of this thesis. The k-ω code developed as a part of this work could be used for post-processing of unsteady wall-pressure either from CFD or experiments. The wavenumber-spectrum data from this code could be used for FE or wavenumber domain computations. The same k-ω code can also be used to study non-homogeneity in wavenumber spectrum. The CFD simulations were able to capture both aerodynamic and acoustic regions in the wavenumber spectrum perfectly which is a major accomplishment so as to proceed with accurate vibro-acoustics simulation in further steps. The quality of spatio-temporal results of wall-pressure also confirm the requirement for lengthy run. Quadratic velocity of the plate and its acoustic radiation have been predicted from an empirical model using the CFD derived parameters and compared to both finite element method (using the CFD cross-spectral density matrix) and with experiments.

CHAPTER 4

POWER INPUT DUE TO CFD DERIVED TBL EXCITATION IN WAVENUMBER DOMAIN

4.1 Introduction

Most of the aero-vibro-acoustic response methods in literature employ a joint acceptance integration in spatial domain to calculate the TBL power input to a structure [Bremner and Wilby, 2002; Rosa and Franco, 2008]. These methods make use of empirical models of the TBL excitation in terms of auto-spectrum and cross-spectrum for their convenience in joint acceptance computation. This type of empirical models have limitations for non-homogeneous flow and adverse pressure gradient conditions. A finite element method to resolve the modeshapes combined with CFD to resolve the cross spectrum of TBL excitation is obviously the next natural approach. However, it has computational limitations at joint-acceptance spatial integration. This chapter deals with a novel wavenumber approach in the numerical modeling of the TBL power input using CFD wall-pressure excitation. There is not much literature available that deals with the TBL power input calculation using the CFD wall-pressure, especially in the wavenumber domain except [Blanchet *et al.*, 2016]. In their work, the computational details for the wavenumber integration of joint acceptance were not described. In our present work, a novel approach was implemented to further reduce the computational time in wavenumber integration by incorporating upper limits based on modal wavenumber rather than multiples of coincidence wavenumber or convection wavenumber. These upper limits are based on the physical wave interaction between TBL and structural modes as described in [Hambric *et al.*, 2004]. A brief review of the numerical modeling of the turbulent excitation in wavenumber domain and its integration is presented in the following sections. The main objective is to convert the spatio-temporal varying wall-pressure excitation from unsteady CFD simulation into power input to the plate. The vibro-acoustic indicators like quadratic velocity, power input and joint acceptance relations are determined using the expressions presented in Section 3.6.

4.2 Wavenumber domain concept

The idea is to compute the joint acceptance in wavenumber domain rather than in spatial domain utilizing the PowerFLOW predicted WPF. As noticed from Equation (4.3), the spatial domain integration of joint acceptance is four dimensional in nature. Even for a flat plate, with a fine discretisation of the cross spectral density of turbulent excitation, it is computationally intensive. In this study, the numerical evaluation of joint acceptance is conducted in wavenumber domain with wavenumber-frequency spectrum of TBL excitation and modeshapes determined in waveumber-frequency domain. There is a computational advantage when the joint acceptance is calculated in wavenumber domain as we are integrating over two dimensional streamwise and spanwise wavenumber rather than four dimensions as shown in Equation 4.11. Once the wavenumber integration is validated with Corcos model, it is extended with wavenumber-frequency wall-spectrum data from CFD and discretised modeshapes. The discretised modeshapes are generated over the same CFD mesh with spatial down sampling as the CFD mesh contains a fine resolution with 0.075 mm to 1 mm on the plate. This kind of wavenumber integration has better prospects for reducing the computational time and thereby streamlining the CFD wall pressure coupling to the finite element modeshapes that takes into account the plate boundary conditions.

4.3 Identification of the plate boundary conditions based on point mobility test

For simplicity, the automobile side glass mounting conditions with rubber seals around its periphery can be approximated between clamped and simply supported boundary conditions. Simply supported and clamped boundary conditions result in very little acceptance of excitation at convective ridge pressures and have higher acceptance at low wavenumbers as shown in Figure 4.12. A simple point mobility experiment as shown in Figure 4.1 is conducted on a typical automotive side glass to confirm the plate boundary conditions needed for the joint acceptance integration. An impact hammer and accelerometer was placed at same location on side glass to ensure the point mobility measurement. FE simulations for the real side glass are performed in a commericial FE solver and the results are presented in Figure 4.2 for various boundary conditions of plate. After comparison the point mobility from experiments, it was found that simply supported boundary conditions are an acceptable approximation to real mount conditions of side glass. In the driving point mobility plot, the modal peaks obtained from FE simulation are much dominant compared to the experimental value due to two reasons. First reason is that a constant structural damping value of 0.01 was used in FE calculations and the other reason is the fact that

damping of real side glass varies with frequency and much higher due to its laminated nature. Based on the structural point mobility analysis,the modeshapes corresponding to the simply supported boundary conditions have been used in our numerical calculations of joint acceptance. The analytical joint acceptance (hand derived) for Corcos model has been validated with symbolic integration in MAPLE software before using it as validation benchmark for spatial and wavenumber numerical integration.

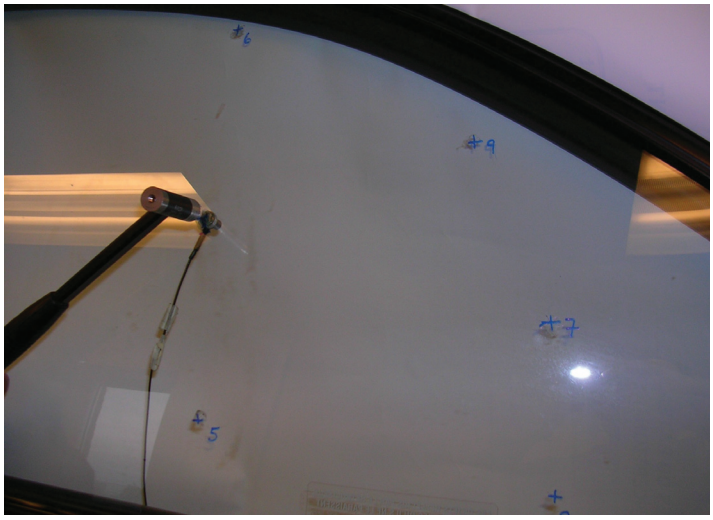

Figure 4.1 Driving point mobility test on side glass of passenger car

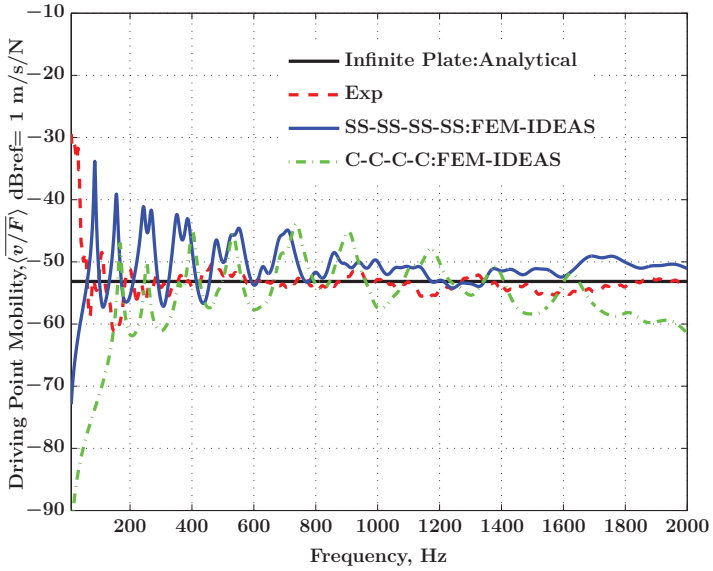

Figure 4.2 Comparison of experimental point mobility with FEM

4.4 Numerical evaluation of joint acceptance in spatial domain with cross spectral density known at discrete points

To determine the power input to a simply supported plate due to turbulent boundary layer excitation, the joint acceptance function has to be evaluated. In this report, the joint acceptance function is calculated in spatial domain with a known cross spectral density model of TBL excitation determined at discrete points.

The mode shapes of the simply supported plate in spatial domain are given by

$$\phi_{mn}(x,y) = \sin\left(\frac{m\pi x}{a}\right)\sin\left(\frac{n\pi y}{b}\right) \tag{4.1}$$

Where x and y are spatial coordinates a, and b are the dimensions of the plate,m and n are the order of the modes. The cross spectral density of Corcos model for the TBL excitation is obtained at discrete points in spatial domain as

$$\psi(x,y,x',y',\omega) = S_{pp}(\omega)e^{-\left|\frac{\omega r_x}{\alpha_x U_c}\right|}e^{-\left|\frac{\omega r_y}{\alpha_y U_c}\right|}e^{\frac{i\omega r_x}{\alpha_x U_c}} \tag{4.2}$$

Where (x,y) are coordinates of measurement point on the plate and (x',y') are the coordinates at reference point on the plate, $r_x = x - x'$ and $r_y = y - y'$, U_c is the convection velocity, $1/\alpha_x$ and $1/\alpha_y$ are the decay constants given by the power spectrum model chosen as 0.1 and 0.72 for [Robert, 1984]. Joint acceptance function is evaluated numerically by integrating the product of the mode shapes and Corcos model in the spatial domain as

$${j_{mn}}^2 = \frac{1}{(A)^2}\int_A\int_A \phi_{mn}(x,y)\psi(x,y,x',y',\omega)\phi_{mn}(x',y')dxdydx'dy' \tag{4.3}$$

Note that Equation (4.3) can be integrated analytically and the result from numerical integration was compared to the closed form to show the difficulty involved in numerical integration of joint acceptance in spatial domain.

Numerical procedure: Spatial domain

The simply supported plate is divided into finite elements as in Figure 4.3 and joint acceptance integral is evaluated in each element. A bi-linear rectangular element with linear interpolation was chosen and Guass quadrature was used to integrate the joint acceptance in spatial domain. For each bi-linear element, it has two Gauss points in each

direction and the two functions are evaluated at Gauss points. The integral has been evaluated over the Gauss limits in each direction. The Lagrangian interpolation functions used for the bi-linear rectangular element are taken from [Atalla and Sgard, 2015]

$$\begin{aligned} N_1 &= \frac{1}{4}(1-\xi)(1-\eta) \\ N_2 &= \frac{1}{4}(1+\xi)(1-\eta) \\ N_3 &= \frac{1}{4}(1+\xi)(1+\eta) \\ N_4 &= \frac{1}{4}(1-\xi)(1+\eta) \end{aligned} \tag{4.4}$$

The Corcos model cross spectrum in spatial domain has been transformed into an isoparametric coordinates (ξ, η) as shown in Figure 4.3 using the interpolation functions(first order) as $\psi_e(\xi, \eta, \omega)$ for each element.

$$\psi_e(\xi, \eta, \omega) = \sum_{i=1}^{4} N_i(\xi, \eta)\ \psi_i(x, x', y, y', \omega) \tag{4.5}$$

The geometrical coordinates for each element in spatial domain have been transformed into isoparametric coordinates using the interpolation function as

$$\begin{aligned} x_e &= \sum_{i=1}^{4} N_i(\xi, \eta)\ x_i \\ x'_e &= \sum_{i=1}^{4} N_i(\xi, \eta)\ x'_i \\ y_e &= \sum_{i=1}^{4} N_i(\xi, \eta)\ y_i \\ y'_e &= \sum_{i=1}^{4} N_i(\xi, \eta)\ y'_i \end{aligned} \tag{4.6}$$

The modeshapes of the simply supported panel are also transformed into the isoparametric coordinates as

$$\phi_{mn_e}(\xi, \eta) = \phi_{mn}(x_e, y_e) \tag{4.7}$$

$$\phi'_{mn_e}(\xi, \eta) = \phi_{mn}(x_e{}', y_e{}') \tag{4.8}$$

The four dimensional integration is evaluated using Gauss quadrature and transforming

the spatial domain to the isoparametric space with a Jacobain ($J(\xi,\eta)$) as scaling factor as follows

$$= \frac{1}{(A)^2}\int_{-1}^{1}\int_{-1}^{1} \phi_{mn}(x,y)N_i(\xi,\eta)\ \psi_i(x,y,x',y',\omega)\ \phi_{mn}(x',y')J(\xi,\eta)d\xi d\eta \tag{4.9}$$

Finally the integral reduces to the summation of each Gauss points (gx, gy) for each element as in Figure 4.3 and sum of all elements in the spatial domain. A 2×2 Gauss point integration scheme with linear elements were chosen.

$$= \frac{1}{(A)^2}\sum_{p=1}^{gx}\sum_{q=1}^{gy} W_pW_q\phi_{mn_e}(\xi_p,\eta_q)\psi_e(\xi_p,\eta_q,\omega)\phi'_{mn_e}(\xi_p,\eta_q)\ J_e(\xi_p,\eta_q) \tag{4.10}$$

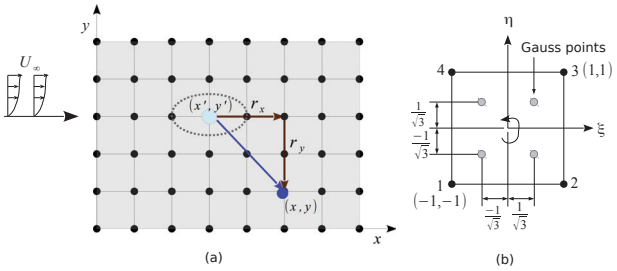

Figure 4.3 Plate mesh(left) with measurement and reference locations and Gauss bi-linear element (right) for interpolation

The input data such as plate details and turbulent flow properties presented in Table 4.1 remain the same for spatial and wavenumber integration. The time required for the computation of joint acceptance integral in spatial domain for each mode is 10869 CPU sec for 2500 elements on Intel core 2 Duo Desktop machine with 16 GB RAM. The joint acceptance convergence results in spatial domain for mode $m = 1$ and $n = 1$ are compared to the closed form value of integral (Figure 4.4). For higher modes in Figure 4.5, the joint acceptance do not converge well even with large number of elements. The joint acceptance integration in spatial domain is very time consuming and expensive for each mode. To overcome this disadvantage wavenumber domain integration of joint acceptance is proposed.

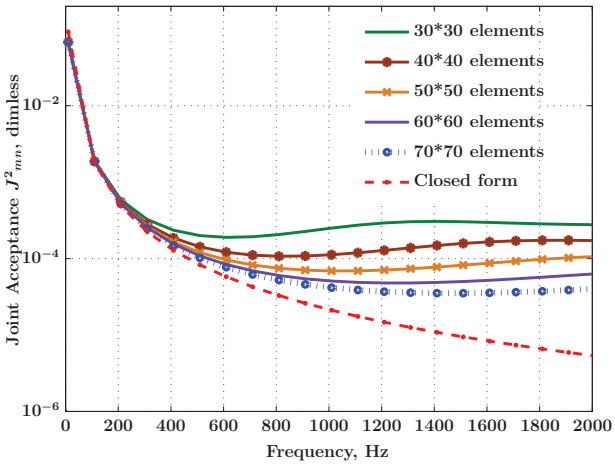

Figure 4.4 Convergence of joint acceptance function for mode m=1 and n=1 in spatial domain

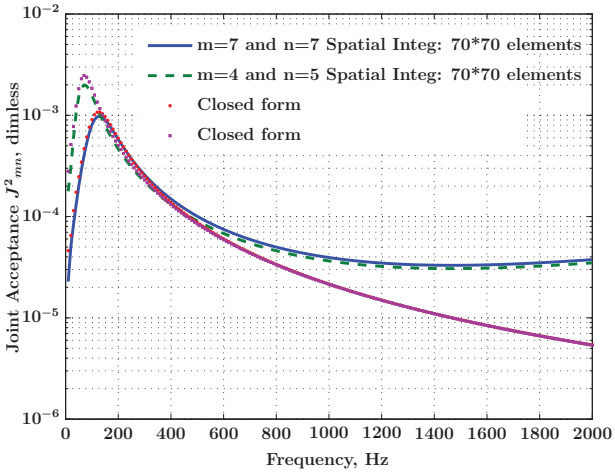

Figure 4.5 Joint acceptance for mode m=7 and n=7 obtained in spatial domain

4.5 Numerical evaluation of joint acceptance in wavenumber domain with wavenumber-frequency spectrum known at discrete points

To determine the power input to a simply supported plate due to turbulent boundary layer excitation, the joint acceptance function has to be evaluated. In this section, the joint acceptance function is calculated in wave number domain with a known wavenumber-frequency spectrum of turbulent boundary layer (TBL) excitation determined at discrete points. The mode shapes of the simply supported plate and the cross-spectral density of Corcos model in wavenumber space are determined at the discrete points using the definition of spatial Fourier transform. Due to the two-dimensional wavenumber integration of joint acceptance and the proposed criterion for upper limits of integration as discussed in Section 4.7, there was a significant improvement in computation compared to spatial domain. The modal sensitivity function and Corcos model excitation in wavenumber domain is given as follows

$$|\phi_{mn}(k_x,k_y)|^2 = \frac{\frac{2m^2\pi^2}{a^2}\left[1-(-1)^m\cos k_x a\right]}{\left[\frac{m^2\pi^2}{a^2}-{k_x}^2\right]^2}.\frac{\frac{2n^2\pi^2}{b^2}\left[1-(-1)^n\cos k_y b\right]}{\left[\frac{n^2\pi^2}{b^2}-{k_y}^2\right]^2}$$

$$\psi(k_x,k_y,\omega) = \frac{S_{pp}\left(\frac{U_c}{\omega}\right)^2}{\left({\alpha_x}^2+\left(\frac{U_c k_x}{\omega}-1\right)^2\right)\left({\alpha_y}^2+\left(\frac{U_c k_y}{\omega}\right)^2\right)}$$

Where k_x and k_y and are the wavenumbers in x and y direction a and b are the dimensions of the plate, m and n are the order of the modes. The wavenumber-frequency spectrum of Corcos model is obtained at discrete points in wave number space mesh as shown in Figure 4.6. Similarly the plate modeshape values are also obtained at discrete points on the mesh using analytical expression. The plot for the modeshapes for $m = 1$ and $n = 1$ of a simply supported plate in wavenumber space are as shown in Figure 4.7, which has a maximum at origin.

Joint acceptance function is evaluated numerically by integrating the product of the mode shapes and Corcos model in the wavenumber space using the Equation 4.11.

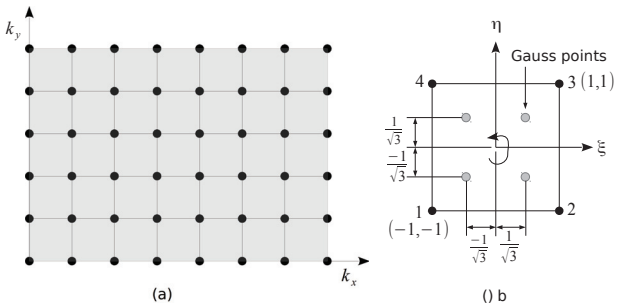

Figure 4.6 Wavenumber mesh (left) and Gauss bi-linear element (right) for interpolation

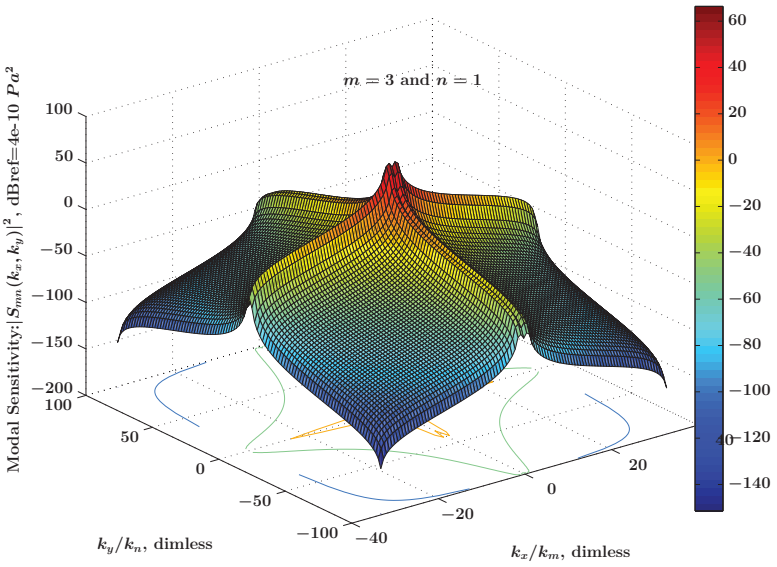

Figure 4.7 Modeshape of simply supported plate for mode $m = 3$ and $n = 1$ in wavenumber domain

$$j_{mn}{}^2 = \frac{1}{(2\pi A)^2} \int_0^\infty \int_0^\infty |\phi_{mn}(k_x, k_y)|^2 \psi(k_x, k_y) dk_x dk_y \tag{4.11}$$

It's imperative to visualise the plots of modeshapes and Corcos model demonstrating the complexity of shapes and singularity before choosing the numerical method of integration. The plot for the Corcos model in wavenumber frequency for a particular frequency is shown in Figure 4.8. In Figure 4.9, the two-dimensional Corcos wavenumber-frequency spectrum for a particular frequency shows the convective ridge. In a geometric sense, the wrinkled modeshapes and the peak shaped convective excitation spectrum pose a complexity in terms of numerical integration in addition to the singularities and limits of wavenumber integration.

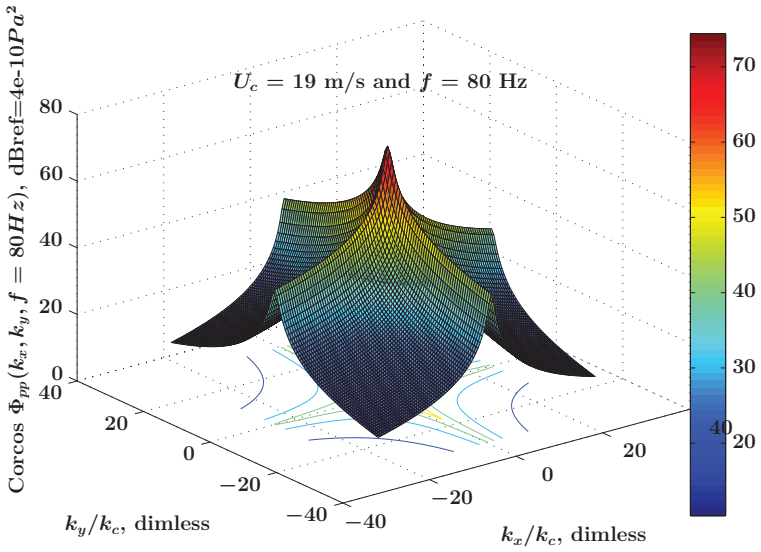

Figure 4.8 Corcos model at 5 Hz frequency in wavenumber domain

Numerical procedure: Wavenumber domain

The numerical approach is similar to the one discussed in Section 4.4.

The Corcos model for each element in wavenumber space has been transformed into an isoparametric coordinates using the interpolation functions as

$$\psi_e(\xi, \eta, \omega) = \sum_{i=1}^{4} N_i(\xi, \eta)\ \psi_i(k_x, k_y, \omega) \tag{4.12}$$

The geometrical coordinates for each element in wavenumber space have been transformed

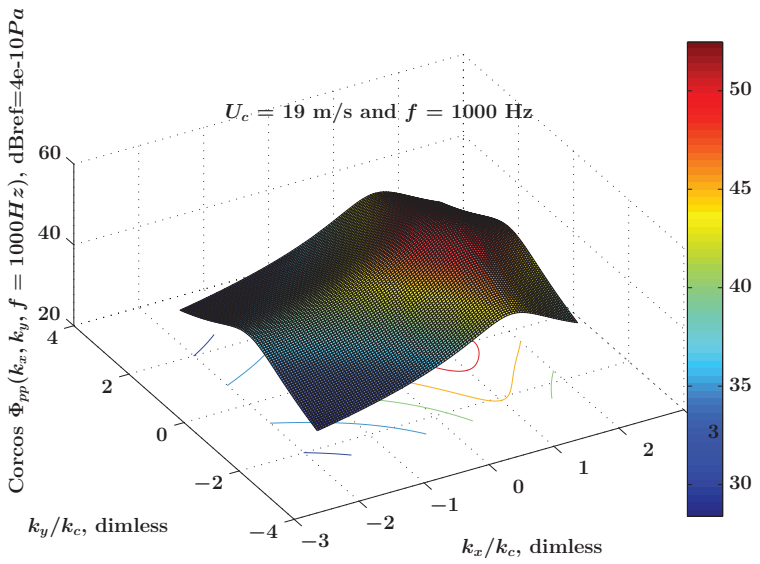

Figure 4.9 Corcos model at 1000 Hz frequency in wavenumber domain

into isoparametric coordinates using the interpolation function as

$$\begin{aligned} k_{x_e} &= \sum_{i=1}^{4} N_i(\xi,\eta)\ k_{x_i} \\ k_{y_e} &= \sum_{i=1}^{4} N_i(\xi,\eta)\ k_{y_i} \end{aligned} \tag{4.13}$$

The modeshapes of the simply supported panel are transformed into the isoparametric coordinates as

$$|\phi_{mn_e}(\xi,\eta)|^2 = |\phi_{mn}(k_{xe}, k_{y_e})|^2 \tag{4.14}$$

The joint acceptance function with upper limits many times higher than the coincidence wavenumber k_{hmax} are written as

$$j_{mn}{}^2 = \frac{1}{(2\pi A)^2} \int_0^{k_{hmax}} \int_0^{k_{hmax}} |\phi_{mn}(k_x, k_y)|^2 \psi(k_x, k_y) dk_x dk_y$$

where $k_{hmax} = 10 \times k_h$. Before presenting the results of the comparison with the closed form solution in Section 4.8, a discussion on the selectiob of the integration limit K_max is presented

4.6 Wavenumber interaction between TBL and structural modes

In this section, we are going to find an answer to this question "Is joint acceptance high for the side glass in the low wave number region of excitation ?". The concept of *slow* and *fast* mode as described by [Hambric *et al.*, 2004] for TBL and structural interactions have been used to optimally decide the integrations limits for wavenumber integration of joint acceptance. Even in the diffuse field excitation, the concept of slow and fast mode holds good as described in [Fahy and Gardonio, 2007] and [Atalla and Sgard, 2015]. The flexural wave speed is a proportional to the square root of frequency. When the flexural wave speed lags behind the TBL convection speed, the structural mode is considered to be *slow mode* with respect to TBL. When the flexural wave speed leads ahead of the TBL convection speed, the structural mode is considered to be *fast mode* with respect to TBL. But when the flexural wave speed matches with TBL convection speed, the frequency at which this speed match happens is known as coincidence frequency. To demonstrate the dispersion curves with coincidence frequencies for various excitations, the aluminium plate and TBL flow details are taken from Table 4.1. The dispersion curves showing the coincidence frequencies for coupling of acoustic,convection and structural wavenumber is shown in Figure 4.10. At the aerodynamic coincidence in Figure 4.10 the phase velocities of structural bending and convective wave match and there is a large coupling in wavenumbers there onwards. The streamwise wavenumber spectrum and structure wavenumber sensitivity function are computed for low and high speed flows using the plate and TBL details given in Table 4.1.

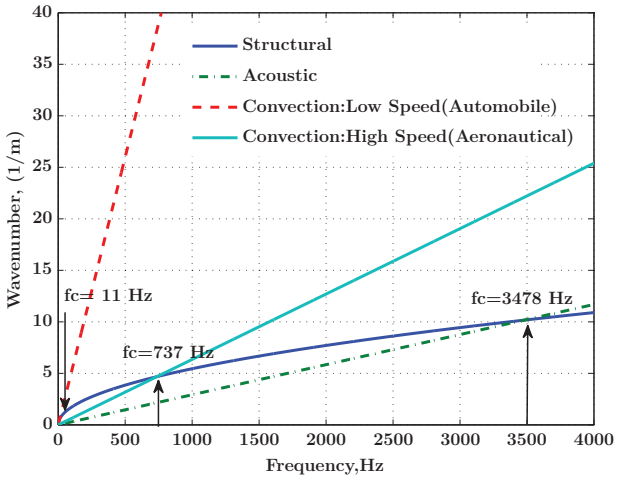

Figure 4.10 Wavenumber-frequency diagrams: dispersion curves

Name	Plate & TBL details
Length	$a = 0.47\ m$
Breadth	$b = 0.37\ m$
Thickness	$h = 0.0034\ m$
Flexural rigidity	$D = \frac{Eh^3}{12(1-\upsilon^2)}\ Pa.m^3$
Mass density	$\rho = 2700\, kg/m^3$
Young's modulus	$E = 7.2 \times 10^{10} Pa$
Poisson's ratio	$\upsilon = 0.34$
Free stream velocity	$U_\infty = 43.6\ m/s$
Convection velocity	$U_c = 0.7U_\infty\ m/s$
Corcos model decay coefficients	$1/\alpha_x = 0.1$ and $1/\alpha_y = 0.72$
Coincidence wave number	$k_h = U_c\sqrt{\frac{\rho h}{D}}\ rad/m$
Convective wave number	$k_c = \frac{\omega}{U_c}\ rad/m$

Table 4.1 Plate and TBL details for Joint acceptance calculation

A three dimensional view of Corcos model in terms of wavenumber-frequency spectrum is illustrated in Figure 4.9 for a fixed frequency at low Mach number. This spectrum can be characterised into two regions, a) the low wave number region where the surface interactions dominate the structural acceptance of the energy from the flow field and b) the convective region centered at, where edge interactions dominate the response, [Chandiramani, 1977]. The strongest pressure fluctuations occur within the convective ridge. In the case of marine and automotive applications, as the flow velocity is very low, there is an importance of estimation of low wave number components. For aerospace applications where the flow is attached and with high Mach number, the estimation of convective ridge is very important compared to the low wave numbers.

In low speed flows as shown in Figure 4.11, the dominant modal wavenumber response coincides with the dominant wavenumber range of the TBL excitation near the convective ridge for a slow structural mode with respect to TBL. For a *low speed* convective TBL flow usually observed in automobile, structural mode is *always fast* due to the low convection velocity, hence the low wave number TBL becomes dominant due to strong acceptance of structural mode like in Figure 4.12. These fast structural modes are present, when the ratio of structural bending wavenumber and convective wavenumber is quite low due to panel stiffening and low speed convective TBL flow. In Figure 4.12, the structure is excited mostly by the low wavenumber content in both clamped and simply supported (SSP) boundary conditions which is the case in our present test cases. In similar way, the

wavenumber interaction between high speed flow with slow and fast modes are presented in Figures 4.13 and 4.14. Due to the *high speed TBL* flow, the structural modes are *always slow* and there by the estimation of convective ridge is very important compared to the low wave numbers as observed in Figure 4.13. The response due to the slow structural mode interaction would be low due to the absence of any structural acceptance available to take in the TBL excitation as shown in Figure 4.14. Based on this wavenumber interaction, the upper limits of wavenumber integration can be decided to reduce the computational effort for both low speed and high speed TBL flows.

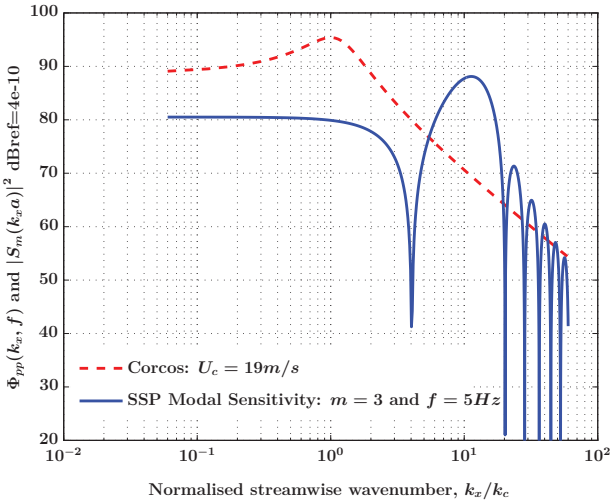

Figure 4.11 Wavenumber interaction between low speed flow and slow mode

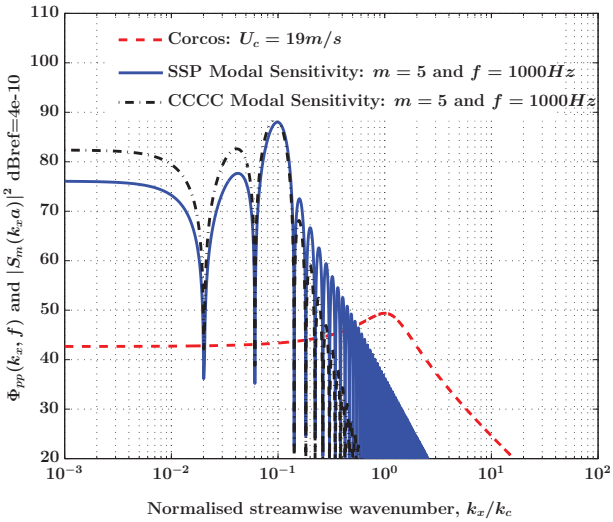

Figure 4.12 Wavenumber interaction between low speed flow and fast mode under clamped and SSP BC

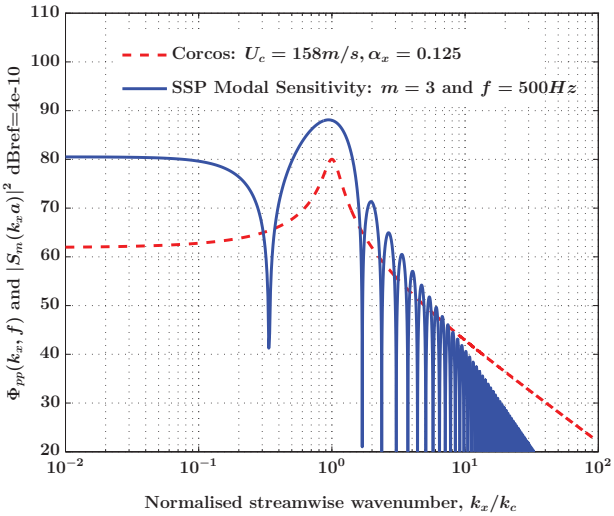

Figure 4.13 Wavenumber interaction between high speed flow and slow mode

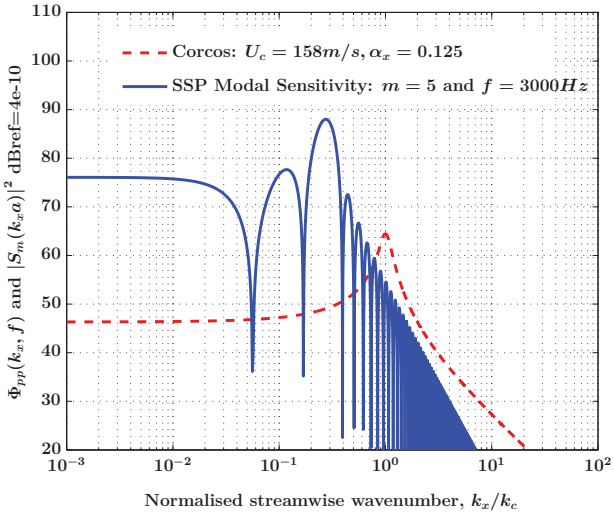

Figure 4.14 Wavenumber interaction high speed flow and fast mode

4.7 Upper limits of joint acceptance integration at low speed flow

Both structural and turbulent convection wavenumbers have to be properly resolved for good convergence of joint acceptance. Hence deciding the upper limits of integration are very crucuial for successfull wavenumber integration. In theory and past experience from wavenumber integration for diffuse acoustic field excitation, an upper limit of 10-20 times the coincidence wavenumber ($10k_h - 20k_h$) should be good enough depending on the maximum frequency of concern. Unfortunately setting the upper limits based on coincidence wavenumber does not yield any improvement in computation time as shown in Table 4.2. With the increase in structural mode order, the computational effort increases and corresponding upper limits of integration needs to be increased to capture the higher orders.

Integration	Mode m and n	Frequency Step, Hz	Upper limit Frequency, Hz	Number of elements	Upper limit of Integration	Time and Computer
Analytical	7,7	100	5000	–	–	0.78 sec, Intel Core 2 duo CPU
Wavenumber	7,7	100	5000	100	$15k_h$	2.49 sec, Intel Core 2 duo CPU

Table 4.2 Computation time for the joint acceptance integration for higher structural modes

If for suppose, the upperlimits are based on the multiple times of convection wavenumber, k_c. The wavenumber integral would have to be determined for each frequency where the upper limits are also a function of frequency. This would be highly computational intensive at higher frequencies. For this reason, the maximum value of k_c based on maximum frequency of interest could be used as the upper limits of wavenumber integration. But setting the upper limits based on maximum value of k_c leads to more computational effort as shown in Figure 4.15 with the need for hundreds of elements to match the closed form joint acceptance. The smart approach to set the upper limits of wavenumber integration would be based on structural modal wavenumber, k_{mn}. The basic idea is as follows, the major amount of joint acceptance is present only in the region of high acceptance lobes of the structural modeshapes as shown in Figures 4.12 and 4.14. It would be obvious to integrate the joint acceptance whereever its dominant rather than with respect to the

convection wavenumber. Even with a 1-3 times the maximum of k_m and k_n, the higher order joint acceptance would converge faster to the closed form value within a few ten's of elements in each direction as shown in Figure 4.15. This trick works well for high speed flows. As noticed in Figures 4.13 and 4.14, the convective ridge becomes the dominant term and couples well with the structural modal lobes. Similar to low speed flows, joint acceptance integration for high speed flows could be peformed with upper limits based on modal wavenumbers irrespective of the dominant contributions from TBL. For a high speed flow of 225 m/s, the joint acceptance integration with upper limits of 2.5 times the k_{mn} predicts well with closed form values for lower and even higher modes (Figures 4.16 and 4.17).

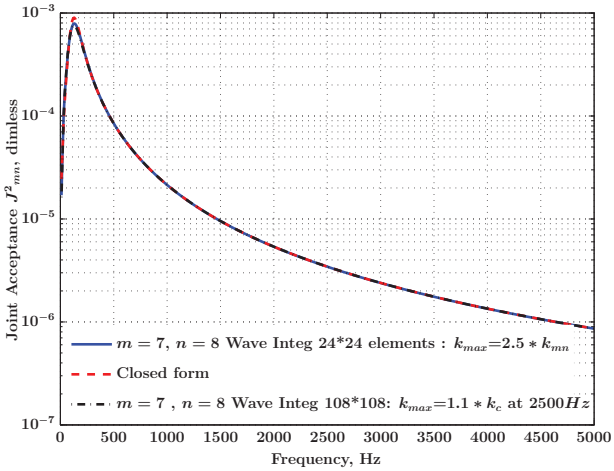

Figure 4.15 Joint acceptance calculated in wave number domain for m=7 and n=8 based on convective wavenumber and modal wavenumber

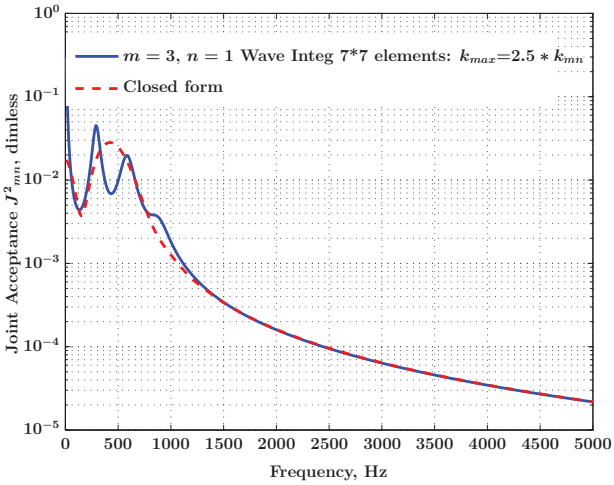

Figure 4.16 High speed flow: Joint acceptance in wavenumber domain for $m = 3$ and $n = 1$ and analytical value

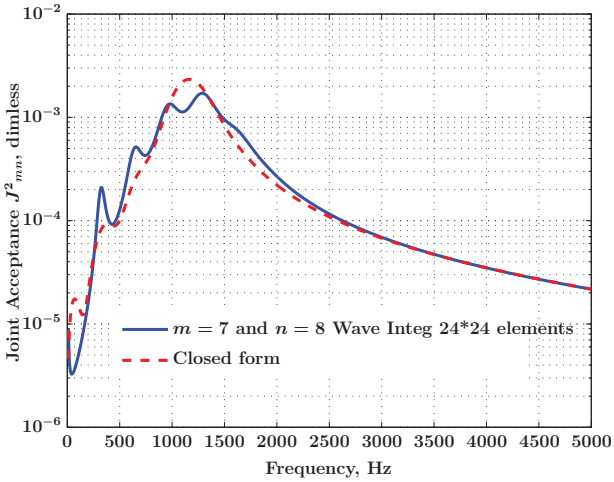

Figure 4.17 High speed flow: Joint acceptance in wavenumber domain for $m = 7$ and $n = 8$ and analytical value

4.8 Validation of joint acceptance integration using Corcos model

The vibro-acoustic indicators like quadratic velocity and power input are calculated from the joint acceptance integration in wavenumber domain. Both quadratic velocity and power input have a perfect match with spatial domain as shown in Figures 4.18 and 4.19. It is noted that Corcos model was used to generate the TBL excitation in terms of wavenumber and spatial domain for use in the joint acceptance integration. With the assurance from this validation, the numerical scheme of joint acceptance integration in wavenumber domain is extended to calculate the vibroacoustics with CFD wall-pressure excitation.

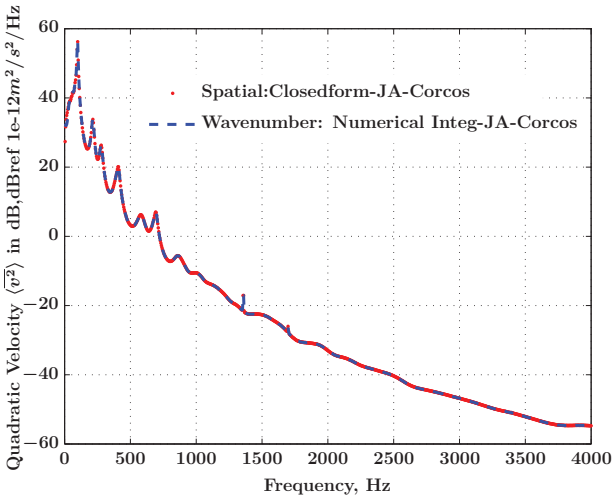

Figure 4.18 Quadratic velocity using Corcos in spatial vs wavenumber domain for fence case at low speed

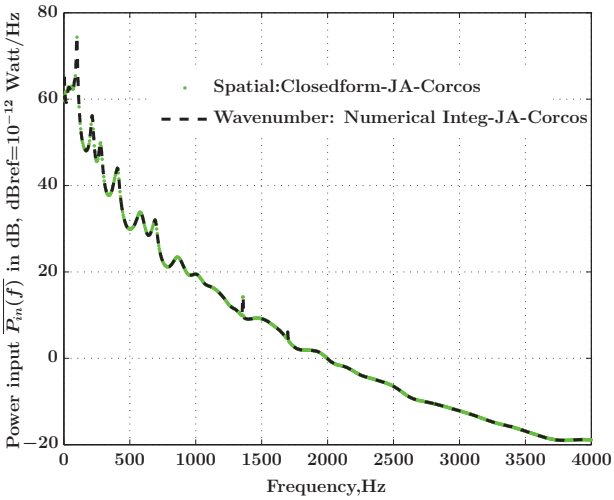

Figure 4.19 Power input using Corcos in spatial vs wavenumber domain for fence case at low speed

4.9 Validation of joint acceptance integration using CFD wavenumber WPF

In this section, the CFD derived k-ω spectrum was used as the excitation term instead of the Corcos model. The joint acceptance integration is calculated in wavenumber domain with upper limits based on 1.2 times modal wavenumber k_{mn} for both flat fence and side mirror cases. The modal summation of joint acceptance computed with CFD wavenumber wall-pressure does not fully match with that of the Corcos analytical value as expected in Figure 4.20 due to the Corcos model weakness.

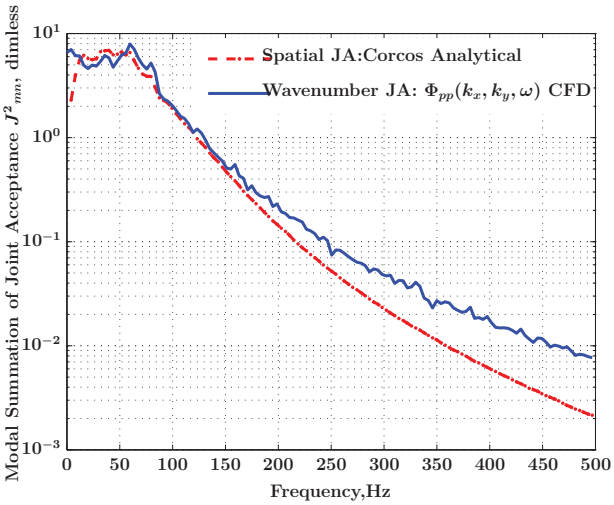

Figure 4.20 Fence case: Joint acceptance in wavenumber using CFD wavenumber WPF vs Corcos model

The Corcos model used in this calculation makes use of the PSD from CFD and the cross-spectrum term of the model is based on empirical values of decay paramters that does not take into account of the spatial variation of TBL. The quadratic velocity in Figure 4.21 is calculated from the wavenumber integration of joint acceptance. It does match well until 250 Hz with spatial joint acceptance integration when CFD derived Corcos model was used in spatial domain. The mismatch beyond 250 Hz could be due the fact that a single set of CFD-derived Corcos parameters was used for the entire plate.

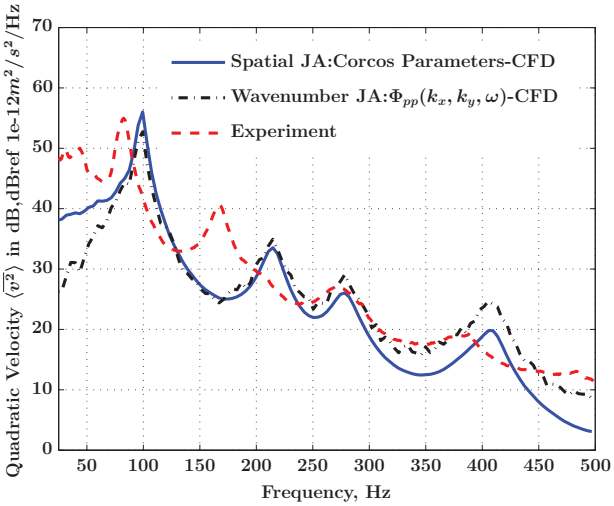

Figure 4.21 Fence case:Quadratic velocity using CFD wavenumber WPF and CFD derived Corcos model

In Figure 4.22, as expected the joint acceptance from wavenumber integration has a clear mismatch with spatial value due to the fact that Corcos analytical model with empirical decay parameters could not predict well the side mirror TBL flow excitation. Finally the quadratic velocity from wavenumber integration in Figure 4.23 does fall in the close range of FEM-CPSD prediction and experiments. This validates the wavenumber integration numerical scheme and provides an computationally efficient solution for modelling of TBL excitation. The quadratic velocity from CFD-derived Corcos model falls apart above 500 Hz from the rest of simulations and experiment due to their single set of Corcos parameters from attached zone and spatially averaged PSD. A patch wise joint acceptance calculation based on a set of Corcos parameters for each localised homogeneous zone on the plate would be a prospective route for further studies.

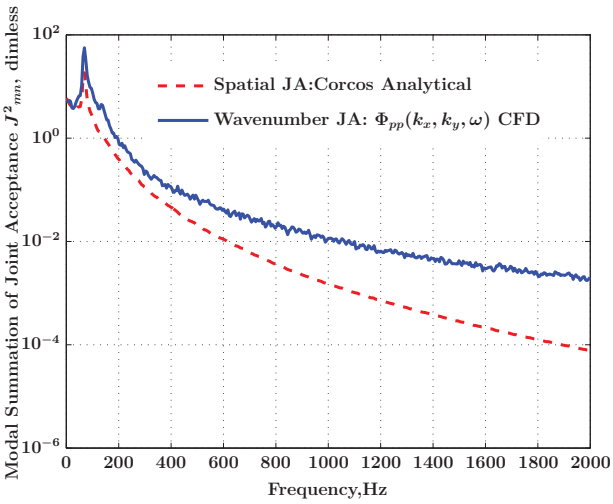

Figure 4.22 Side mirror case: Joint acceptance in wavenumber using CFD wavenumber WPF and Corcos model

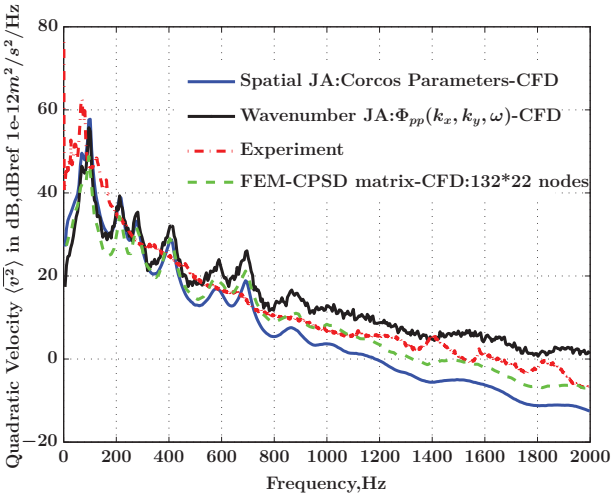

Figure 4.23 Side mirror case: Quadratic velocity using CFD wavenumber WPF and CFD derived Corcos model

4.10 Conclusions

In an effort to efficiently compute the power input due to TBL excitation, joint acceptance has been calculated in wavenumber domain with Corcos and CFD wall-pressure data. Based on a simple point mobility experiment conducted on a typical automotive side glass and with necessary FE simulations for various boundary conditions of plate, it was found that simply supported boundary conditions are close enough approximation to real mount conditions. These corresponding modeshapes of the plate have been used in our numerical calculations of joint acceptance. The analytical joint acceptance (hand derived) for Corcos model has been validated with symbolic integration before using it as validation benchmark for spatial and wavenumber numerical integration. Even for a lower modes, a lot of linear elements were required to properly compute the joint acceptance in spatial domain using Gauss quadrature. In spatial domain, the number of linear elements required drastically increases with heavily wrinkled high order modeshapes. In fact with a few number (10-20) of linear elements per wavenumber, the higher order modes of joint acceptance are properly computed. In spatial domain integration of joint acceptance, it needs hundred's of linear elements per spatial domain direction. In order to find the optimum wavenumber mesh size criterion, one has to monitor two parameters, a) upper limits of wavenumber integration b) number of linear elements to resolve this wavenumber field. The concept of slow and fast modes that determines the coupling strength between the low Mach number TBL flow and structural modeshapes has been taken into account in setting the upper limits of wavenumber integration. The computation time for joint acceptance was reduced by calculating in wavenumber domain with two integrals instead of four dimensional integration in spatial domain and proper upper limits of wavenumber integration. Incase of a low speed TBL flow, with typical side window glass mounting conditions, the upper limits of wavenumber integration limits could be fixed at $1.2k_{mn}$. This limit should be good enough to properly capture the total joint acceptance due to the coupling between modeshapes and wavenumber spectrum of TBL excitation. The proposed upper limits also work well for high speed flows but need more verification at vibro-acoustics indicators level. Finally the vibro-acoustic indicators such as quadratic velocity match well with experimental values. Hence it is very promising to use TBL excitation in terms of CFD wavenumber-frequency spectrum to compute vibro-acoustic indicators.

CHAPTER 5

RANDOM SAMPLING OF CFD DERIVED TBL WPF

5.1 Introduction

Random sampling technique was used as an alternative approach in modelling the turbulent boundary layer (TBL) excitation compared to the traditional Finite Element(FE) simulation due to the easeness in the computation of TBL power input. Random sampling treats the TBL excitation as a stationary random process and decomposes the spatially and time correlated TBL field into distributed point forces with random phases. This decompostion step skips the computational bottleneck of joint-acceptance in FEM. In the present study, the main objective is to use CFD derived TBL excitation in terms of cross-spectral density matrix as an input to the random sampling numerical algorithm. The real question is "Is it possible to decompose the CFD wall-pressure cross-spectral density matrix into distributed point loads with random phases similar to a Corcos model cross-spectral density ?". After decomposition, a deterministic modal approach based on Rayleigh-Ritz was used to predict the plate response for the distributed point forces. The plate response is spatially and sample averaged to obtain the mean quadratic velocity of the plate. A detailed numerical alogirthm used for random sampling is given in [Coyette *et al.*, 2009], [Wittig and Sinha, 1975] and [Atalla and Sgard, 2015].

5.2 Numerical algorithm for Random sampling

The TBL excitation is decomposed in terms of spatially distributed uncorrelated point force excitation. The decomposition is based on Cholesky decomposition and modal response calculation was performed for each random sample. The mathematical expressions for vibro-acoustics indicators are discussed in Section 3.6.

Assumptions in random sampling

1. TBL is weakly stationary and homogeneous random process
2. The cross-spectral density matrix of TBL is positive definite

For a TBL excitation based on Corcos model, the cross-spectral density matrix would be Hermitian matrix due to its mathematical representation and it becomes a real matrix for diffuse field. The step-by-step numerical algorithm is described as follows

STEP 1: Generation of Cross-Spectral Density (CPSD) matrix of TBL excitation based on Corcos model at each frequency over entire plate with mesh size $(n_x \times n_x)$ nodes

STEP 2: Cholesky decomposition of the CPSD matrix into a lower triangular matrix and it's conjugate upper triangular matrix at each frequency

$[\phi_{pp}(r_x, r_y, \omega)] = [L^*][L]$

STEP 3: Generation of random phases γ_i between $[0, 2\pi]$ with help of random numbers generated between $[0, 1]$ based on a uniform distribution function $(n_x \times 1)$

$\gamma_i = 2\pi\, rand(0, 1)$

STEP 4: Calculation of the point force load vector on each nodes of the plate at each frequency as follows

$F = [L^*]e^{j\gamma_i}$

STEP 5: Evaluation of the quadratic velocity response of the plate subjected to distributed uncorrelated point force at each frequency and summed up for all modes (m, n) and averaged for all nodes $(n_x \times n_x)$ to obtain the spatially averaged quadratic velocity

STEP 6: Repeat Step 1 to 5 for every frequency from 10 Hz to 500 Hz (fence case) and 2000 Hz (side mirror case) in steps of 10 Hz

STEP 7: Repeat Step 1 to 6 for all random phase samples upto maximum samples of $M = 5$ to 10 depending on the convergence

$$S_{vv} = \frac{1}{M} \sum_{i=1toM} S_{vvi}$$

In the present case a random samples of M= 5 to 6 were sufficient to get the convergence when using the Corcos model for generation of cross spectral density matrix. For a CFD dervied cross spectrum, it would be possible to have more random samples depending on the flow turbulence involved.

5.3 Vibroacoustics of plate-cavity system using Random sampling

For a side mirror case, the cross-spectral density matrix for the CFD wall pressure on the plate was determined over a mesh (11×11) nodes. The aluminium plate dimensions are $0.528m \times 0.44m$. The mode shapes are also discretised over the same mesh using analytical expressions for simply supported panel. The above algorithm was numerically implemented in MATLAB to predict the spatially averaged quadratic velocity using random sampling

afer Cholesky decomposition. The quadratic velocity of the plate in Figure 5.1 compares well with analytical corcos model except the mismatch at resonant peaks even with a low number of five random samples. In the fence case, the experimental values of quadratic velocity were limited upto 500 Hz due to the limited dynamic range of instrument [Park *et al.*, 2004]. The mismatch at resonant peaks is attributed to the experimental mount conditions of the plate. Cholesky decompostion of CFD derived CPSD matrix was not possible for the fence and mirror cases due to the non-Hermitian nature of the CPSD matrix. The possible physical significance for the non-Hermitian nature of the CPSD matrix might be due to the absence of flow symmetry in streamwise and spanwise direction along with strong pressure gradients. Incase of side mirror, the power input and quadratic velocity of the plate in Figure 5.2 and Figure 5.3 compares well with finite element simulations using the Corcos generated full CPSD matrix. From the Figure 5.3, random sampling is able to predict the response and converge faster with fewer number of random samples and fewer nodes than FE based on Corcos model. One might note that the response from analytical Corcos model fails to match with other simulation approaches beyond 700 Hz due to single set of decay parameters from attached zone. Random sampling has shown as a quick and good cross-check for FE simulations.

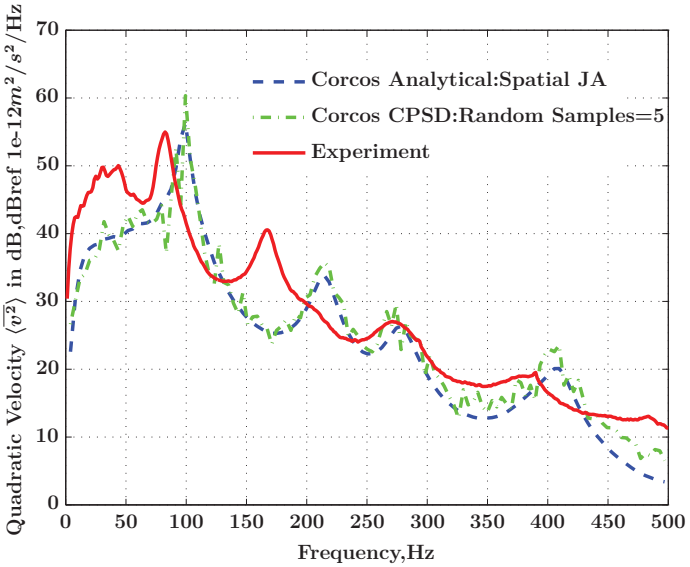

Figure 5.1 Spatial averaged quadratic velocity from Random sampling, analytical Corcos model and experiment for fence case

For a better convergence in Random sampling and finite element method, finer mesh need to be used inorder to capture the high frequency decay rates in coherence. Both the approaches give similar results but the computational time for the random sampling is drastically lesser than the finite element simulations. In this example the finite element

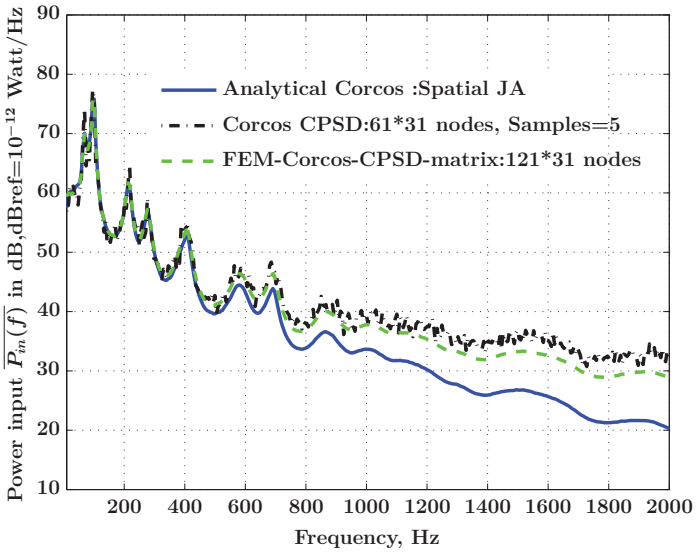

Figure 5.2 Power input from Random sampling, Analytical Corcos model and FEM for side mirror case

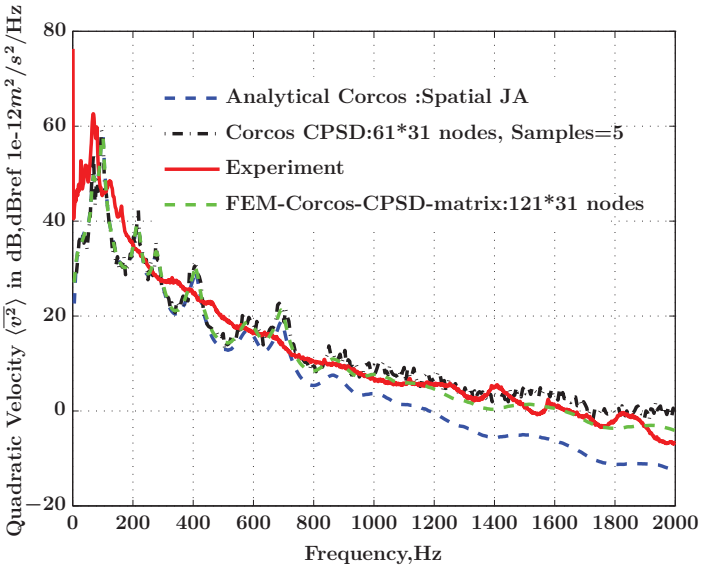

Figure 5.3 Spatial averaged quadratic velocity from Random sampling, analytical Corcos model, FEM, experiment for side mirror case

method took 3 hours on Calcul Quebec super computer with single node 250 GB memory and 48 processsors. With a smaller random sampling mesh (half the FEM nodes), the random sampling was completed in 20 minutes with 10 samples on a local desktop machine. This difference is due to the absence of joint acceptance calculation in the random sampling compared to the finite element method as the correlated excitation is decomposed into deterministic point forces.

5.4 Conclusions

Random sampling is an alternative approach considered to solve the random vibro-acoustics problem. This approach makes use of Cholesky decomposition to reduce the random excitation into simple point loads and adding random phases to it so as to construct the turbulent wall pressure. Although this approach gives good results with experiments when using a Corcos model as TBL excitation model. The major disadvantage is with the enormous number of samples required to preserve the accuracy of the random sampling simulation for a much more complicated case. The complex cross-spectral density matrix of TBL excitation using Corcos model is (complex Hermitian) symmetric but with CFD derived cross-spectral data, the assumption of symmetric and Hermitian nature of the excitation matrix does not hold good. Therefore a random sampling approach would definitely fail when the CFD derived TBL excitation is used. As an alternative, the CFD cross-spectral density matrix can be forced to a symmetric and Hermitian by matching the data set on either side of the diagonal in the matrix. But this treatment would lose non-homogeneous information captured by CFD, that is required for a accurate vibro-acoustic simulation. On the other hand CFD derived TBL excitation could be decomposed using advanced decomposition techniques which warranty further studies. In eitherway random sampling would not be suitable approach when using CFD WPF. Finally the vibro-acoustics indicators like quadratic velocity and power input using random sampling match well with FEM for Corcos model but the analytical Corcos model values differ at higher frequencies due to its empirical nature. Nevertheless it has been noticed that when using a empirical model like Corcos model, random sampling approach would reduce the computation time because of the coarse mesh compared to a full-scale FE computation.

CHAPTER 6

CONCLUSION

6.1 Summary of work

In this study, our main goal was to estimate the sound radiated inside the cavity due to the turbulent wall-pressure excitation on the side glass of the car. In this aspect, two kinds of case studies a) Flat fence (representative of A-pillar) and b) side mirror that have been the sources of automotive wind noise are considered. In both case studies, a turbulent flow with typical speed around 37-40 m/s equivalent to that of a automotive highway speed around 130 km/h excites the flat plate backed by anechoic cavity. An experimental wind tunnel setup that is able to reproduce this kind of turbulent flow was built by Purdue University. The experimental flow and acoustical results were shared as a part of collaborative research study. Three kinds of numerical approaches have been adopted to solve the aero-vibro-acoustics problem at hand. 1) Extraction of empirical model parameters from a unsteady CFD wall pressure and using a Joint acceptance analytical method to predict the vibro-acoustic response 2) Estimation of turbulent power input excitation in wavenumber and spatial domain 3) Random sampling of turbulent wall pressure excitation. To overcome the limitations of empirical models, a CFD code named PowerFLOW which is based on Lattice Boltzmann Method had been used. A systematic aerodynamic and transient CFD analysis along with validations were carried out at all levels (time, space, wavenumber and frequency) using experimental results for both flat fence and side mirror.

The decay rate for the CFD wall-pressure PSD in flat fence is proportional to $f^{\frac{-7}{3}}$ in the mid frequency range (100 Hz to 1000 Hz). The wall-pressure PSD for mirror case has a slightly lower decay rate proportional to $f^{\frac{-5}{3}}$ in the reattached region but follows similar decay rate of $f^{\frac{-7}{3}}$ like that of flat fence in separated region. It is assuring that the decay rates observed are in coincidence with values noticed by other researchers in case of separated and reattached flows. The S_{pp} (PSD) from CFD simulation of mirror case matches well with experiments, so the spatially averaged autospectrum over entire probes is used as an input to Corcos model instead of empirical spectral model. Once the aerodynamic CFD simulations are validated with experimental data from Purdue University wind tunnel, post-processing of the unsteady wall-pressure fluctuations were done using k-ω developed as a part of this work. The k-ω code is based on FFT techniques.

The k-ω code has been thoroughly validated using analytical Corcos model as an example and also verified with that available in literature [Arguillat *et al.*, 2005]. The k-ω spectrum at fixed frequency for flat fence resembles the elliptical shape [Mellen, 1990] and for side mirror resembles the rhombic shape. The acoustic zones are identified clearly in streamwise wavenumber frequency spectrum along with convective ridge. The same k-ω code has been used to study the non-stationarity and non-homogenity of the side mirror flow at different locations on the plate. It has been observed that autospectrum dictates the level of vibro-acoustic response and crosspectrum or coherence dictates the decay of the response over the frequency range. The extraction of unsteady wall pressure fluctuations using CFD code has been a big achievement in this study due to a lengthy simulation run that gives a statistically stationary set of pressure data in time and space. Although the unsteady CFD simulation ran for long time, the benefits delivered from it always outweigh the CFD run times.

It has been concluded that none of the empirical spectral model available in literature could properly predict the power spectral density of wall-pressure for flat fence and side mirror when compared with CFD wall-pressure spectra. But the closest model that could predict the roll-off at higher frequencies is given by [Rozenberg *et al.*, 2012] which includes the effect of adverse pressure gradients. A wavenumber-frequency analysis of TBL WPF reveal that, side mirror flow is more separated and reattached with vortices generated on either side of the mirror unlike the flatfence case where it is more homogeneous as the flow reaches the trailing edge. The kind of empirical model parameter identification from a long enough CFD wall-pressure is an original contribution of this study that helps to localise the flow zones into smaller homogeneous regimes where the Corcos model or any other model would be applicable. The vibro-acoustic indicators calculated from the CFD derived Corcos parameters almost match well with experiments.

The coupling of unsteady CFD wall pressure to structural mode shapes has been achieved using interpolation techniques. To efficiently *map* the unsteady CFD wall pressure onto the structural mesh an interpolation algorithm has been used without sacrificing the fine piece of information from CFD run. The coupling between CFD wall pressure and structure is properly estimated with the term known as *Joint Acceptance* in spatial and wavenumber domain. The wavenumber integration of Joint acceptance function with Corcos model has taken advantage of the coupling strength between the low Mach number flow interaction with structural modes as discussed by [Hwang *et al.*, 2003]. There are few tricks to reduce the computation time for Joint acceptance. First, to calculate in wavenumber domain with two integrals instead of four dimensional integration in spatial domain. Second, to

set up the limits of wavenumber integration based on the physical interaction rather than fully integrating till infinity or higher multiples of modal wavenumber k_{mn}. Incase of a low speed TBL flow, with typical side window glass mounting conditions, the upper limits of wavenumber integration limits could be fixed at $1.2k_{mn}$. This limit should be good enough to properly capture the total joint acceptance due to the coupling between modeshapes and cross-spectral density of TBL excitation.

Random sampling is another approach to solve the random vibro-acoustics problem using cholesky decomposition into plane waves and adding random phases to it so as to generate the turbulent wall pressure. The complex cross-spectral density matrix of TBL excitation using Corcos model is (complex Hermitian) symmetric but with CFD derived cross-spectral data, the assumption of symmetric and Hermitian nature of the excitation matrix is not true. Therefore a random sampling approach would definitely fail with CFD derived WPF excitation.

The originality of thesis is due to the estimation of Corcos parameters from a statistically converged CFD wall-pressure, by segregating homogeneous zones based on auto-spectrum and reattachment contours. Another original contribution is to minimize the computational effort in the wavenumber integration of joint acceptance by proposing upper limits based on modal wavenumber k_{mn}. Out of the three approaches used, it has been noticed that SEA based turbulent power input calculated in wavenumber domain using wall pressure from a lengthy unsteady CFD run looking promising for further development.

6.2 Future work and Perspectives

As a part of future work, there could be improvement in the computation schemes involved interpolation algorithm to map the CFD WPF onto the structural mesh. Due to the lengthy unsteady LBM simulation runs, Stochastic methods like Random Particle Method by [Ewert, 2007] and Stochastic Noise Generation and Radiation(SNGR) by [Bechara *et al.*, 1994] might be looked upon in extracting the unsteady WPF. Proper Orthogonal Decomposition (POD) and wavelets may be also be considered as promising tools for post-processing of CFD transient pressure with non-stationary and non-homogeneous nature. In the full FE computation of Joint acceptance, the concept of influential zones with respect to a reference probe could be exploited to reduce the computational time of the four dimensional spatial integration. In summary, there could be a reduction in the computation time as the Joint acceptance for the whole plate could be a summation of minor joint acceptance's per each influential zone with each reference probe on the plate.

CHAPTER 7

Résumé du travail

7.1 Résumé du travail

L'objectif principal de cette thèse est d'estimer le bruit émis à l'intérieur de la cabine dans le cas d'une excitation turbulente appelée "Turbulent Wall Pressure (TWP)" sur la vitre latérale de la voiture. Afin d'atteindre cet objectif, deux types d'études de cas ont été considérées: a) Barrière plate représentative du pilier A (A-pillar), b) Un Rétroviseur. Ces derniers representent des sources du bruit aérodynamique dans le domaine de l'automobile. Dans les deux cas, un écoulement turbulent avec une vitesse de convection typique autour de 37- 40 m/s, équivalent à une vitesse d'automobile d'environ 130 $kmph$ excite la barrière plate soutenue par une cavité anéchoïque. Un test expérimental utilisant une soufflerie capable de reproduire ce type d'écoulement turbulent a été mis en place par Purdue University. Les données expérimentales et les résultats acoustiques ont été partagés dans le cadre d'une étude en collaboration. Trois types d'approches numériques ont été adoptés pour résoudre le problème de l'aéro-vibro-acoustique. 1) Extraction des paramètres des modèles empiriques à partir d'une pression de paroi CFD transitoire et l'utilisation d'une méthode analytique de la fonction "Joint Acceptance" pour prédire la réponse vibro-acoustique 2) Estimation de la puissance injectée de l'excitation turbulente dans le domaine de nombre d'onde et le domaine spatial. 3) Échantillonnage aléatoire de l'excitation. Pour surmonter les limitations des modèles empiriques, un code CFD nommé PowerFLOW basé sur la méthode Lattice Boltzmann a été utilisé. Une analyse systématique de la CFD aérodynamique et transitoire ainsi que des validations ont été effectuées à tous les niveaux (temps, espace, nombre d'ondes et fréquence) en utilisant des résultats expérimentaux pour la barrière plate et le rétroviseur.

Le taux de décroissance de la PSD de la pression pariétale CFD dans une barrière plate est proportionnel à $f^{\frac{-7}{3}}$ dans la gamme de fréquences moyennes (100 Hz à 1000 Hz). Le PSD de la pression pariétale pour le rétroviseur a un taux de décroissance légèrement inférieur et proportionnel a $f^{\frac{-5}{3}}$ dans la région rattachée mais suit un taux de décroissance similaire au $f^{\frac{-7}{3}}$ comme celui d'une barrière plate dans une région séparée. Il a été confirmé que les taux de décroissance observés coïncident avec les valeurs constatées par d'autres chercheurs en cas de flux séparés et rattachés. Le S_{pp} (Auto-spectre) de la simulation CFD du cas rétroviseur correspond bien aux mesures expérimentales.par conséquent, l'auto-spectre

moyenné spatialement sur des sondes entières est utilisé comme entrée dans le modèle de Corcos au lieu du modèle spectral empirique. Une fois les simulations aérodynamiques CFD validées avec des données expérimentales provenant de la soufflerie de Purdue University, le post-traitement des fluctuations de la pression pariétale a été effectué à l'aide du code k-ω développé dans le présent travail et qui est basé sur les techniques FFT. Le code k-ω a été soigneusement validé en utilisant le modèle analytique de Corcos comme exemple et également vérifié avec celui disponible dans la littérature [Arguillat *et al.*, 2005]. A une fréquence fixe, le spectre k-ω ressemble à la forme elliptique dans le cas de la barrière plate [Mellen, 1990], et ressemble à la forme rhombique dans le cas du rétroviseur latéral. Les zones acoustiques et convectives sont clairement identifiées dans le spectre de nombre d'onde. Le même code k- ω a été utilisé pour étudier la non stationnarité et la non homogénéité du flux de rétroviseurs latéraux à différents endroits de la plaque.

Il a été observé que l'auto-spectre dicte le niveau de réponse vibro-acoustique et que le spectre croisé ou la cohérence dicte la décroissance de la réponse sur la gamme de fréquences. L'extraction des WPFs transitoire à l'aide du code CFD ont été une grande réussite dans cette étude grâce à une longue simulation qui fournit un ensemble de données de pression statistiquement stationnaires dans le temps et homogènes dans l'espace. Bien que la simulation CFD transitoire ait duré longtemps, ses avantages l'emportent toujours sur les durées de calcul des CFD. Il a été conclu qu'aucun des modèles spectraux empiriques disponibles dans la littérature ne permettait de prédire correctement la densité spectrale de puissance de la pression pariétale pour une barrière plate et un rétroviseur quand comparés aux spectres CFD de la pression pariétale.

Mais le modèle le plus proche capable de prédire le ralentissement à des fréquences plus élevées est donné par [Rozenberg *et al.*, 2012], qui inclut l'effet des gradients de pression "adverse pressure gradients". Une analyse fréquence-nombre d'onde de TBL WPF révèle que l'écoulement autour du rétroviseur est plus séparé et rattaché aux vortex générés de chaque côté du rétroviseur, contrairement au cas de la barrière plate où il est plus homogène lorsque le flux atteint le bord de fuite. Le type d'identification empirique des paramètres du modèle, est une contribution originale de cette étude qui aide à localiser les zones d'écoulement dans des régimes homogènes plus petits où le modèle Corcos ou tout autre modèle serait applicable. Les indicateurs vibro-acoustiques calculés à partir des paramètres Corcos dérivés de la CFD correspondent bien aux expériences.

Le couplage de la pression pariétale CFD transitoire aux formes propres de la structure a été obtenu en utilisant des techniques d'interpolation. Pour pouvoir cartographier efficacement la pression pariétale CFD transitoire sur le maillage structurel, un algorithme

d'interpolation a été utilisé sans sacrifier la fine information issue de l'analyse CFD. Le couplage entre la pression pariétale CFD et la structure est correctement estimé avec le terme connu sous le nom de *Joint Acceptance* dans le domaine spatial et le domaine du nombre d'onde. L'intégration en nombre d'onde de la fonction "Joint Acceptance" avec le modèle Corcos a tiré partie du couplage fort entre l'interaction de l'écoulement à faible vitesse et les modes structuraux, comme l'explique [Hwang *et al.*, 2003]. Il y'a peu d'astuces pour réduire le temps de calcul pour la "Joint Acceptance". Premièrement, un calcul dans le domaine des nombres d'ondes avec deux intégrales au lieu d'une intégration à quatre dimensions dans le domaine spatial. Deuxièmement, définir les limites de l'intégration du nombre d'ondes sur la base de l'interaction physique plutôt que d'intégrer pleinement les infinis ou les ordres supérieurs du nombre d'ondes modal k_{mn}. En présence d'un flux TBL à faible vitesse, avec des conditions de montage typiques des vitres latérales, les limites supérieures d'intégration des nombres d'ondes pourraient être fixées à $1.2k_{mn}$. Cette limite devrait être suffisante pour bien saisir l'acceptation totale de l'articulation en raison du couplage entre les modes et la densité spectrale croisée de l'excitation TBL.

L'échantillonnage aléatoire est une autre approche pour résoudre le problème de la vibro-acoustique aléatoire en utilisant la décomposition de Cholesky en ondes planes et en y'ajoutant des phases aléatoires afin de générer la pression pariétale turbulente. La matrice de la densité cross-spectrale complexe de l'excitation de TBL utilisant le modèle de Corcos est (complexe hermitien) symétrique mais avec des données transversales dérivées de CFD, l'hypothèse de la nature symétrique et hermitienne de la matrice d'excitation n'est pas vraie. Par conséquent, une approche basée sur l'échantillonnage aléatoire ne fonctionne pas avec une excitation WPF dérivée CFD. Parmi les trois approches utilisées, on a remarqué que la puissance turbulente basée sur la SEA calculée dans le domaine du nombre d'ondes en utilisant la pression pariétale d'un long calcul CFD transitoire semblait prometteuse pour un développement ultérieur. Intégrer une intégration intelligente du nombre d'ondes de "Joint Acceptance" réduirait certainement le temps de calcul par rapport à l'intégration du nombre d'onde avec des limites supérieures basées sur le nombre d'ondes convectif.

7.2 Travaux futurs et Perspectives

Dans le cadre de travaux futurs, il pourrait y avoir une amélioration dans les schémas de calcul utilisant les algorithmes d'interpolation pour mapper le CFD WPF sur le maillage structurel. En raison de la longueur des simulations LBM transitoire, les méthodes stochastiques telles que la méthode des particules aléatoires par [Ewert, 2007] et la génération et le rayonnement stochastiques du bruit (SNGR) par [Bechara *et al.*, 1994] pourraient être utilisées pour extraire le WPF transitoire. La décomposition orthogonale propre (POD) et

les ondelettes peuvent également être considérées comme des outils prometteurs pour le post-traitement de la pression transitoire des CFD avec un caractère non stationnaire et non homogène. Dans le calcul FE complet de la “Joint Acceptance”, le concept de zones d’influence par rapport à une sonde de référence pourrait être exploité pour réduire le temps de calcul de l’intégration spatiale à quatre dimensions. En résumé, il pourrait y avoir une réduction du temps de calcul, car la “Joint Acceptance” pour la plaque entière pourrait être une somme d’un ensemble de “Joint Acceptance” mineures pour chaque zone influente avec chaque sonde de référence sur la plaque.

LIST OF REFERENCES

Abraham, B. M. and Keith, W. L. (1998). Direct measurements of turbulent boundary layer wall pressure wavenumber-frequency spectra. *Journal of Fluids Engineering*, volume 120, number 1, pp. 29–39. 33, 42

Albarracin, C., Doolan, C., Jones, R., Hansen, C., Brooks, L. and Teubner, M. (2012). A RANS-based statistical noise model for trailing edge noise. In *18th AIAA/CEAS Aeroacoustics Conference (33rd AIAA Aeroacoustics Conference)*. AIAA, p. 2181. 39

Allen, M. and Vlahopoulos, N. (2001). Noise generated from a flexible and elastically supported structure subject to turbulent boundary layer flow excitation. *Finite Elements in Analysis and Design*, volume 37, number 9, pp. 687–712. 45

Arguillat, B., Ricot, D., Bailly, C. and Robert, G. (2010). Measured wavenumber: Frequency spectrum associated with acoustic and aerodynamic wall pressure fluctuations. *Journal of the Acoustical Society of America*, volume 128, number 4, pp. 1647–1655. 42, 74, 82, 84, 92

Arguillat, B., Ricot, D., Robert, G. and Bailly, C. (2005). Measurements of the wavenumber-frequency spectrum of wall pressure fluctuations under turbulent flows. In *Collection of Technical Papers - 11th AIAA/CEAS Aeroacoustics Conference*, volume 1. AIAA, pp. 722–739. 42, 50, 51, 74, 75, 131, 134

Ask, J. and Davidson, L. (2009). A numerical investigation of the flow past a generic side mirror and its impact on sound generation. *Journal of Fluids Engineering, Transactions of the ASME*, volume 131, number 6, pp. 0621011–06110212. 56

Atalla, N. and Sgard, F. (2015). *Finite element and boundary methods in structural acoustics and vibration*. CRC Press. 95, 107, 114, 125

Bechara, W., Bailly, C., Lafon, P. and Candel, S. M. (1994). Stochastic approach to noise modeling for free turbulent flows. *AIAA journal*, volume 32, number 3, pp. 455–463. 39, 132, 135

Bendat, J. S. and Piersol, A. G. (2011). *Random data: analysis and measurement procedures*, volume 729. John Wiley & Sons. 74

Blake, W. K. (1970). Turbulent boundary-layer wall-pressure fluctuations on smooth and rough walls. *Journal of Fluid Mechanics*, volume 44, number 4, pp. 637–660. 47

Blake, W. K. (2017). *Mechanics of flow-induced sound and vibration, Volume 2: Complex flow-structure interactions*. Academic press. 41, 45

Blanchet, D., Alimonti, L. and Golota, A. (2016). Applying complex turbulent cross-correlation function to an SEA side glass to predict interior wind noise. *SAE Technical Paper*. 103

Borisyuk, A. O. and Grinchenko, V. T. (1997). Vibration and noise generation by elastic elements excited by a turbulent flow. *Journal of Sound and Vibration*, volume 204, number 2, pp. 213–237. 32

Bradshaw, P. (1967). The turbulence structure of equilibrium boundary layers. *Journal of Fluid Mechanics*, volume 29, number 4, pp. 625–645. 38

Bremner, P. and Wilby, J. (2002). Aero-vibro-acoustics: Problem statement and methods for simulation-based design solution. In *8th AIAA/CEAS Aeroacoustics Conference and Exhibit*. 4, 48, 103

Bull, M. K. (1996). Wall-pressure fluctuations beneath turbulent boundary layers: Some reflections on forty years of research. *Journal of Sound and Vibration*, volume 190, number 3, pp. 299–315. ix, 3, 25

Caiazzo, A., Desmet, W. *et al.* (2016). A generalized corcos model for modelling turbulent boundary layer wall pressure fluctuations. *Journal of Sound and Vibration*, volume 372, pp. 192–210. 29

Caillet, A. (2008). *Validation numérique du comportement d'une plaque excitée par un écoulement turbulent modelisé par powerflow couplé à un logiciel de vibroacoustique*. Master's thesis, Université de Sherbrooke. 6, 101

Careta, A., Sagués, F. and Sancho, J. (1993). Stochastic generation of homogeneous isotropic turbulence with well-defined spectra. *Physical Review E*, volume 48, number 3, pp. 2279–2287. 40

Caro, S., Ramonda, A., Pérot, F., Vergne, S. and Pechabat, M. (2006). TBL noise generated by a simplified side mirror configuration and acoustic transfer through the window: Modelling using ACTRAN and FLUENT. In *Collection of Technical Papers - 12th AIAA/CEAS Aeroacoustics Conference*, volume 2. pp. 1146–1168. 27, 46

Castro, I. and Haque, A. (1987). The structure of a turbulent shear layer bounding a separation region. *Journal of Fluid Mechanics*, volume 179, pp. 439–468. 12

Catlett, M. R., Anderson, J. M., Forest, J. B. and Stewart, D. O. (2015). Empirical modeling of pressure spectra in adverse pressure gradient turbulent boundary layers. *AIAA Journal*, volume 54, number 2, pp. 569–587. 27, 28, 72

Çengel, Y. A. and Cimbala, J. M. (2006). *Fluid mechanics: fundamentals and applications*. McGraw-Hill Higher Education, Boston, 956 pp. 14

Chandiramani, K. (1977). Vibration response of fluid-loaded structures to low-speed flow noise. *The Journal of the Acoustical Society of America*, volume 61, pp. 1460–1470. 115

Chang III, P. A., Piomelli, U. and Blake, W. K. (1999). Relationship between wall pressure and velocity-field sources. *Physics of Fluids*, volume 11, number 11, pp. 3434–3448. 34

Chase, D. M. (1980). Modeling the wavevector-frequency spectrum of turbulent boundary layer wall pressure. *Journal of Sound and Vibration*, volume 70, number 1, pp. 29–67. 27, 30

Chase, D. M. (1987). The character of the turbulent wall pressure spectrum at subconvective wavenumbers and a suggested comprehensive model. *Journal of Sound and Vibration*, volume 112, number 1, pp. 125–147. 27, 29, 31, 32

Chase, D. M. (1993). A semi-empirical model for the wavevector-frequency spectrum of turbulent wall-shear stress. *Journal of Fluids and Structures*, volume 7, number 6, pp. 639–659. 32

Chen, H. (1998). Volumetric formulation of the Lattice Boltzmann method for fluid dynamics: Basic concept. *Physical Review E*, volume 58, number 3, pp. 3955–3963. 51

Choi, H. and Moin, P. (1990). On the space-time characteristics of wall-pressure fluctuations. *Physics of Fluids A*, volume 2, number 8, pp. 1450–1460. 34

Cockburn, J. A. and Robertson, J. E. (1974). Vibration response of spacecraft shrouds toin-flight fluctuating pressures. *Journal of Sound and Vibration*, volume 33, number 4, pp. 399–425. 26, 29, 30

Coles, D. (1956). The law of the wake in the turbulent boundary layer. *Journal of Fluid Mechanics*, volume 1, number 02, pp. 191–226. 18, 66

Coney, W., Her, J. and Moore, J. (1999). A semi-empirical approach for modeling greenhouse surface wind noise. *SAE Technical Papers, 1999-01-1811*. 84

Corcos, G. (1963). Resolution of pressure in turbulence. *The Journal of the Acoustical Society of America*, volume 35, pp. 192–199. 29

Coyette, J.-P., Detandt, Y., Lielens, G. and Van den Nieuwenhof, B. (2009). *Vibro-acoustic simulation of mechanical components excited by distributed random loads* (Technical report). SAE Technical Papers, 2009-01-2212. 48, 125

Crocker, M. J. (2007). *Handbook of noise and vibration control*. John Wiley & Sons, Hoboken, N.J., 1569 pp. ix, 1, 2, 11

Crouse, B., Freed, D., Balasubramanian, G., Senthooran, S., Lew, P.-T. and Mongeau, L. (2006a). Fundamental aeroacoustic capabilities of the Lattice-Boltzmann Method. In *Collection of Technical Papers - 12th AIAA/CEAS Aeroacoustics Conference*, volume 4. pp. 2120–2136. 35

Crouse, B., Senthooran, S., Freed, D., Balasubramanian, G., Gleason, M., Puskarz, M., Lew, P. and Mongeau, L. (2006b). Experimental and numerical investigation of a flow-induced cavity resonance with application to automobile buffeting. In *Collection of Technical Papers - 12th AIAA/CEAS Aeroacoustics Conference*, volume 2. pp. 1198–1215. 4

Davies, H. G. (1971). Sound from turbulent-boundary-layer-excited panels. *The Journal of the Acoustical Society of America*, volume 49, pp. 878–889. 44, 47

Dejong, R., Bharj, T. and Lee, J. (2001). Vehicle wind noise analysis using a SEA model with measured source levels. *SAE Technical Papers*. 48, 84

Dowling, A. (1984). Mean flow effects of the low-wavenumber pressure spectrum on a flexible surface. In *Symposium on Flow-Induced Vibrations: Turbulence-induced noise and vibration of rigid and compliant surfaces*, volume 5. American Society of Mechanical Engineers, p. 63. 10

Driver, D. M. and Johnston, J. P. (1990). Experimental study of a three-dimensional shear-driven turbulent boundary layer with streamwise adverse pressure gradient. *NASA Ames Research Center Technical Report*, pp. 1–266. 12

Driver, D. M., Seegmiller, H. L. and Marvin, J. G. (1987). Time-dependent behavior of a reattaching shear layer. *AIAA journal*, volume 25, number 7, pp. 914–919. ix, 13

Druault, P., Hekmati, A. and Ricot, D. (2013). Discrimination of acoustic and turbulent components from aeroacoustic wall pressure field. *Journal of Sound and Vibration*, volume 332, number 26, pp. 7257–7278. 75

Efimtsov, B. (1982). Characteristics of the field of turbulent wall pressure fluctuations at large Reynolds numbers. *Soviet Physics Acoustics*, volume 28, number 4, pp. 289–292. 26, 29, 31

Efimtsov, B. (1984). Similarity criteria for the spectra of wall pressure fluctuations in a turbulent boundary layer. *Soviet Physics Acoustics*, volume 30, pp. 33–35. 26

Ewert, R. (2007). RPM - the fast random particle-mesh method to realize unsteady turbulent sound sources and velocity fields for CAA applications. In *13th AIAA/CEAS Aeroacoustics Conference (28th AIAA Aeroacoustics Conference)*. p. 3506. 39, 132, 135

Ewert, R., Dierke, J., Siebert, J., Neifeld, A., Appel, C., Siefert, M. and Kornow, O. (2011). CAA broadband noise prediction for aeroacoustic design. *Journal of Sound and Vibration*, volume 330, number 17, pp. 4139–4160. 39, 40

Fahy, F. J. and Gardonio, P. (2007). *Sound and structural vibration: radiation, transmission and response*. Elsevier. 114

Farabee, T. M. (1986). *An experimental investigation of wall pressure fluctuations beneath non-equilibrium turbulent flows* (Technical report). DTIC Document. ix, 28

Finnveden, S., Birgersson, F., Ross, U. and Kremer, T. (2005). A model of wall pressure correlation for prediction of turbulence-induced vibration. *Journal of Fluids and Structures*, volume 20, number 8, pp. 1127–1143. 29, 46

Francois, V. H., Bordji, M., Baresch, D. and Lafon, P. (2011). Wavenumber-frequency analysis of the wall pressure fluctuations in the wake of a car side mirror. In *17th AIAA/CEAS Aeroacoustics Conference (32nd Aeroacoustics Conference)*. p. 2936. 50, 74

Gad-el Hak, M. (2001). Flow control: The future. *Journal of Aircraft*, volume 38, number 3, pp. 402–418. 23

Glegg, S., Morin, B., Atassi, O. and Reba, R. (2010). Using Reynolds-averaged Navier-Stokes calculations to predict trailing-edge noise. *AIAA Journal*, volume 48, number 7, pp. 1290–1301. 38

Gloerfelt, X. and Berland, J. (2013). Turbulent boundary-layer noise: Direct radiation at Mach number 0.5. *Journal of Fluid Mechanics*, volume 723, pp. 318–351. 35, 74

Goody, M. (2004). Empirical spectral model of surface pressure fluctuations. *AIAA Journal*, volume 42, number 9, pp. 1788–1794. 26, 27, 33, 72

Graham, W. R. (1997). A comparison of models for the wavenumber-frequency spectrum of turbulent boundary layer pressures. *Journal of Sound and Vibration*, volume 206, number 4, pp. 541–565. 32

Gravante, S. P., Naguib, A. M., Wark, C. E. and Nagib, H. M. (1998). Characterization of the pressure fluctuations under a fully developed turbulent boundary layer. *AIAA Journal*, volume 36, number 10, pp. 1808–1816. 34

Hambric, S. A., Hwang, Y. F. and Bonness, W. K. (2004). Vibrations of plates with clamped and free edges excited by low-speed turbulent boundary layer flow. *Journal of Fluids and Structures*, volume 19, number 1, pp. 93–110. 29, 103, 114

Han, F., Bernhard, R. J. and Mongeau, L. G. (1999). Prediction of flow-induced structural vibration and sound radiation using energy flow analysis. *Journal of Sound and Vibration*, volume 227, number 4, pp. 685–709. 45

He, X. and Luo, L.-S. (1997). Theory of the Lattice boltzmann Method: From the Boltzmann equation to the lattice Boltzmann equation. *Physical Review E*, volume 56, number 6, pp. 6811–6817. 51

Hekmati, A., Ricot, D. and Druault, P. (2010). Vibroacoustic behavior of a plate excited by synthesized aeroacoustic pressure fields. In *16th AIAA/CEAS Aeroacoustics Conference*. p. 3950. 48

Hekmati, A., Ricot, D. and Druault, P. (2013). Numerical synthesis of aeroacoustic wall pressure fields over a flat plate: Generation, transmission and radiationanalyses. *Journal of Sound and Vibration*, volume 332, number 13, pp. 3163–3176. 48

Hinze, J. O. (1975). *Turbulence*, 2nd edition. McGraw-Hill, New York, 790 pp. 10, 11

Horton, H. P. (1968). *Laminar separation bubbles in two and three dimensional incompressible flow*. Ph.D. thesis, University of London. ix, 13

Howe, M. S. (1987). On the structure of the turbulent boundary-layer wall pressure spectrum in the vicinity of the ACoustic wavenumber. *Proceedings of the Royal Society of London, Series A: Mathematical and Physical Sciences*, volume 412, number 1843, pp. 389–401. 31

Howe, M. S. (1998). *Acoustics of fluid-structure interactions*. Cambridge University Press, Cambridge ; New York, 560 pp. ix, 25, 27

Hu, N. and Herr, M. (2016). Characteristics of wall pressure fluctuations for a flat plate turbulent boundary layer with pressure gradients. In *22nd AIAA/CEAS Aeroacoustics Conference*. p. 2749. 27, 72

Hucho, W.-H. (1998). *Aerodynamics of road vehicles: from fluid mechanics to vehicle engineering*, 4th edition. Society of Automotive Engineers, Warrendale, PA, 918 pp. 1

Hwang, Y. F., Bonness, W. K. and Hambric, S. A. (2003). *On Modeling Structural Excitations by Low Speed Turbulent Boundary Layer Flows* (Technical Report ADA465806). DTIC Document, 60 pages pp. ix, 3, 27, 28, 29, 32, 33, 131, 135

Hwang, Y. F., Bonness, W. K. and Hambric, S. A. (2009). Comparison of semi-empirical models for turbulent boundary layer wall pressure spectra. *Journal of Sound and Vibration*, volume 319, number 1-2, pp. 199–217. 26, 72

Höld, R., Brenneis, A., Eberle, A., Schwarz, V. and Siegert, R. (1999). Numerical simulation of aeroacoustic sound generated by generic bodies placed on a plate: Part i - prediction of aeroacoustic sources. In *5th AIAA/CEAS Aeroacoustics Conference and Exhibit*. p. 1896. 50

Joslin, R. D., Thomas, R. H. and Choudhari, M. M. (2005). Synergism of flow and noise control technologies. *Progress in Aerospace Sciences*, volume 41, number 5, pp. 363–417. 23

Juvé, D., Berton, M. and Salze, E. (2015). Spectral properties of wall-pressure fluctuations and their estimation from computational fluid dynamics. In *Flinovia-Flow Induced Noise and Vibration Issues and Aspects*. Springer, pp. 27–46. 28, 39

Kamruzzaman, M., Bekiropoulos, D., Lutz, T., Würz, W. and Krämer, E. (2015). A semi-empirical surface pressure spectrum model for airfoil trailing-edge noise prediction. *International Journal of Aeroacoustics*, volume 14, number 5-6, pp. 833–882. 27

Keith, W. L. and Abraham, B. M. (1994). *Derivation of a Wavenumber Filter Design for the Measurement of Turbulent Wall Pressure Fluctuations* (Technical report). Naval Undersea Warfare Center Division Newport Div RI. ix, 44

Keith, W. L., Hurdis, D. A. and Abraham, B. M. (1992). Comparison of turbulent boundary layer wall-pressure spectra. *Journal of Fluids Engineering, Transactions of the ASME*, volume 114, number 3, pp. 338–347. 26, 42

Khalighi, Y. (2010). *Computational aeroacoustics of complex flows at low Mach number*. Ph.D. thesis, Stanford University. 56

Khalighi, Y., Mani, A., Ham, F. and Moin, P. (2010). Prediction of sound generated by complex flows at low mach numbers. *AIAA Journal*, volume 48, number 2, pp. 306–316. 56

Klein, M., Sadiki, A. and Janicka, J. (2003). A digital filter based generation of inflow data for spatially developing direct numerical or Large Eddy Simulations. *Journal of Computational Physics*, volume 186, number 2, pp. 652–665. 40

Kraichnan, R. (1956). Pressure fluctuations in turbulent flow over a flat plate. *Journal of the Acoustical Society of America*, volume 28, number 3, pp. 378–390. 36, 38

Kraichnan, R. H. (1970). Diffusion by a random velocity field. *Physics of Fluids (1958-1988)*, volume 13, number 1, pp. 22–31. 39

Lee, Y. T., Blake, W. K. and Farabee, T. M. (2005). Modeling of wall pressure fluctuations based on time mean flow field. *Journal of Fluids Engineering, Transactions of the ASME*, volume 127, number 2, pp. 233–240. 38

Lee, Y. T., Farabee, T. M. and Blake, W. K. (2009). Turbulence effects of wall-pressure fluctuations for reattached flow. *Computers and Fluids*, volume 38, number 5, pp. 1033–1041. 38

Leishman, G. J. (2006). *Principles of helicopter aerodynamics with CD extra*. Cambridge university press, 816 pp. ix, 16

Liepmann, H. W. (1943). Investigations on laminar boundary-layer stability and transition on curved boundaries. *NACA Wartime Report ACRno: 3H30*, pp. 1–68. 15

Lueptow, R. M. (1995). Transducer resolution and the turbulent wall pressure spectrum. *Journal of the Acoustical Society of America*, volume 97, number 1, pp. 370–378. 42

Lyon, R. H. (2014). *Theory and Application of Statistical Energy Analysis*. Elsevier. 95

Maidanik, G. and Jorgensen, D. (1967). Boundary wave-vector filters for the study of the pressure field in a turbulent boundary layer. *The Journal of the Acoustical Society of America*, volume 42, pp. 494–501. 43

Manoha, E. (1996). The wavenumber-frequency spectrum of the wall pressure fluctuations beneath a turbulent boundary layer. In *2nd AIAA/CEAS Aeroacoustics Conference*. pp. 1758–1772. 42

Mastrello, L. (1969). Radiation from panel response to a supersonci turbulent boundary layer. *Journal of Sound and Vibration*, volume 10, number 2, pp. 261–295. 26

Maury, C., Gardonio, P. and Elliott, S. J. (2002). A wavenumber approach to modelling the response of a randomly excited panel, part ii: Application to aircraft panels excited by a turbulent boundary layer. *Journal of Sound and Vibration*, volume 252, number 1, pp. 115–139. ix, 44, 45

Mazzoni, D. (2003). An efficient approximation for the vibro-acoustic response of a turbulent boundary layer excited panel. *Journal of Sound and Vibration*, volume 264, number 4, pp. 951–971. 44, 46

Mellen, R. H. (1990). On modeling convective turbulence. *The Journal of the Acoustical Society of America*, volume 88, p. 2891. 29, 80, 131, 134

Millan, P. and Riethmuller, M. L. (2003). *Post-processing of experimental and numerical data: February 17-21, 2003*, volume 2003-03. Von Karman Institute for Fluid Dynamics, Rhode Saint Genèse, Belgium. 75

Miller, T. S., Gallman, J. M. and Moeller, M. J. (2012). Review of turbulent boundary-layer models for acoustic analysis. *Journal of Aircraft*, volume 49, number 6, pp. 1739–1754. 32

Norton, M. P. and Karczub, D. G. (2003). *Fundamentals of noise and vibration analysis for engineers*. Cambridge university press. 95

Panton, R. L. and Linebarger, J. H. (1974). Wall pressure spectra calculations for equilibrium boundary layers. *Journal of Fluid Mechanics*, volume 65, number Part 2, pp. 261–287. 37, 38

Park, J., Mongeau, L. and Siegmund, T. (2004). An investigation of the flow-induced sound and vibration of viscoelastically supported rectangular plates: Experiments and model verification. *Journal of Sound and Vibration*, volume 275, number 1-2, pp. 249–265. 5, 6, 44, 51, 56, 82, 84, 92, 98, 127

Peltier, L. J. and Hambric, S. A. (2007). Estimating turbulent-boundary-layer wall-pressure spectra from cfd rans solutions. *Journal of Fluids and Structures*, volume 23, number 6, pp. 920–937. 38

Pérot, F., Auger, J.-M., Giardi, H., Bailly, C. and Juvé, D. (2004). Computation of the noise generated by low mach number flows around a cylinder and a wall-mounted half cylinder. In *10th AIAA/CEAS Aeroacoustics Conference*. p. 2859. 56

Pérot, F., Meskine, M. and Vergne, S. (2009). Investigation of statistical properties of pressure loadings on real automotive side glasses. In *15th AIAA/CEAS Aeroacoustics Conference (30th AIAA Aeroacoustics Conference)*. p. 3402. 50, 84

Petyt, M. (1990). *Introduction to finite element vibration analysis*. Cambridge University Press, Cambridge England ; New York, 558 pp. 95

Pope, L. (1979). Update on the low wave number content of TBL pressure fields. *Shock Vibration Information Center Shock Vibration Digest*, volume 11, pp. 15–22. 41

Powell, R. E., Senthooran, S. and Freed, D. M. (2010). Statistical analysis of correlation between simulation and measurement of interior wind noise. In *ASME 2010 3rd Joint US-European Fluids Engineering Summer Meeting collocated with 8th International Conference on Nanochannels, Microchannels, and Minichannels*, American Society of Mechanical Engineers. pp. 2727–2737. 4

Ragnarsson, P., Schram, C., Tournour, M., Freed, D., Senthooran, S. and Pan, F. (2007). Using statistical methods to predict turbulence induced sound and vibration in aerospace and automotive applications. In *14th International Congress on Sound and Vibration 2007, ICSV 2007*, volume 3. pp. 2298–2305. 47

Remmler, S., Christophe, J., Anthoine, J. and Moreau, S. (2010). Computation of wall-pressure spectra from steady flow data for noise prediction. *AIAA Journal*, volume 48, number 9, pp. 1997–2007. 38

Robert, G. (1984). *Modélisation et simulation du champ excitateur induit sur une structure par une couche limite turbulente*. Ph.D. thesis, Ecole Centrale de Lyon. 44, 47, 106

Rosa, S. D. and Franco, F. (2008). Exact and numerical responses of a plate under a turbulent boundary layer excitation. *Journal of Fluids and Structures*, volume 24, number 2, pp. 212–230. 103

Rozenberg, Y., Robert, G. and Moreau, S. (2012). Wall-pressure spectral model including the adverse pressure gradient effects. *AIAA Journal*, volume 50, number 10, pp. 2168–2179. 27, 33, 38, 72, 73, 131, 134

Rozenberg, Y. and Roger, M.and Moreau, S. (2010). Rotating blade trailing-edge noise: Experimental validation of analytical model. *AIAA Journal*, volume 48, number 5, pp. 951–962. 38

Salze, E., Bailly, C., Marsden, O., Jondeau, E. and Juvé, D. (2014). An experimental characterisation of wall pressure wavevector-frequency spectra in the presence of pressure gradients. In *20th AIAA/CEAS Aeroacoustics Conference*. Number 2014-2909. 74

Salze, E., Bailly, C., Marsden, O., Jondeau, E. and Juvé, D. (2015). An experimental investigation of wall pressure fluctuations beneath pressure gradients. In *21st AIAA/CEAS Aeroacoustics Conference*. Number 2015-3148. 43, 74

Schewe, G. (1983). On the structure and resolution of wall-pressure fluctuations associated with turbulent boundary-layer flow. *Journal of Fluid Mechanics*, volume 134, pp. 311–328. 42

Schlichting, H. and Gersten, K. (2000). *Boundary-layer theory*. Springer Science & Business Media. 16, 20

Schloemer, H. H. (1967). Effects of pressure gradients on turbulent-boundary-layer wall-pressure fluctuations. *The Journal of the Acoustical Society of America*, volume 42, number 1, pp. 93–113. 28

Senthooran, S., Crouse, B., Balasubramanian, G., Freed, D., Noelting, S. and Gleason, M. (2005). Simulation of wall pressure fluctuations on simplified automobile shapes using a Lattice based method. In *ASME 2005 International Mechanical Engineering Congress and Exposition*, American Society of Mechanical Engineers. pp. 115–123. 4

Senthooran, S., Crouse, B., Noelting, S., Freed, D., Duncan, B., Balasubramanian, G. and Powell, R. (2006). Prediction of wall pressure fluctuations on an automobile side-glass using a Lattice-Boltzmann method. In *Collection of Technical Papers - 12th AIAA/CEAS Aeroacoustics Conference*, volume 3. pp. 1945–1959. 36, 50

Siefert, M., Ewert, R., Unruh, O. and Heintze, O. (2010). A synthetic wall pressure model for the efficient simulation of boundary layer induced cabin noise. In *16th AIAA/CEAS Aeroacoustics Conference, Stockholm, Sweden*. 40

Simpson, R. L. (1996). Aspects of turbulent boundary-layer separation. *Progress in Aerospace Sciences*, volume 32, number 5, pp. 457–521. 12

Smol'yakov, A. and Tkachenko, V. (1991). Model of a field of pseudosonic turbulent wall pressures and experimental data. *Soviet physics.Acoustics*, volume 37, number 6, pp. 627–631. 26, 29, 32, 45, 46, 72

Smol'yakov, A. V. (2000). Calculation of the spectra of pseudosound wall-pressure fluctuations in turbulent boundary layers. *Acoustical Physics*, volume 46, number 3, pp. 342–347. 27, 32

Strawderman, W. A. and Brand, R. S. (1969). Turbulent-flow-excited vibration of a simply supported, rectangular flat plate. *The Journal of the Acoustical Society of America*, volume 45, pp. 177–192. 43

Strumolo, G. S. (2002). VAWT: The virtual aerodynamic/aeroacoustic wind tunnel. *Journal of Engineering Mathematics*, volume 43, number 2-4, pp. 173–187. 48

Tengzelius, U. (2010). A semi-random finite element modal approach to turbulent boundary layer induced sound transmission. In *16th AIAA/CEAS Aeroacoustics Conference*. p. 3952. 48

Totaro, N. and Guyader, J. L. (2003). Model of frequency averaged injected power into a plate excited by a turbulent boundary layer. *Acta Acustica (Stuttgart)*, volume 89, number 4, pp. 647–657. 47

Vadavalli, V., Moreau, S. and Atalla, N. (2011). Statistical properties of pressure loadings and vibroacoustic response of a simplified side glass induced by the flow over generic flow-deflector and side-mirror. In *17th AIAA/CEAS Aeroacoustics Conference (32nd AIAA Aeroacoustics Conference)*. p. 2848. 50

Védy, E., Van Lier, L., Parchen, R., Golliard, J., Van Beek, P., Tibaut, P. and Baier, W. (2005). *Application of statistical noise generation and radiation for aeroacoustic predictions in the automotive industry* (Technical report). SAE Technical Paper. 40

Wang, M., Moreau, S., Iaccarino, G. and Roger, M. (2009). LES prediction of wall-pressure fluctuations and noise of a low-speed airfoil. *International Journal of Aeroacoustics*, volume 8, number 3, pp. 177–197. 35

White, F. M. (1999). *Fluid mechanics*, 4th edition. WCB/McGraw-Hill, Boston, Mass., 826 pp. ix, 17, 23, 56

White, F. M. (2006). *Viscous fluid flow*, 3rd edition. McGraw-Hill Higher Education, New York, NY, 629 pp. 14

Williams, J. E. F. (1982). Boundary-layer pressures and the corcos model: a development to incorporate low-wavenumber constraints. *Journal of Fluid Mechanics*, volume 125, pp. 9–25. 29, 31

Wills, J. (1971). Measurements of the wave-number/phase velocity spectrum of wall pressure beneath a turbulent boundary layer. *Journal of Fluid Mechanics*, volume 45, number 01, pp. 65–90. 41

Winkler, J., Carolus, T. and Moreau, S. (2009). Airfoil trailing-edge blowing: Broadband noise prediction from large-eddy simulation. In *15th AIAA/CEAS Aeroacoustics Conference (30th AIAA Aeroacoustics Conference)*. AIAA, p. 3200. 35

Wittig, L. E. and Sinha, A. K. (1975). Simulation of multicorrelated random processes using the FFT algorithm. *Journal of the Acoustical Society of America*, volume 58, number 3, pp. 630–634. 48, 125

Witting, J. (1986). A spectral model of pressure fluctuations at a rigid wall bounding an incompressible fluid, based on turbulent structures in the boundary layer. *Noise Control Eng.J*, volume 26, number 1, pp. 28–43. 27, 29, 31